A First Principles Computational Study of $ZnO/PbTiO_3$ as a Tunable Catalyst for CO_2 Conversion

by

Babatunde Alawode
B.Sc., University of Lagos, Nigeria (2010)

Submitted to the Department of Mechanical Engineering and DMSE
in partial fulfillment of the requirements for the degrees of
Master of Science in Mechanical Engineering
and
Master of Science in Material Science and Engineering
at the
MASSACHUSETTS INSTITUTE OF TECHNOLOGY
June 2015

Author .....
Department of Mechanical Engineering and DMSE
April 27, 2015

Certified by .....
Alexie M. Kolpak
Assistant Professor, Department of Mechanical Engineering
Thesis Supervisor

Certified by .....
Jeffrey C. Grossman
Associate Professor, DMSE
Thesis Supervisor

Accepted by .....
David E. Hardt
Chairman, Department of Mechanical Engineering Committee on Graduate Students

Accepted by .....
Donald R. Sadoway
Chairman, DMSE Committee on Graduate Students

A First Principles Computational Study of $ZnO/PbTiO_3$ as a Tunable Catalyst for CO_2 Conversion

by

Babatunde Alawode

Submitted to the Department of Mechanical Engineering and DMSE
on April 27, 2015, in partial fulfillment of the
requirements for the degrees of
Master of Science in Mechanical Engineering
and
Master of Science in Material Science and Engineering

Abstract

Due to its role in climate change, there is great interest in finding ways to take advantage of the vast amount of waste CO_2 we produce by its conversion to useful substances. This approach is currently impractical due to the high temperatures and pressures generally required for the synthesis of compounds using CO_2 as a precursor. To make direct CO_2 capture and conversion economically viable, new materials able to catalyze the conversion reactions at significantly milder conditions will be essential. In this thesis, we use DFT computations to begin the design of a dynamically tunable ferroelectric oxide-supported thin film catalyst that can capture CO_2 directly from the emission stream and convert it into methanol or cyclic carbonates. Promising candidates for a dynamically tunable catalyst of this type are the different combinations of ZnO directions grown on the perovskite $PbTiO_3$.

For the non-polar $ZnO(11\bar{2}0)$ grown on the perovskite, we demonstrate that the surface chemistry is dependent on both the polarization direction of the $PbTiO_3$ substrate and on the number of $ZnO(11\bar{2}0)$ layers n. Growing the ZnO in the (0001) direction on the perovskite showed even more interesting results. We found that this process is sufficient to obtain a ZnO ferroelectric and is superior to previous attempts to make ferroelectric phase changes possible in the oxide, namely Li-doping. We demonstrate that switiching the polarization direction of the perovskite substrate is sufficient to switch the polarity at the ZnO surface. This is an excellent basis for a dynamically tunable catalyst.

Thesis Supervisor: Alexie M. Kolpak
Title: Assistant Professor, Department of Mechanical Engineering

Thesis Supervisor: Jeffrey C. Grossman
Title: Associate Professor, DMSE

Acknowledgments

This thesis would not be possible without the help and guidance of several people. From my first day in the United States on August 26th 2012, Professor Alexie Kolpak has helped me navigate the intricacies of the MIT environment and to [somewhat] understand the physics of materials. Coming from a non-material science background, her open-door policy and friendly demeanor helped me get up to speed on research much faster.

Special thanks also goes to my colleagues in the Kolpak Group. The special effort of Dr. Brian Kolb in getting me up to speed on the use of the material simulation codes and the science behind them is much appreciated. Nong, Levi and Jerry, and other lab mates made learning DFT much fun!

My journey so far through MIT has been made exciting by the different people I have met: lab mates, room mates, TAs and co-workers. TheBridgeInitiative, MISTI-Israel, ImpactLabs, MIT-GCF Tang Small Group and the MIT Energy Club were a big part of my experience. I would like to appreciate the work and friendship of Akinola Oyedele, Dixia Fan, Nwike Iloeje, Xi Rong, Joy Ekuta, Chibueze Amanchukwu, Heather Beem, Yetunde Alo, Yin-Tat Lee, Kemi Adeyemi, Amara Uyanna and Chika Ugboh and the mentorship of Kunle Adeyemo, Mrs Iyabo Attah, Rotimi Awoleke and the good folks at EducationUSA Lagos. Thank you all for believing. :)

Contents

List of Figures

List of Tables

Chapter 1

Introduction

1.1 Background

The United States currently meets 85% of its energy needs by burning fossil fuels. [4] Beginning from the industrial revolution, this has resulted in increasing concentrations of greenhouse gases in the atmosphere and concomitant rise in atmospheric temperatures (Fig. 1-1). Since carbon dioxide is the major greenhouse gas (Fig. 1-2), it is of interest to find ways to capture it, particularly at source. There are currently three approaches to this: direct usage, sequestration and conversion. In the first case, carbon dioxide has some interesting but rather limited uses in beverages, fire extinguishers, oil recovery, etc. [5] Perhaps a better-studied case is that of physical capture of the gas. This method, known as Carbon Capture and Storage (capture, compression, transportation, and storage of CO_2 in suitable subterranean geological reservoirs) [6] is a large-scale approach which may be limited by cost and our understanding of the long-term capacity of geological formations to hold CO_2. Moreover, capturing and compressing CO_2 may increase the fuel needs of, for example, a coal-fired CCS plant by 25-40%. [7] These and other system costs are estimated to increase the cost of the energy produced by 21–91% for purpose built plants, and even more for existing ones. [7] There are concerns that safe and permanent storage of CO_2 cannot be guaranteed and that even very low leakage rates could undermine any climate mitigation effects. [8, 9, 10]

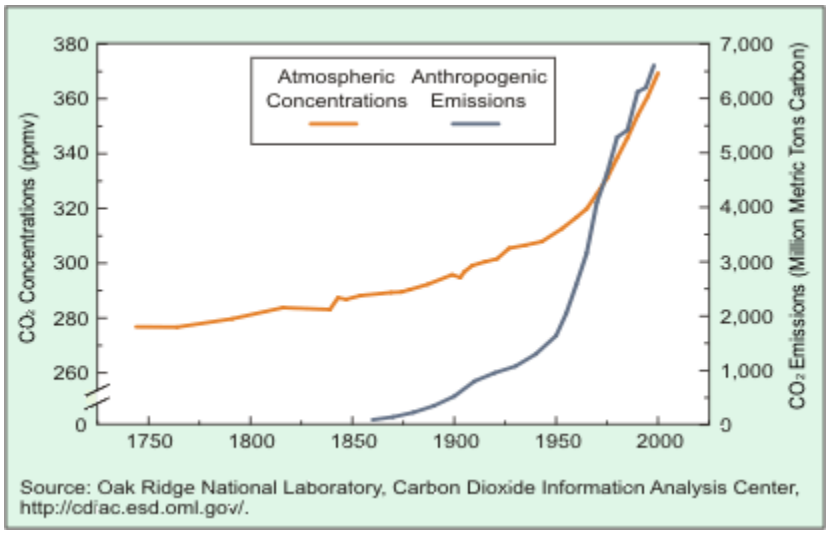

Figure 1-1: Trends in Atmospheric Concentrations and Anthropogenic Emissions of Carbon Dioxide.

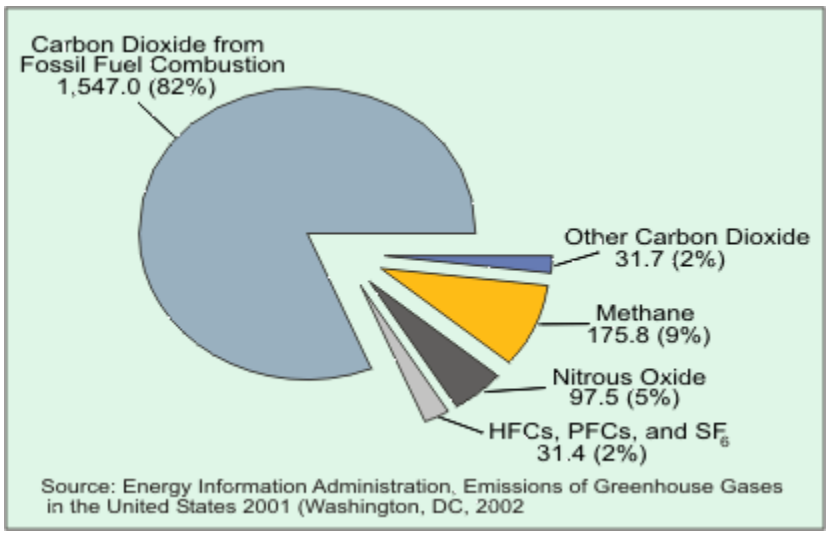

Figure 1-2: U.S. Anthropogenic Greenhouse Gas Emissions, Percentages, 2001.

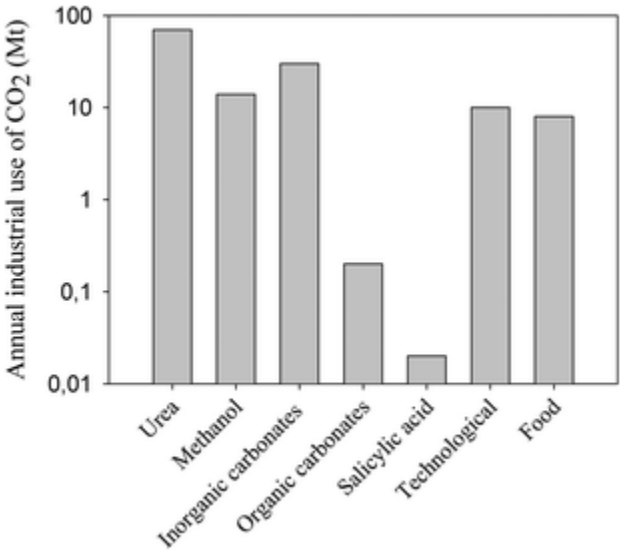

Figure 1-3: Annual industrial use of CO_2. Note the vertical axis is logarithmic. Adapted from Ref. [1].

The third approach, chemical conversion, may be the best option yet if we are able to find cheaper ways to achieve the fixation. Since carbon and oxygen are both key elements in organic chemistry, there are a wide range of chemicals (Fig. 1-4) that can at least theoretically utilize CO_2 as a feedstock for production, including organic acids, alcohols, esters, and sugars which have important commercial uses. [11, 6] For example, methanol, which is the basic chemical building block of paints, solvents and plastics, has innovative applications in energy, transportation fuels [12] and fuel cells. It had a global demand of 45.6 million metric tons and generated $36 billion in economic activity in 2010 [13]. Another potential large scale use of CO_2 is the production of cyclic carbonates. These have several commercial applications due to their use as chemical intermediates (e.g for dimethyl carbonate production) [14] and as aprotic polar solvents. [15] A particularly important and growing application of cyclic carbonates is their use as electrolytes in lithium ion batteries. [16] Practically, however, CO_2 is utilized to a very limited extent in industrial production processes. Fig. 1-3 shows some trends in actual CO_2 use. We see that scale of conversion to methanol is comparable to that of the technological uses (primarily enhanced oil recovery) though the former has a much greater demand than the latter. This is partly due to the fact that the most efficient reactant for the conversion is frequently

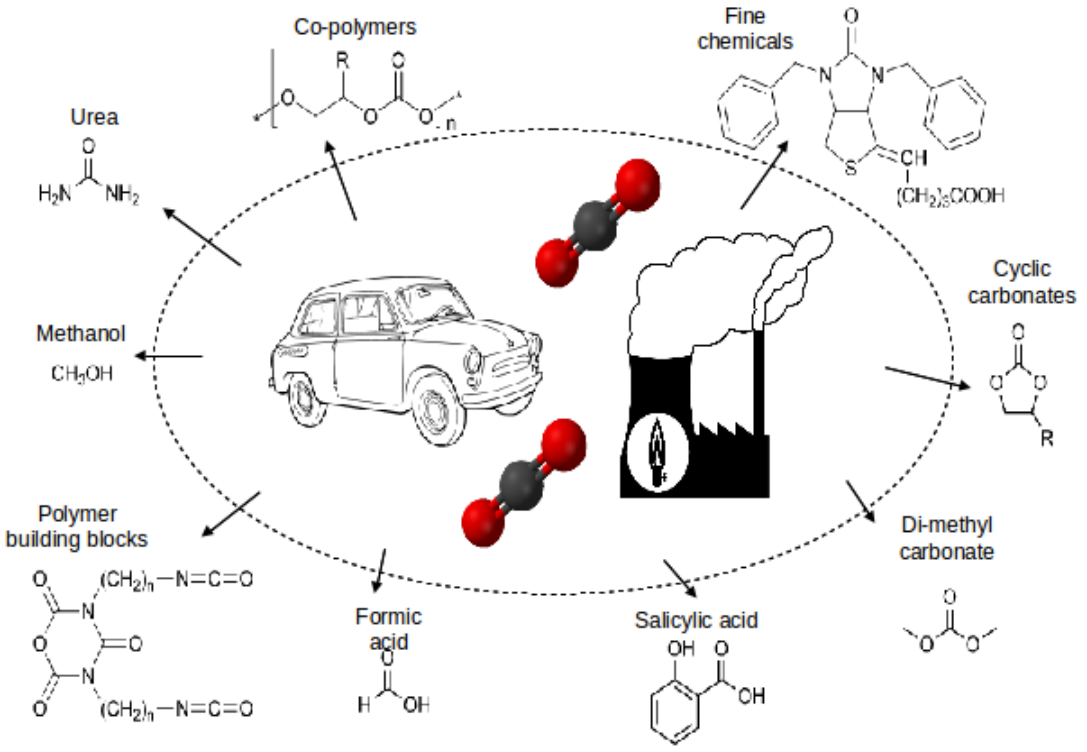

Figure 1-4: Potential products of carbon dioxide conversion.

not CO_2. For example, in the industrial production of methanol, a mixture of CO and H_2 (syngas) is the primary feedstock as these are much easier to obtain (by secondary conversion from natural gas) and a relatively small amount of CO_2 is only fed into the reactor to ensure conversion of any unreacted H_2. Another stumbling block to the adoption of CO_2 as a choice reactant is the high energy and financial cost of the conversion process itself. For example, commercial production of cyclic carbonates relies on quaternary ammonium or phosphonium salts as catalysts which require the use of high temperatures and pressures. Under these conditions, CO_2 fixation is a net producer rather than consumer of CO_2 due to the energy required to heat and pressurize the reactor and reactants. [17] These challenges explain why the current industrial usage of CO_2 is only 0.5% of the 24Gt/yr total anthropogenic CO_2 we produce.[1] This obvious gap has led many researchers to investigate ways to improve the CO_2 fixation process.

1.2 Energetics of reactions

To understand the challenge surrounding CO_2 conversion, we first need to discuss the energetics of reactions and the role of catalysts. Most reactions involve many intermediate steps between the reactants and products but can be considered in a simplified way as to be a one or two step process. Figure 1-5(a) shows a pathway from energy to product in a one-step exothermic process. Even though the product is more stable (lower in energy) than the reactant, the process will need an energy input $\triangle E^a$ to transform the reactant state to the transition configuration. The rate constant of the reaction k is related to the activation energy $\triangle E^a$ by

$$k = ve^{-\frac{\triangle E^a}{RT}} \tag{1.1}$$

and the rate of the reaction by

$$r = k[A]^n[B]^m[...]^{\cdots} \tag{1.2}$$

for the reaction $nA + mB + ... \longrightarrow pC + qD + ...$. v is the "attempt frequency", R is the molar gas constant and T is the temperature in Kelvin. $[A]$, $[B]$, ... are the concentrations or partial pressures of the reactants. Obviously the rate of a reaction is most influenced by the activation energy $\triangle E^a$. The role of a catalyst is to lower this energy and thereby increase the rate of reaction. In industrial and laboratory measurements, the performance of a catalyst is given in terms of the turn-over frequency (TOF), the number of reactant molecules the catalyst is able to convert per time.

The same definitions as above apply to Figure 1-5(b) for a one-step endothermic process. When there are many steps as in Figure 1-5(c), it is useful to define which of the intermediate steps is the most important. For example, if $\triangle E_1^a >> \triangle E_2^a$, then step 2 is the more important step and is defined as rate-limiting.

For all the sub-figures in Fig. 1-5, the exact pathway between the reactants and

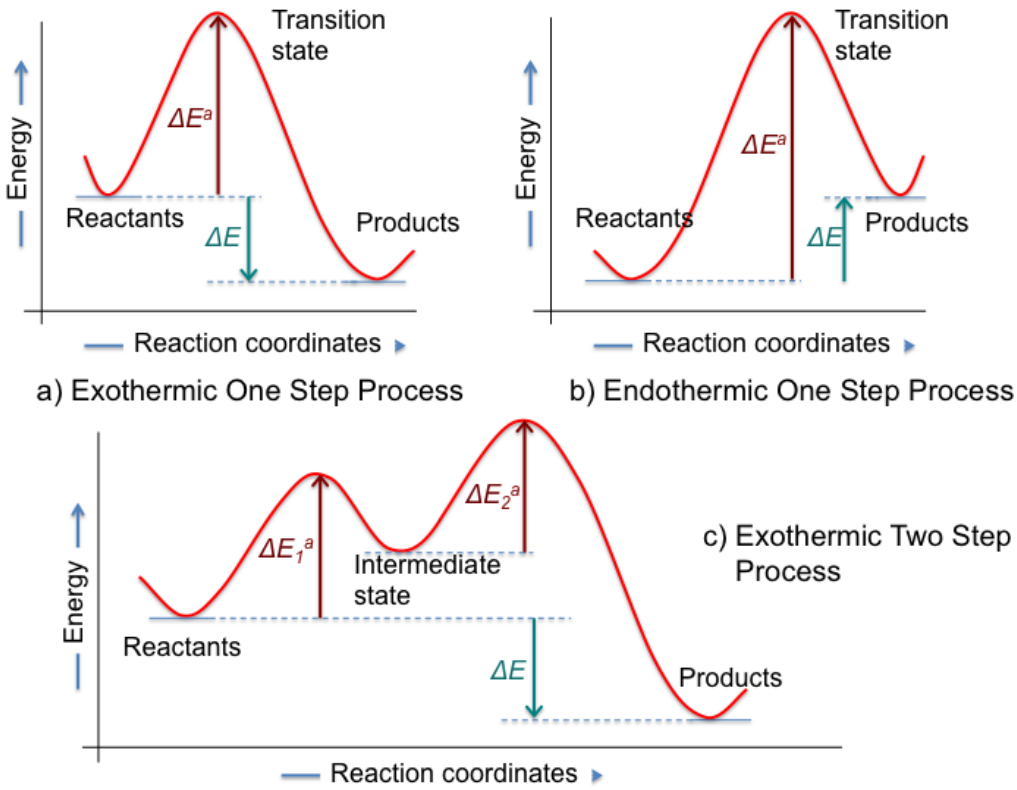

Figure 1-5: Reaction energetics diagram for an a) exothermic one-step process, b) endothermic one-step process and c) exothermic two-step process.

products is dependent on the catalyst and reaction conditions. However, the relative energies of the start and end states are affected only by the phases of the substances. Therefore the goal of catalysis science has been to influence the reaction pathway such that the activation energies for the most important steps are lowered. This may involve finding ways to stabilize (lower the energy of) the important intermediates or changing the pathway such that transitions to new intermediates are thermodynamically favorable.

As a practical example, we consider the conditions that need to be met for CO_2 conversion and utilization to become commercially and environmentally feasible. These include:

- The co-reactants should be easily and cheaply obtainable on a large scale and from renewable resources.

- Reactions should proceed under (relatively) mild conditions (i.e low pressures

and temperatures).

- The catalyst or system should have a high selectivity for CO_2 (so there is minimal requirement to first purify waste-CO_2 streams)
- There should be a relatively constant turnover to product irrespective of CO_2 source (i.e resistance to poisoning).
- The catalyst should be stable and made from earth-abundant elements in order to have reasonable cost and scale impacts.
- Energy required by the process should come from a non-fossil fuel source or by coupling with an exothermic process.
- The catalyst should enable a high product selectivity and/or control over type of product, e.g tuning of reaction conditions to yield different organic compounds during hydrogenation of CO_2.

As decades of research have proven, meeting even some of these goals is extremely challenging. Progress has been made but not many approaches have ever become efficient enough to be used outside of the lab. In Chapter 2, we will review some of these approaches and discuss the catalysts used.

1.3 Our Approach: Dynamically Tunable Catalysis

According to Sabatier's principle, the best catalyst for any particular reaction binds the reactants and product species moderately to the surface. If the catalyst binds the species too weakly, the reaction rate will be slow due to low coverage of reactants. On the other hand, if the intermediates are bound too strongly, the rate will be low because the products are not frequently desorbed. Therefore, the best catalyst invariably compromises on the interaction with the molecules involved in the reaction. These concepts are illustrated in Figure 1-6. Since both adsorption and desorption are in principle beneficial to a reaction, if a surface could be designed that binds reactant intermediates strongly and easily desorbs products, the reaction rate would

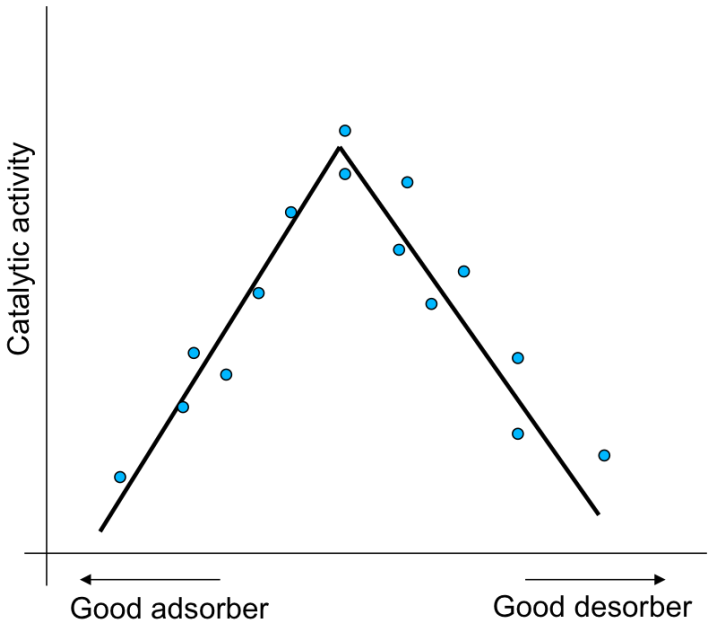

Figure 1-6: Sabatier's principle illustration. The points indicate different catalyst materials.

be greatly improved. The overall goal of the current project is to utilize the properties of a regular CO_2 catalyst (ZnO) and a ferroelectric ($PbTiO_3$) to design such a catalyst for carbon capture. The ferroelectric (a material which has a spontaneous reversible electric polarization) provides a way to manipulate the surface chemistry of the ZnO catalyst depending on the direction of the polarization.

Imagine a catalyst which can be in two states: 1 and 2. As shown in Fig. 1-7(a), consider the case where the pathway for one reaction has different energetics at different states of the catalyst. To simplify the illustration, the reaction is depicted as having two transition states. The stability of these transition states are different when the catalyst is in state 1 versus state 2, such that a combined lower-energy (and hence faster) reaction pathway can be constructed if the catalyst can be switched between states 1 and 2 *in-situ*. In principle, by constantly switching between states 1 and 2, the net reaction pathway will be a combination of the lower pathway for the first step and the lower pathway for the second step (Fig. 1-7(a)(iii)).

Another example of the utility of a catalyst with switchable properties is illustrated schematically in Fig. 1-7(b) where we consider the case in which there are competing

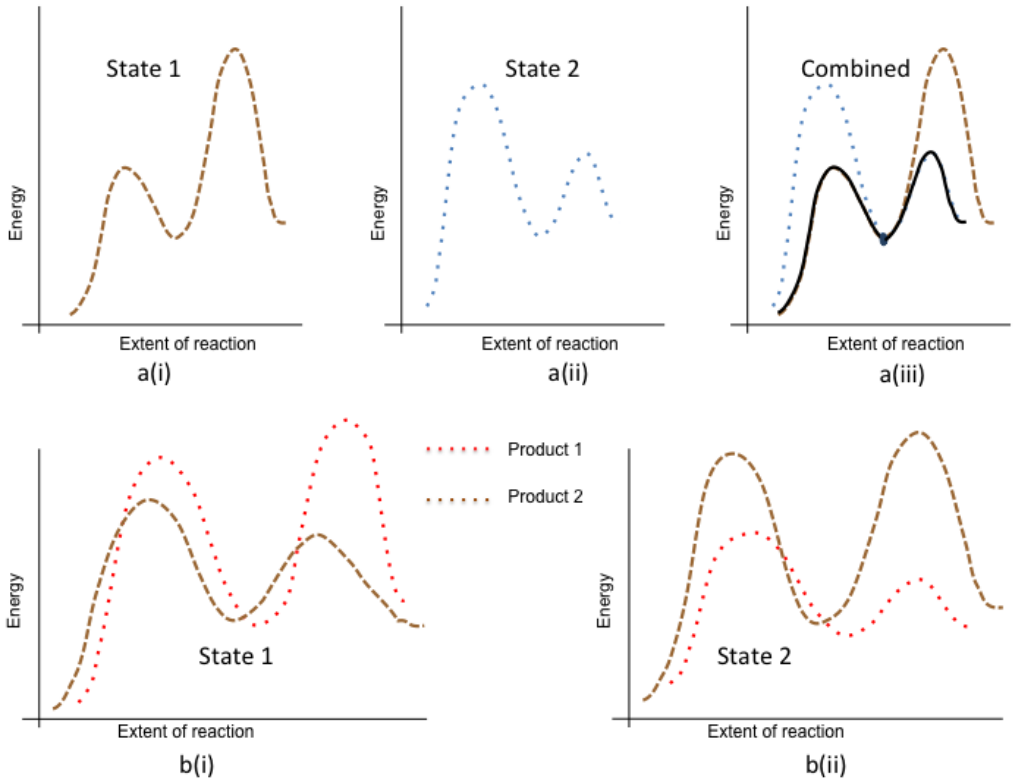

Figure 1-7: Illustration of tunable catalysis used to a) control the energetics of one reaction pathway, and b) guide a reaction towards a particular product among competing reactions.

products (and therefore reaction pathways) given the same reactants. If the energetics for product 1 are favorable at one state of the catalyst while the energetics of product 2 are more favorable for the other, we can imagine the possibility of suppressing (or promoting) specific reactions as necessary. For example, in Fig. 1-7(b)(i) where the catalyst is at state 1, the product from the reaction will be mostly product 2. On the other hand, at state 2, the product from the reaction will be mostly product 1 since the catalyst is at state 2 (Fig. 1-7(b)(ii)). If these scenarios are possible, we would have a means to design for the selectivity of a catalyst towards desired products and/or a method to inhibit the formation of undesirable ones.

The states 1 and 2 could in principle be obtained reversibly by employing external signals such as an electric or magnetic fields or light. We define a catalyst of this type as dynamically tunable. In this thesis, we will describe an analysis of the use of a ferroelectric as a means of achieving varied states at the surface of a ZnO catalyst.

This novel approach provides a potential means to go beyond the limits of Sabatier's principle which has governed all known catalysts investigated in the past 255 years of catalysis science.

1.4 Objective and structure of this thesis

The goal of this thesis is to apply density functional theory to understand whether/how a perovskite influences the surface chemistry of a (ZnO) catalyst in order to add tunability as described in Section 1.3. The rest of this thesis is organized as follows. In Chapter Two we review the state of art in CO_2 reactions of particular interest: conversion to methanol and cyclic carbonates. Chapter Three provides a background on ferroelectrics and explains why perovskites are so widely used. Chapter Four introduces the theory behind the primary method used in this study, Density Functional Theory. In Chapter Five we discuss the detail of the computations and present the results of our work to determine the best functional for describing the CO_2/ZnO/$PbTiO_3$ system. In this chapter, we also investigate whether or not an electrode (which will be present in experiments or any real devices for polarization switching) needs to be introduced in our computations. Chapter Six reports our theoretical results for ZnO polar $(11\bar{2}0)$ and non-polar (0001) slabs which will be used as benchmarks for calculations reported in Chapters Six and Seven. Chapters Six and Seven discuss polar and non-polar epitaxial ZnO on $PbTiO_3$ respectively. The surfaces and interfaces are described and the catalytic properties for CO_2 adsorption and dissociation are investigated. In the final chapter, we discuss the significance of our results and briefly describe the next steps in this investigation.

Chapter 2

Review of CO_2 conversion

2.1 Introduction

A large energy input is generally required to transform CO_2. One simple way to achieve a lower energy requirement for a CO_2 conversion process is to utilize a high energy co-reactant (e.g H_2 rather than H_2O) and optimize the reaction towards a low-energy product (such as urea or methanol rather than say, ethene). But even then there is some barrier for the process (Figure 2-1). The focus of most research is therefore how to reduce the activation energies E_a of the reactions after carefully choosing a process that is sufficiently exothermic at reasonable conditions. This is done by a judicious selection or engineering of catalysts. In this chapter, we will discuss the state of the art in the catalysis of CO_2 reactions towards methanol and cyclic carbonate production. As discussed in the previous chapter, these have several commercial applications due to their use as fuels and chemical intermediates (methanol), and as aprotic polar solvents and lithium-ion battery electrolytes (cyclic carbonates).

2.2 CO_2 conversion to methanol

The industrial process for the production of methanol utilizes synthesis gas (from coal or natural gas) containing CO and H_2 along with a small amount of CO_2 in the following reaction:

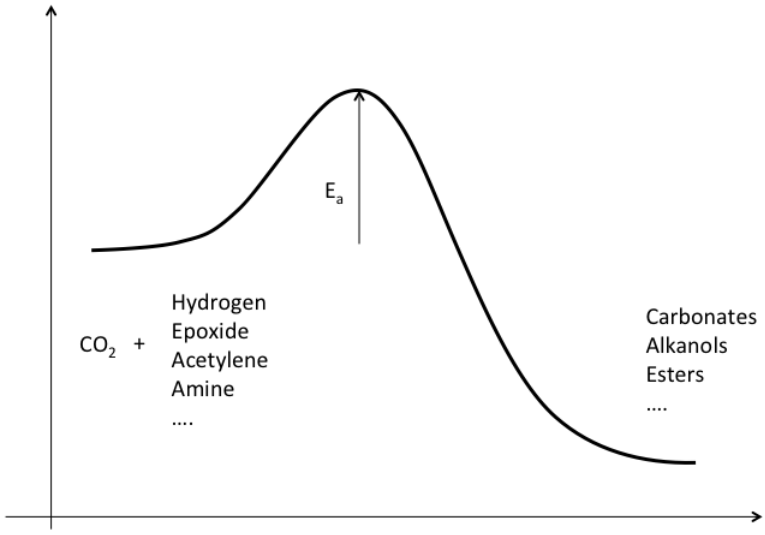

Figure 2-1: Conversion of CO_2.

$$3CO + 9H_2 + CO_2 \rightarrow 4CH_3OH + H_2O$$

This reaction is efficiently catalyzed by a copper/zinc oxide based catalyst. For yet unknown reasons this catalyst does not work as well for pure CO_2, where the reaction is given by: [18]

$$CO_2 + 3H_2 \rightarrow CH_3OH + H_2O$$

where $\triangle H^o$ for this reaction is -137.8KJ/mol. [19] Because the formation of methane is even more favorable ($CO_2 + 4H_2 \rightarrow CH_4 + 2H_2O$, $\triangle H^o = -259.9$KJ/mol), methane evolution is almost always a competing process in methanol synthesis from CO_2 depending on the conditions. [20] Another possibility is the reverse water-gas-shift reaction ($CO_2 + H_2 \rightarrow CO + H_2O$, $\triangle H^o = 41.2$KJ/mol) which may be favorable at high temperatures and pressures.

Catalysts for CO_2 hydrogenation to methanol can be classified into the following categories:

2.2.1 Cu- and Zn-based catalysts

Most of the catalysts with the best reactivities for CO_2 hydrogenation contain pure Cu or Cu and Zn doped with some other metal(s). Pure Cu is rather ubiquitous for electrochemical conversions [20] since it has the best performance among metals considered in the literature. Hori *et al.* [21] showed that the products in the electrochemical process include hydrogen, methane, formic acid, ethene and CO, with the relative proportions strongly dependent on the electrode potential. For the heterogenous catalysis processes, Cu/ZnO doped with Cr, Zr or Th gave reasonable performance as catalysts.

2.2.2 Noble metals

Pd supported by certain oxides is the most commonly used noble metal catalyst for CO_2 hydrogenation to methanol. Ramaroson *et al.* [22] found that La_2O_3 showed a >80% selectivity for methanol formation from CO_2 and H_2. On the other hand, supports of SiO_2, Al_2O_3 and TiO_2 produced mostly methane. Other researchers have characterized Pd-ZnO catalysts supported on multi-walled carbon nanotubes (MWCNTs) [23], Pd-CeO_2 [24] and Pt-SiO_2 catalysts [25].

2.2.3 Metal carbides

Transitional metal carbides have been shown to have similar catalytic properties for CO_2 hydrogenation to methanol as most common transition metals. [26] Therefore they are potential substitutes for the more expensive metals. Investigations of these metals include work on Mo_2C, Fe_2C, and WC reported in Ref. [27].

The development of most of these catalysts have largely involved trial and error. In recent years, systematic analyses and the development of faster computational methods for modeling of catalysts have led to more deliberate catalyst design for CO_2 conversion to methanol such as Ref. [28].

2.3 Conclusion

In this chapter, we reviewed the development of catalysts for CO_2 fixation. So far, research that led to these approaches have been largely trial and error, and are severely handicapped by the poor understanding we have of atomistic processes during these conversions. For example, the conversion of syngas to methanol using $Cu/ZnO/Al_2O_3$ catalyst has been commercialized since 1966 but we do not yet completely know how the catalysis takes place. However because of the many studies of the process, we do have useful starting points for designing a catalyst for the related CO_2 to methanol conversion process. On the other hand, the process of CO_2 fixation to a cyclic carbonate over an oxide catalyst has been shown to be simple addition. It should therefore be possible to use state-of-the-art computational tools to design an excellent catalyst for this reaction since the mechanistic process is much simpler.

In designing catalysts that meet some of the criteria listed in Section 1.2, we may need to go beyond trial and error and methods which are inherently limited by Sabatier's principle. In this thesis, a dynamically tunable catalysis method that in principle adds the possibility of dramatically changing reaction energetics and pathways such that product selectivity and mild reaction conditions are possible is developed.

Chapter 3

Ferroelectrics

3.1 Introduction

A ferroelectric is a material that has a spontaneous electric polarization. Consider Figure 3-1 depicting three materials A, B and C. Most materials (such as material A) do not contain electric dipoles, so when an electric field is applied, the polarization induced in the material is a linear function of the field, the slope of which is the permittivity. Material B is shown having a random arrangement of dipoles which cancel out. If an electric field is applied, these dipoles align with the field thereby inducing polarization. Under a slowly changing field, the response curve with an enhanced non-linear polarization as shown is obtained. This material is described as paraelectric. In Fig. 3-1(c), the dipoles are already mostly aligned in some preferred direction. When an electric field is applied across the material, this spontaneous polarization gets strengthened as any unaligned dipole lines up in the direction of the field (if in the same direction) or all the dipoles reverse direction (if the field points in the opposite direction). A cyclic field across this material will give a response curve which has an hysteresis effect as shown. Normally, a ferroelectric material becomes paraelectric above T_c, its Curie temperature.

Ferroelectrics are important precisely because of their spontaneous switchable polarizations and non-linear permittivity. Ferroelectric capacitors for example can be made smaller than regular dielectric capacitors because of their high permittivity.

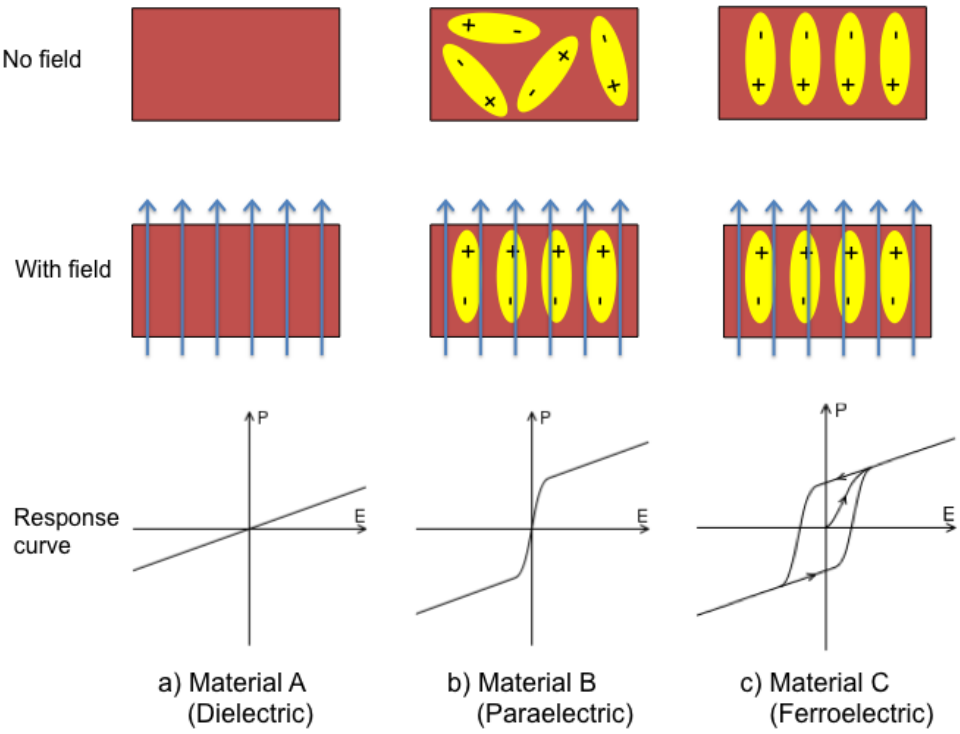

Figure 3-1: Classes of materials based on behavior under the influence of an electric field.

In addition, this capacitance is tunable. The hysteresis effect is useful for memory applications such as in ferroelectric random access memories (FeRAMs) for computers and RFID cards. Also, since ferroelectric materials are necessarily pyroelectric (can generate a voltage due to a temperature difference when heated or cooled) and piezoelectric (can generate electric charge when pressure is applied) to some degree, they are useful for sensor applications in for example, fire and vibration sensors and ultrasound machines. Ferroelectrics have also found applications in catalysis. This will be discussed in a separate section.

3.2 Perovskites

Perovskites are the most common types of ferroelectrics. They have the formula ABC_3 where A is an alkali or alkali-earth metal, B is a transition metal and C is most commonly oxygen. Aside from their ferroelectric properties, perovskites are interesting materials due to a variety of solid state phenomena (band gap, polarization, metal-insulator transitions, piezoelectricity, collossal magnetoresistance, various types of magnetic and orbital ordering, and potential for coupling between different order parameters) they exhibit. These properties are frequently tuned by changing the ions at the A or B sites or forcing departure from the ideal stoichiometry by strain engineering.

As shown in Figure 3-2, the spontaneous polarization in a perovskite is primarily due to a displacement of the B-site cation relative to the center of the oxygen octahedral (if the paraelectric phase is cubic such as in $BaTiO_3$ and $PbTiO_3$). A similar distortion occurs for perovskite oxides with an hexagonal or rhombohedral structure such as $LiNbO_3$, $ZnSnO_3$ and $BiFeO_3$.

Perovskites have found many applications because of their tunable properties. The identity of the A and B cations can be changed or mixed as desired to yield many different materials with varied properties. It has also been found that the lattice constants of most perovksites can be changed, inspiring the field of study now known Strain Engineering. By straining the lattice constants, several properties have been

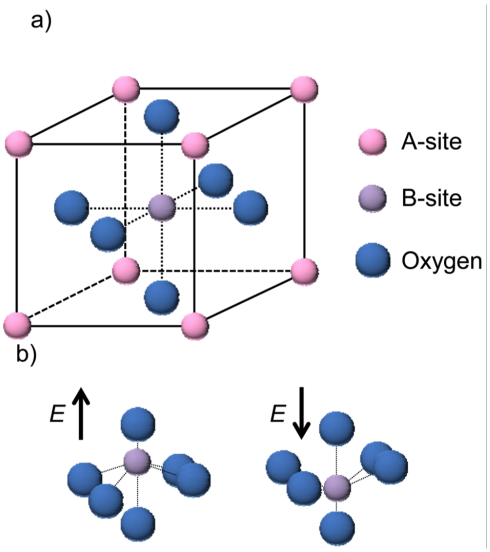

Figure 3-2: Perovskite structure showing distortion of the B-site cation relative to the center of the oxygen octahedral.

tuned, including semiconductor-metal transitions, electron mobilities and band gaps. Also, when different perovskites with similar lattice constants are epitaxially grown to form superlattices, interesting phenomena such as 2D gases at the interfaces is possible.

3.3 Ferroelectric materials as catalysts

The direction of the ferroelectric polarization has been demonstrated to have an effect on the surface chemistry of ferroelectrics. The first to demonstrate this for a ferroelectric was Parravano who showed that the rate of CO oxidation over $KNbO_3$ and $NaNbO_3$ significantly increased around the Curie temperatures of the catalysts. [29] A more recent experimental study of catalysis on bare ferroelectric surfaces is that of Yun and co-workers. They measured the temperature programmed desorption (TPD) data for different kinds of molecules and showed that 2-propanol has a desorption peak temperature 100K greater on the negatively polarized surface compared to the positively polarized one. [30] This means that the adsorption energy is much greater on the negatively polarized surface.

The internal electric field in ferroelectric catalysts and the polar surface termi-

nations can mitigate electron-hole recombinations when used for the photocatalysis and this has resulted in several studies on the possibilities of using ferroelectrics as solar cell materials and photocatalysts. [31] Another interesting catalytic application of bare ferroelectrics such as $BaTiO_3$ and $PbTiO_3$ is the combustion of methane[32]. An exciting phenomenon on these materials for hydrocarbon-related catalysis is the difference in adsorption properties of ethanol and methanol on oppositely poled surfaces. It was found that ethanol adsorbs more rapidly on negatively poled $BaTiO_3$ [33] in contrast to methanol which adsorbs more rapidly on positively poled $BaTiO_3$ [34]. This highlights the intriguing possibility of tuning the surface of the catalyst for selectivity towards methanol or ethanol.

The effect of ferroelectrics has also been shown where another layer is grown over the ferroeectric. The first observation of this type of effect was by Inoue and co-workers in the 1980s. They reported that activation energy (hence kinetic behavior) for CO oxidation over a $LiNbO_3$-supported Pd catalyst significantly changed depending on the polarization of the support and the thickness of the Pb layer. [35] They found that the energy barrier varied over Pd on the positive polar surface changed from 126KJ/mol when the Pd thickness was over 0.2nm to 96KJ/mol at 0.02nm, whereas the Pd deposited on the negatively poled surface showed a constant energy barrier of 128KJ/mol irrespective of thickness. They also showed that the adsorption energy of CO and H_2 on NiO deposited on oppositely poled directions of $LiNbO_3$. [36] This phenomenon was explained using a band bending model in which the polarization of the substrate modifies the electronic distribution on the NiO surface. A theoretical paper by Kolpak and co-workers where Pt layers deposited on oppositely poled $PbTiO_3$ showed different activities for CO dissociation supports this model. [37] They showed that the increase in the available Pt *d*-states at the Fermi level of the negatively polarized substrate enhances the adsorption of oxygen atoms. Yun *et al.* [38] recently performed a similar experiment confirming these results and models.

3.4 Landau Theory

Landau Theory is a general theory explaining second order transitions in materials when a new state of reduced symmetry develops such as during a paraelectric to ferroelectric transition. For this system the variables are temperature T, polarization P, electric field E, strain η and stress σ. The free energy F is considered to be a function of polarization (three components), stress (six components) and temperature. We guess that the form of F is

$$F = \frac{1}{2}aP^2 + \frac{1}{4}bP^4 + \frac{1}{6}cP^6 + ... - EP \tag{3.1}$$

The constants a, b, and c are determined as follows: The minimum of the energy should result in the equilibrium configuration, at which

$$E = aP + bP^3 + cP^4 + ... \tag{3.2}$$

so the if we define the dielectric susceptibility χ as the differential of this equation with respect to P at $P = 0$, we will have:

$$\chi = \frac{P}{E} = \frac{1}{a} \tag{3.3}$$

If we assume $a = 0$ at the Curie point T_o, then a must be of the form $a_o(T - T_o)$. It is known experimentally that a and c are always positive. Therefore the type of transition state that a ferroelectric undergoes depends on b. Figure 3-3 shows how the free energy F changes as a function of polarization for paraelectric and ferroelectric materials. In experiments or *ab-initio* modeling, we can plot the total energy as a function of polarization as in Figure 3-3(b) and fit values of a, b and c for any ferroelectric material.

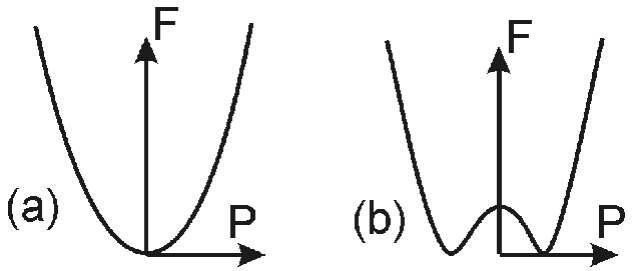

Figure 3-3: Free energy F as a function of polarization for a) paraelectric and b) ferroelectric materials.

3.5 Conclusion

The meaning of ferroelectricity has been explained and a class of ferroelectric materials, perovskite oxides have been described. The use of these materials as catalysts, both by themselves and as support for other catalysts is explored. We find that the ferroelectric changes in the materials offer a means to control the adsorption properties of certain molecules and reaction energetics of some reactions even when the molecules and reactants are not in direct contact with the ferroelectric. In the final section of this chapter, we briefly described Landau theory which models phase transitions such as the one ferroelectrics undergo.

In the next chapter, we will introduce the our *ab-initio* simulation methods.

Chapter 4

Methods

4.1 Introduction

In this work, we will build computational models of materials in order to design a catalyst and simulate its performance as a catalyst for carbon dioxide conversion. This is made possible by the work of several researchers in developing computational models for materials. In the early 20's materials were modeled by simple spring-like pair potentials holding together atoms in a specified lattice. The holy grail of this method was to figure out the best interatomic potentials for certain systems and improvement of computational times. Lennard-Jones model [39], force-field potentials (e.g Ref. [40]), embedded atom model [41] and the more recent Morse potential [42] were among the most successful approaches. The methods were able to reproduce bulk properties of the materials including lattice constants, bulk modulus, crack propagation etc and are used in molecular mechanics and dynamics simulations. However, these methods failed when applied to process which had significant involvement of electrons or had changing or complicated potential fields such as in bond-breaking, solid diffusion, epitaxy and chemical reactions.

Gradual developments in Computational Quantum Chemistry beginning in the late 30's eventually solved this problem. Schrodinger's equation (Equation 4.1), a linear partial differential equation which accurately models the behavior of quantum systems, is the starting point for these methods. [43]

$$E\Psi(\mathbf{r}) = \left[\frac{-\hbar^2}{2m}\nabla^2 + V(\mathbf{r})\right]\Psi(\mathbf{r}) \tag{4.1}$$

where E is the total energy in the quantum system (collection of atoms, molecules or fundamental particles), $\Psi(\mathbf{r})$ is the wavefunction (a probability amplitude whose square is the probability density) at a point $\mathbf{r}$, $\hbar$ is the reduced Planck's constant, m is the mass, ∇^2 is the Laplacian and $V(\mathbf{r})$ is the potential energy.

Erwin Schrodinger showed that this equation can be exactly solved for the hydrogen atom. He was able to reproduce the experimental hydrogen spectral series and the energy levels of the Bohr model. However, the equation becomes quickly complicated when more electrons are introduced, per modeling of heavier elements. The many-body Schrodinger Equation,

$$E\Psi = \left[\sum_i^N \frac{-\hbar^2}{2m_i}\nabla_i^2 + \sum_i^N V(\mathbf{r}_i) + \sum_{i<j}^N U(\mathbf{r}_i, \mathbf{r}_j)\right]\Psi \tag{4.2}$$

where $U(\mathbf{r}_i, \mathbf{r}_j)$ is the interaction energy between electrons i and j becomes complicated for more than one electron.

Methods to solve this equation include Pertubation theory, the variational method, Quantum Monte Carlo, the Wentzel-Kramers-Brillouin (WKB) approximation, the Hartree Fock Method and Density Functional Theory (DFT) method. Of all the listed methods, Density Functional Theory is the most widely used because it provides a way to solve the Schrodinger equation with reasonable computational cost which scales well with system size without sacrificing too much accuracy. We briefly describe the development of DFT in the next section.

4.2 Density Functional Theory

Density Functional Theory is a computational method used to calculate the ground state properties of many body systems. It is an implementation of the Schrodinger

equation with appropriate approximations that promotes accuracy at reasonable computational costs. DFT approaches the difficult-to-solve interacting electrons problem by mapping it exactly to the easier-to-solve non-interacting electrons problem. The computational tractability comes from using functionals of the electron density rather than direct calculation of the wavefunctions.

The step that signaled the birth of DFT was the formulation of the two Hohenberg-Kohn (H-K) theorems [44] in 1964. The first H-K theorem proved that the ground-state properties of a many-body electron system are uniquely determined by the electron density that depends on the three spatial coordinates x, y and z. This makes it possible to reduce the problem of solving the N-electron Schrodinger equation having 3N coordinates to that of solving the N-electron equation having 3 coordinates. To prove the one-to-one mapping between the ground state wavefunction and density, Hohenberg and Kohn used the variational principle: that the expectation value of the Hamiltonian H obtained with the true ground state wavefunction must be less that that obtained with any other wavefunction. We have, for two wavefunctions Ψ and Ψ':

$$E_o = \langle \Psi | H | \Psi \rangle \tag{4.3}$$

and

$$E_o' = \langle \Psi' | H' | \Psi' \rangle \tag{4.4}$$

By the variational principle,

$$E_o < \langle \Psi' | H | \Psi' \rangle \tag{4.5}$$

and

$$E_o' > \langle \Psi | H' | \Psi \rangle \tag{4.6}$$

Equations 4.5 and 4.6 can be rewritten as

$$E_o < E_o' + \langle \Psi' | H - H' | \Psi' \rangle \tag{4.7}$$

and

$$E_o^{'} < E_o + \langle \Psi | H^{'} - H | \Psi \rangle \tag{4.8}$$

In real space, $\langle \Psi^{'} | H - H^{'} | \Psi^{'} \rangle = \int \rho_o (V - V^{'}) d\mathbf{r}$ and $\langle \Psi^{'} | H - H^{'} | \Psi^{'} \rangle = \int \rho_o (V^{'} - V) d\mathbf{r}$ if we assume Ψ and $\Psi^{'}$ to give the same ground state density ρ_o. Therefore if wall of quantum chemistrye sum Equations 4.7 and 4.8, we obtain:

$$E_o + E_o^{'} < E_o + E_o^{'} \tag{4.9}$$

The falseness of Equation 4.9 shows that Ψ and $\Psi^{'}$ cannot give the same ground state density ρ_o.

The second H-K theorem defines an energy functional and proves that the correct ground state electron density minimizes this functional. Kohn and Sham[45] in 1965 combined these two theorems to develop a method of finding the ground state energy from the electron density. They showed that the energy can be written as the sum of the kinetic energy of a non-interacting electron gas, energy from an external potential, an Hartree energy and an exchange-correlation energy, viz:

$$E = T + V_{ion}(\mathbf{r}) \rho(\mathbf{r}) d\mathbf{r} + \frac{e^2}{2} \int \frac{\rho(\mathbf{r}) \rho(\mathbf{r}^{'})}{|r - r^{'}|} d\mathbf{r} d\mathbf{r}^{'} + E_{XC} \tag{4.10}$$

The exchange correlation part of the energy is however not known and various approximations are employed. In addition, we need to find the density in order to use the above expression. Kohn and Sham's idea to obtain these is depicted in Fig 4-1. The steps in the DFT scheme are:

1. Construct the nuclear potential given the atomic types and positions in the system.

2. Calculate the Hartree and exchange correlation potentials.

3. Solve the Kohn-Sham equations to obtain the wavefunctions.

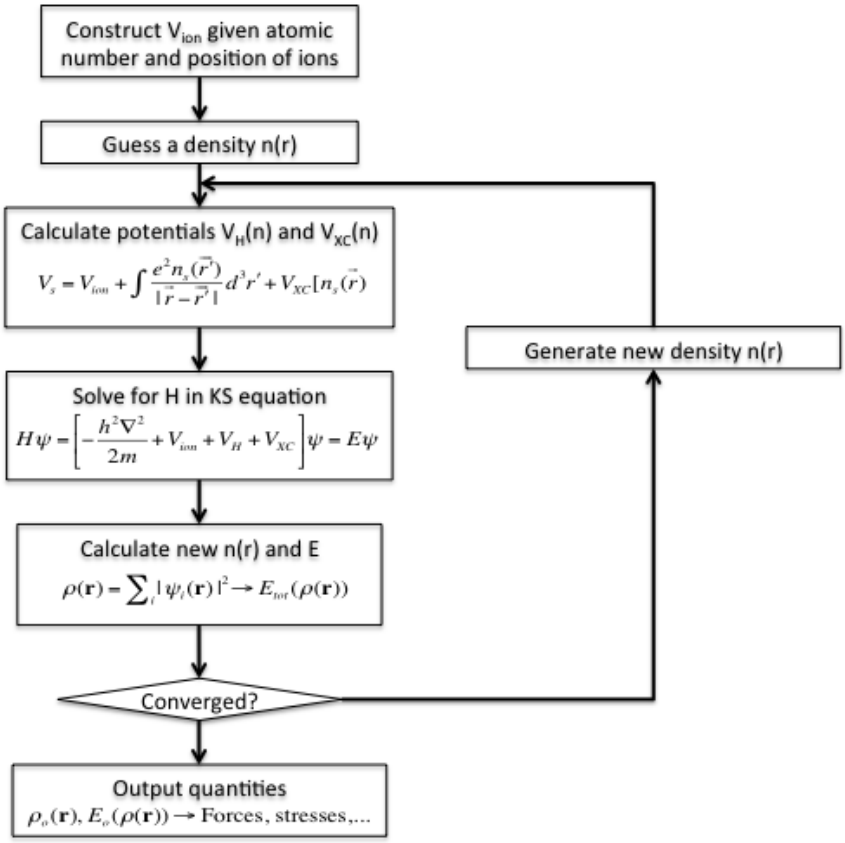

Figure 4-1: DFT self-consistency scheme.

4. Use the new wavefunctions to calculate updated values of the spatial electron densities and the total energy.

5. Stop the self-consistent field calculation when the difference between the old and new energies are sufficiently small. If only the ground state energy and density of the system are required, the calculation should end here.

6. If calculating the optimized atomic positions of the atoms in the system, also calculate the forces on each atom in step 4. Move the atoms based on the magnitudes and directions of the forces and calculate the new electronic densities and forces. Repeat this until the forces are almost zero.

7. If calculating the optimized lattice parameters and positions of the atoms, also calculate the forces on each atom and the stresses in the cell. Move the atoms and change the lattice parameters based on the forces and stresses respectively and calculate the new electronic densities, energies, forces and stresses. Repeat until the forces and stresses are sufficiently small.

A plane wave basis set is usually used to describe the Kohn-Sham orbitals (wavefunctions) of Equation 4.2. Though other functions are possible, plane waves are the most commonly used to to their simple mathematical nature and that they allow a high numerical accuracy. Plane waves are written as:

$$\psi_i(\mathbf{r}) = \sum_{\mathrm{G<G_c}} \mathrm{C_i e^{i\mathbf{G}.\mathbf{r}}} e^{i\mathbf{k}.\mathbf{r}} \tag{4.11}$$

4.3 Exchange Correlation Functionals

An unfortunate compromise in the computational tractability in the DFT method is having to approximate the electron-electron exchange correlation energy E_{XC} in Equation 4.10 since we do not know its analytical form. The simplest possible approximation of E_{XC} is the local density approximation (LDA) developed by Kohn and Sham. [46] Here the exchange-correlation energy functional depends solely on

the values of the electron density and not on its derivatives.The functional is written as

$$E_{XC}^{LDA}(\rho) = \int \rho(\mathbf{r})\epsilon_{XC}(\rho)\mathrm{d}\mathbf{r} \tag{4.12}$$

where ϵ_{XC} is the exchange-correlation energy of a homogenous electron gas (a quantum mechanical model of interacting electrons in a field of uniformly distributed positively charged nuclei) with charge density ρ. In this approximation, the correlation energy is treated as purely local.

When it is necessary to include spin polarization in the system being modeled, the local spin density approximation (LSDA) performs better than the LDA. Here two spin densities ρ_α and ρ_β representing up and down directions respectively are employed, where the total density ρ is $\rho_\alpha + \rho_\beta$. The form of the LSDA is

$$E_{XC}^{LSDA}(\rho_\alpha, \rho_\beta) = \int \rho(\mathbf{r})\epsilon_{XC}(\rho_\alpha, \rho_\beta)\mathrm{d}\mathbf{r} \tag{4.13}$$

From the foregoing, it is clear that the LSDA and LDA will be most accurate when the density changes slowly with position. When this is not the case, it is better to include nth-order variations in the density. A logical first improvement on the LDA is the generalized gradient approximation (GGA) which takes into account the gradient of the electron density at each position. That is, the exchange-correlation energy is written as a function of both ρ and $\nabla\rho$, viz

$$E_{XC}^{GGA}(\rho_\alpha, \rho_\beta) = \int \rho(\mathbf{r})\epsilon_{XC}(\rho_\alpha, \rho_\beta, \nabla\rho_\alpha, \nabla\rho_\beta)\mathrm{d}\mathbf{r} \tag{4.14}$$

This improves the accuracy of many types of calculations. Further improvement can be achieved by including higher derivatives of the density but the improved accuracy comes at a disproportionate computational cost. Therefore in this work, the generalized gradient approximation will be employed.

4.4 Pseudopotentials

The pseupotential method replaces the complicated behavior of the core electrons and nucleus of each atom with an effective potential. Since the core of the atoms (compared to the valence electrons) are not involved in the bonding properties of the atoms in the system, approximating the effect of the core by some potential should reduce the computational cost of DFT calculations even further without significant effects on accuracy when optimized for the problem at hand. The highly localized core orbitals, which are normally sharp functions mathematically represented by a large number of plane waves, are replaced with a smoother function so that the electrons in the orbitals are not treated explicitly in the calculation.

A pseudopotential is constructed by first performing an all-electron calculation to determine the potential, wavefunctions and eigenvalues of the atomic reference state. The pseudo-potential is then chosen such that the eigenvalues match that of the reference state and the wavefunction outside some cut-off radius r_c exactly matches that of the reference.

The most common forms of pseudopotentials are the norm-conserving [47] and the ultrasoft [48]. In this thesis, we will use pseudopotentials of the later type which are less computationally expensive.

4.5 Dispersion Correction (DFT-D)

Density Functional Theory is yet unable to properly describe intermolecular interactions, especially van der Waal's forces. New DFT methods have been developed to overcome this problem. Among these, the Grimme dispersion correction [49] is the most widely used since it can easily be incorporated as a correction on existing functionals and so does not significantly affect the other properties for which the functional was designed.

For the dispersion correction, the parametrization of the density functional is restricted to short electron correlation ranges and longer ranges are described by

damped $C_6 \cdot R$ terms. This correction is added to the usual Kohn-Sham energy, viz:

$$E_{DFT-D} = E_{KS-DFT} + E_{disp} \tag{4.15}$$

The dispersion energy E_{disp} is given by

$$E_{disp} = -s_6 \sum_{i=1}^{N_{at}-1} \sum_{j=i+1}^{N_{at}-1} \frac{C_6^{ij}}{R_{ij}^6} f_{damp}(R_{ij}) \tag{4.16}$$

where N_{at} is the number of atoms in the system, C_6^{ij} and R_{ij} are the dispersion coefficient and interatomic distances for the pair ij, f_{dmp} is a damping function and s_6 is a functional-dependent global scaling factor. This method has been found to be very successful. Several studies have shown that the performance for non-covalently bound systems including many pure van der Waals complexes is exceptionally good, reaching on the average the level of accuracy of quantum chemistry (e.g CCSD(T)) methods.[50][51]

4.6 Density of States

The density of (energy) states describe the number of states available for electron occupation at each energy interval in a system. It is frequently of interest to know the density of states in a system since it provides a key insight into the material's properties, for example, its band gap, electronic effects due to an interface, metallicity, etc. We can also infer or predict bonding interactions between molecules or between a molecule and a surface.

The density of states in a DFT calculation can be computed when the ground state charge density is known. It is formally defined as

$$n(\epsilon) = \int n(\mathbf{r}, \epsilon) d\mathbf{r} \tag{4.17}$$

where the local density of states, $n(\mathbf{r}, \epsilon)$ is defined as

$$n(\mathbf{r}, \epsilon) = \sum_{i}^{N} |\psi_i(r)|^2 \delta(\epsilon - \epsilon_i) \tag{4.18}$$

4.7 Nudged Elastic Band Calculations

The Nudged Elastic Band (NEB) is a method of calculating the energetics of chemical processes including chemical reactions, solid diffusion, adsorption and desorption and vacancy formation. The rates of these reactions are estimated by finding the transition states between the initial and final states (see Fig. 1-5) using the harmonic transition state theory[52]. The minimum energy path (along which the reaction energetics are calculated) is defined as the path that has the greatest statistical weight on the potential energy surface. At any point along this path, the force of the atoms is tangential to the path.

The NEB method is one of the most robust ways of finding the minimum energy path (MEP) and has been used in conjunction with classical potentials and density functional theory. [53] In the method, images of the system between the initial and final states are constructed and 'rubber-bands' are added to adjacent images. Minimizing the force on these bands results in a path that is the MEP.

Consider a system having $N+1$ images including the start and end states, resulting in the use of N bands $[R_0, R_1, R_2, ..., R_N]$ with R_0 and R_N fixed. The total force acting on an image is the sum of the forces in the elastic bands along the local tangent a 'true' force perpendicular to it.

$$F_i = F_i^s|_{||} - \nabla E(R_i)|_{\perp} \tag{4.19}$$

We then apply an optimization algorithm to move the images according to the magnitude of the force using for example a Verlet algorithm. From this, we can obtain a reaction or process pathway and hence reaction rates for any system as depicted in Fig. 1-5 and Eqs. 1.1 and 1.2.

4.8 Limitations of DFT

Even though DFT is in principle an exact reformulation of the many body Schrodinger Equation, approximations are required for the exchange-correlation energy functional. The error in the correlation part results in the local nature of LDA and GGA type functionals. This has been found to explain why common DFT methods tend to underestimate the band gaps of materials, barriers of chemical reactions, dissociation energies of ions and charge transfer ionization energies, and overestimate the binding energies of charge transfer complexes and material behavior under the action of electric fields. [54] Several methods have been devised to correct these errors. The DFT-D method [49] accounts for long range interactions using a $1/R^6$ correction term and the DFT+U adds an on-site Coulomb repulsion to (usually localized d and f) orbitals of specified atoms so as to correctly account for electron-electron interactions. Understanding the limitations (and possible remedies) of DFT is important in evaluating the results and comparing to experiments.

4.9 Conclusion

This chapter introduced the methods we will use in this thesis. The mostly widely used computational method for materials, the Density Functional Theory, is presented. The self consistent scheme for the implementation is described and the meanings of functionals and pseupotentials are explained. Some of the methods for calculating material properties (e.g Density of States) or improving DFT (e.g DFT-D) are also presented. Finally, the limitations of DFT are discussed. For the systems we will consider in this thesis, DFT with dispersion correction is expected to give results comparable to experimental data as will be shown in the next chapter.

Chapter 5

Functionals and convergence testing

5.1 Selecting a functional

In order to be sure that our DFT calculations represent the systems we are interested in investigating to a reasonable accuracy, we need to make use of the 'right' functionals. In addition, since we will introduce gas phase materials (e.g CO_2) into our systems, we need to account for long-range interactions as well. From previous studies, we know that hybrid functionals are the most accurate for molecular systems [55] and the local density approximation (LDA) [46] and general gradient approximation (GGA) [56, 57] are most widely used for solids. It is known that GGA does not represent the accurately describe all the relevant perovskites so well. [58] Since our systems are combinations of molecules, oxides and perovskites, we have a non-trivial problem of finding or fitting the right functionals. As a first step, we compared the performance of the Wu-Cohen [59, 60] functional against the more commonly used PBE [61] functional. In both we checked the effect of adding dispersion correction [62] (i.e DFT-D calculation).

5.1.1 s_6 factor for Wu-Cohen functional

The presence of dispersive van der Waals forces restrict the applicability of semi-local exchange and correlation functional within density functional theory. [63] The most

common way to correct for this is the use of Grimme's correction [49]. In his paper, Grimme calculated the values of C_6^{ij} for elements H to Xe and s_6 for BLYP, PBE, TPSS and B3LYP functionals using Equations 4.15 and 4.16. Since we do not yet know what the s_6 parameter should be for the Wu-Cohen functional, we have to calculate it.

The value of s_6 was calculated using the following method:

1. The total energies of the 22 molecular systems in the standard S22 set (Table 5.1) were calculated using the Wu-Cohen functional as implemented in PWscf [64] at a set s_6 value of 1.0. E_{disp} was then obtained using the Equation 4.15.

2. The total energy at different values of s_6 were then calculated as

$$E_{DFT-D,s_6} = E_{KS-DFT} + s_6 \cdot E_{disp,s_6=1} \tag{5.1}$$

3. Steps 1 and 2 were performed for the 17 constituent molecular systems to obtain the energies of the single molecules.

4. At each value of s_6 , we evaluated the interaction energies in each molecular system using

$$E_{int} = E_{tot} - E_1 - E_2 \tag{5.2}$$

   where E_{int} is the interaction energy, E_{tot} is the total energy of the system and E_1, E_2 are the energies of the constituent molecules.

5. Finally, the interaction energies were compared with that obtained with the Coupled Cluster Singles and Doubles quantum chemistry method (see Table 5.1). The standard deviations of the 22 interaction energies from the benchmark values were computed for each value of s_6 .

The final results are shown in Fig 5-1. By interpolation, we find the optimal value of the global scaling factor for the Wu-Cohen functional is

$$\boxed{s_6 = 0.82}$$

s/n	Name	Optimization level	Energy (eV)
1	2-pyridoxine 2-aminopyridine complex	MP2/cc-pVTZ CP	-0.7246
2	Adenine thymine complex stack	MP2/cc-pVTZ CP	-0.5303
3	Adenine thymine Watson-Crick complex	MP2/cc-pVTZ CP	-0.7099
4	Ammonia dimer	CCSD(T)/cc-pVQZ noCP	-0.1375
5	Benzene - Methane complex	MP2/cc-pVTZ CP	-0.065
6	Benzene ammonia complex	MP2/cc-pVTZ CP	-0.1019
7	Benzene dimer parallel displaced	MP2/cc-pVTZ CP	-0.1184
8	Benzene dimer T-shaped	MP2/cc-pVTZ CP	-0.1188
9	Benzene HCN complex	MP2/cc-pVTZ CP	-0.1934
10	Benzene water complex	MP2/cc-pVTZ CP	-0.1422
11	Ethene dimer	CCSD(T)/cc-pVQZ noCP	-0.0655
12	Ethene ethyne complex	CCSD(T)/cc-pVQZ noCP	-0.0663
13	Formamide dimer	MP2/cc-pVTZ noCP	-0.6921
14	Formic acid dimer	CCSD(T)/cc-pVTZ noCP	-0.807
15	Indole benzene complex stack	MP2/cc-pVTZ CP	-0.2264
16	Indole benzene T-shape complex	MP2/cc-pVTZ CP	-0.2485
17	Methane dimer	CCSD(T)/cc-pVTZ noCP	-0.023
18	Phenol dimer	MP2/cc-pVTZ CP	-0.3057
19	Pyrazine dimer	MP2/cc-pVTZ CP	-0.1917
20	Uracil dimer h-bonded	MP2/cc-pVTZ CP	-0.8877
21	Uracil dimer stack	MP2/cc-pVTZ CP	-0.4284
22	Water dimer	CCSD(T)/cc-pVQZ noCP	-0.2177

Table 5.1: Reference interaction energies of the S22 set. The data were obtained from the Benchmark Energy and Geometry Database (http://www.begdb.com).

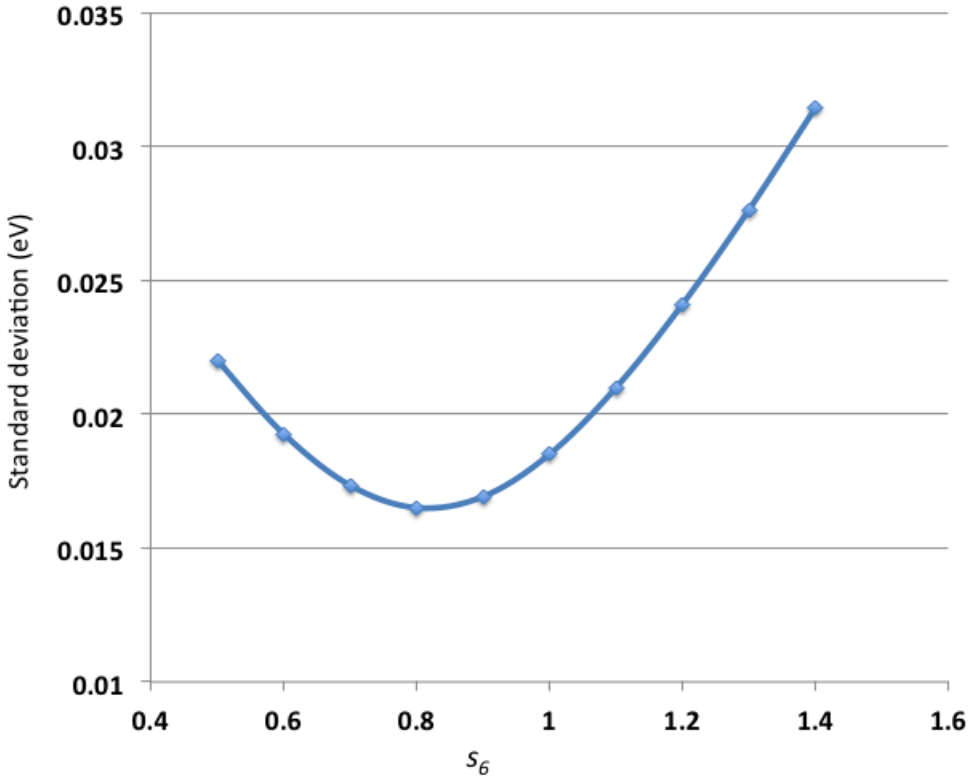

Figure 5-1: Deviation of DFT-D errors in interaction energies of the S22 set using Wu-Cohen functionals.

5.1.2 Wu-Cohen vs PBE functionals

The standard among computational scientists for how good a functional is is how well its results mirrors experimental data. The most common benchmarks for most systems are the formation energies (for solids), interaction energies (for molecular gas-phases) and adsorption energies (for where a gas-solid interaction is important). In deciding whether to use the Wu-Cohen or PBE functional, we adopted these standards. Calculations were done within DFT with and without dispersion correction and the results compared to data obtained from the NIST webbook or most commonly cited or recent papers.

Formation energies

We considered the formation energies of all possible precipitates of the $ZnO/PbTiO_3/CO_2$ system, *viz* ZnO, PbO, $\alpha-PbO_2$, TiO, TiO_2(rutile), Ti_2O_3 and $PbTiO_3$. The energies were calculated using the usual method:

$$E_{f,(A_nB_m)} = E_{tot,(A_nB_m)} - nE_{tot,(A)} - mE_{tot,(B)} \tag{5.3}$$

These energies were then compared to the values listed in the US National Institute of Science and Technology (NIST) Chemistry Webbook [65].

Interaction energies

As described in Section 5.1.1, the interaction energies for the molecular dimer systems can be calculated. We used the s_6 scaling factor of 0.82 and 0.75 for Wu-Cohen and PBE functionals respectively in the DFT-D calculations. The interaction energies were calculated using Equation 5.2 and then compared to data in Table 5.1.

Adsorption energies

We limited the adsorption energy test to the adsorption of CO_2 on the $11\bar{2}0$ non-polar and the 0001 and $000\bar{1}$ polar surfaces of ZnO. These are the surfaces of interest in this project. The adsorption energies were calculated using

$$E_{ads} = E_{ZnO+CO_2} - E_{ZnO} - E_{CO_2} \tag{5.4}$$

where E_{ZnO} is the energy of a ZnO slab and E_{CO_2} is the energy of an isolated CO_2 molecule. The data were then compared to experimental CO_2 adsorption energy such as in Refs [66], [67] and [68].

By comparing the results when different functionals are used, we find that the Wu-Cohen functional with dispersion correction is the best for our work.

To be sure that this choice of functional is reasonable not just for the types of

Subst.	Form	Wu-Cohen Dim. ($\overset{o}{A}$)	Expt. Dim ($\overset{o}{A}$)
C	Hexagonal	2.46 (0.0%), 6.89 (0.15%)	2.46, 6.70
O_2	Molecule	1.23 (1.65%)	1.21
CO_2	Molecule	1.18 (1.70%)	1.16
Pb	FCC	5.04 (1.80%)	4.95
PbO	Tetragonal	4.07 (2.00%), 5.62 (1.01%)	3.99, 5.10
PbO_2	Orthorhombic	5.13 (3.2%), 6.08 (2.01%), 5.59 (2.76%)	4.97, 5.96, 5.44
Ti	$\alpha-$HCP	2.93 (0.68%), 4.67 (0.43%)	2.95, 4.69
TiO	Cubic	4.28 (2.39%)	4.18
TiO_2	Tetragonal	4.60 (0.22%), 3.03 (2.36%)	4.59, 2.96
$PbTiO_3$	Tetragonal	3.87 (0.77), 4.22 (2.18%)	3.90, 4.13
Zn	HCP	2.62 (1.50%), 5.18 (4.65%)	2.66, 4.95
ZnO	Orthorhombic	5.68 (0.89%), 5.29 (1.73%), 3.28 (0.92%)	5.63, 5.20, 3.25

Table 5.2: Comparison of results of Wu-Cohen DFT-derived lattice constants. The values in brackets are the deviations from experimental values.

energies calculated, the lattice constants of different solids relevant to this work were checked as shown in Table 5.2.

5.2 Energy cut-off, k-point grid, slab and vacuum convergence

Cut-off and k-point grid convergence calculation were done for all the systems in Table 5.2. The results are shown in Table 5.3.

We also calculated the required spacing to simulate a vacuum over ZnO and $PbTiO_3$ slabs. By varying the spacing between the repeating slabs in the z-direction and applying a dipole correction, we were able to estimate the convergence of the surface energies. A representative plot of the total energy of a ZnO$(11\bar{2}0)$ slab is shown in Fig 5-2. It is seen that a spacing of $6\overset{o}{A}$ is more than sufficient for the ZnO surface. A similar calculation using two formula units of a symmetric PbO-terminated $PbTiO_3$

Subst.	Form	Cut-off energy (Ry)	K-point grid
C	Hexagonal	30	$5 \times 5 \times 2$
O_2	Molecule	30	$1 \times 1 \times 1$
CO_2	Molecule	40	$1 \times 1 \times 1$
Pb	FCC	45	$12 \times 12 \times 12$
PbO	Tetragonal	45	$5 \times 5 \times 5$
PbO_2	Orthorhombic	50	$5 \times 5 \times 5$
Ti	$\alpha-$HCP	50	$10 \times 10 \times 10$
TiO	Cubic	60	$6 \times 6 \times 6$
TiO_2	Tetragonal	60	$5 \times 5 \times 4$
$PbTiO_3$	Tetragonal	55	$4 \times 4 \times 4$
Zn	HCP	30	$5 \times 5 \times 5$
ZnO	Orthorhombic	55	$5 \times 5 \times 4$

Table 5.3: Converged plane wave cutoff energies and k-point grids used in calculating bulk materials.

slab showed that a spacing of $10\mathring{A}$ with dipole correction was sufficient to simulate a vacuum. In actual calculation, we added more space to account for the presence of CO_2 and methanol adsorbates.

5.3 Effect of adding an electrode

An electrode or some kind of support is necessary for most applications involving perovskites. Electrodes have been demonstrated to have significant effects on the perovskite properties. For example, Sai *et al* [69] reported that the Pt electrodes cancel 97% of the depolarizing field in thin $PbTiO_3$ thin films and thus help to maintain some polarization even in films one lattice unit thick. Here the grounded electrodes provides metallic screening that compensates the polarization charge. Arras *et al.* [70] carried out an interesting study on the effects of metal electrodes on the $LaAlO_3/SrTiO_3$ interface. They showed that changing the type of metal greatly affects the Schottky barrier, carrier concentration and lattice polarization at the interface.

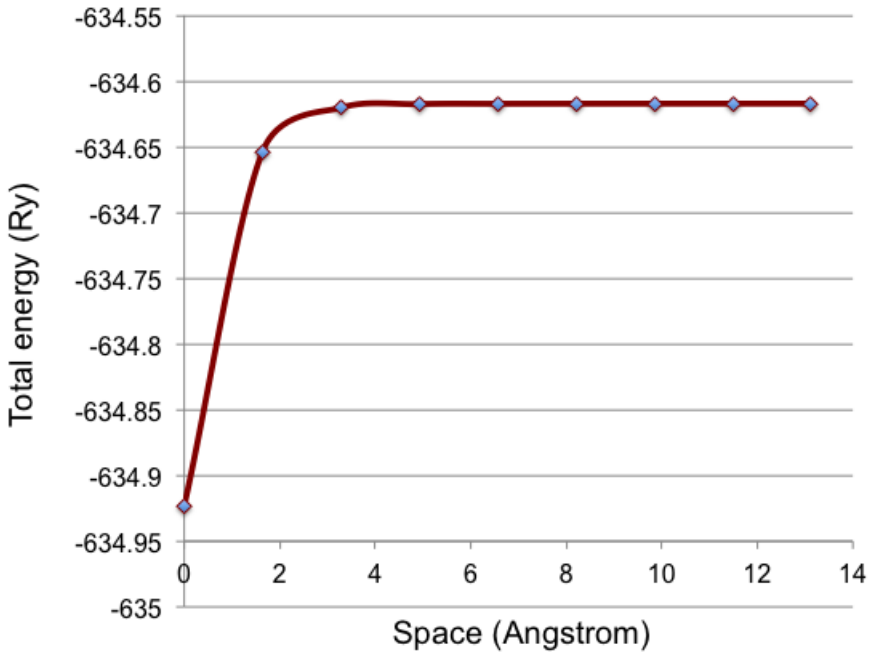

Figure 5-2: Vacuum space convergence for two layers of ZnO($11\bar{2}0$) slab.

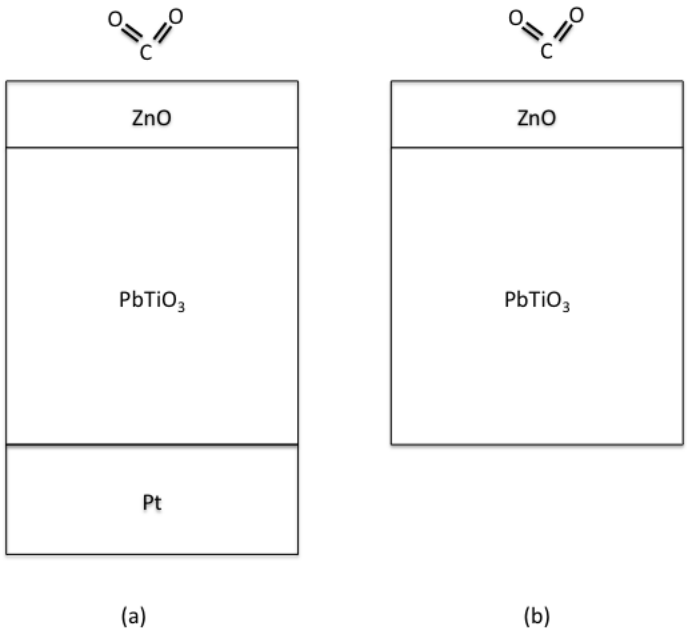

Figure 5-3: Determining the effects of platinum electrodes on surface properties. Calculations were carried out (a) with an electrode support and (b) without an electrode support.

In the light of this, it is imperative to understand how adding a metal electrode in our model of the ZnO/$PbTiO_3$ affects the ZnO surface (hence catalytic) properties. If the electrode has an effect, we will have a better understanding of phenomena at the surfaces. If it does not, then we can get away with modeling a ZnO/$PbTiO_3$ system with fewer atoms hence less computational costs.

We carry out several calculations as follows (see Figure 5-3):

- ZnO/$PbTiO_3$/Pt at both $PbTiO_3$ polarization directions
- ZnO/PbTiO3 at both polarization directions
- CO_2 adsorption on ZnO/$PbTiO_3$/Pt at both polarization directions
- CO_2adsorption on ZnO/$PbTiO_3$ at both polarization directions

We used two ZnO $11\bar{2}0$ layers, four lattice parameter thick PbO-terminated $PbTiO_3$ slab (bottom three fixed) and four layers of Pt at the bottom. We calculated the ZnO

binding energy $PbTiO_3$/Pt and $PbTiO_3$, density of states of ZnO/$PbTiO_3$/Pt and ZnO/$PbTiO_3$, and CO_2 adsorption energy on ZnO/$PbTiO_3$/Pt and ZnO/$PbTiO_3$.

5.3.1 ZnO binding energy on $PbTiO_3$/Pt and $PbTiO_3$

With the Pt and ZnO layers and the topmost $PbTiO_3$layer relaxed, we calculated the binding energy of ZnO to $PbTiO_3$ in the presence and absence of the electrode. Figure 5-4 shows the result. It is seen that the electrode has no effect of the ZnO binding. This tells us that the structure is probably as stable with and without the electrode.

5.3.2 CO_2 adsorption energy on ZnO/$PbTiO_3$/Pt and ZnO/$PbTiO_3$

Then we calculated the CO_2 adsorption energy. Figure 5-4 shows that the electrode has no significant effect.

5.3.3 Density of states of ZnO/$PbTiO_3$/Pt and ZnO/$PbTiO_3$

Finally, we calculated the electronic structure of the layers. As seen in Figures 5-5 and 5-6, there is no significant change in the electronic structure of the layer both for the up- and down- polarized catalyst when the platinum electrode is removed.

From the foregoing, it is evident the electrode is not important to consider here. Therefore for the rest of the calculations in this work, we will model ZnO/$PbTiO_3$/Pt as ZnO/$PbTiO_3$.

5.4 Conclusion

In this chapter, our work on testing functionals was presented. We showed that the proper global scaling factor for the Wu-Cohen functional is 0.82 compared to 0.75

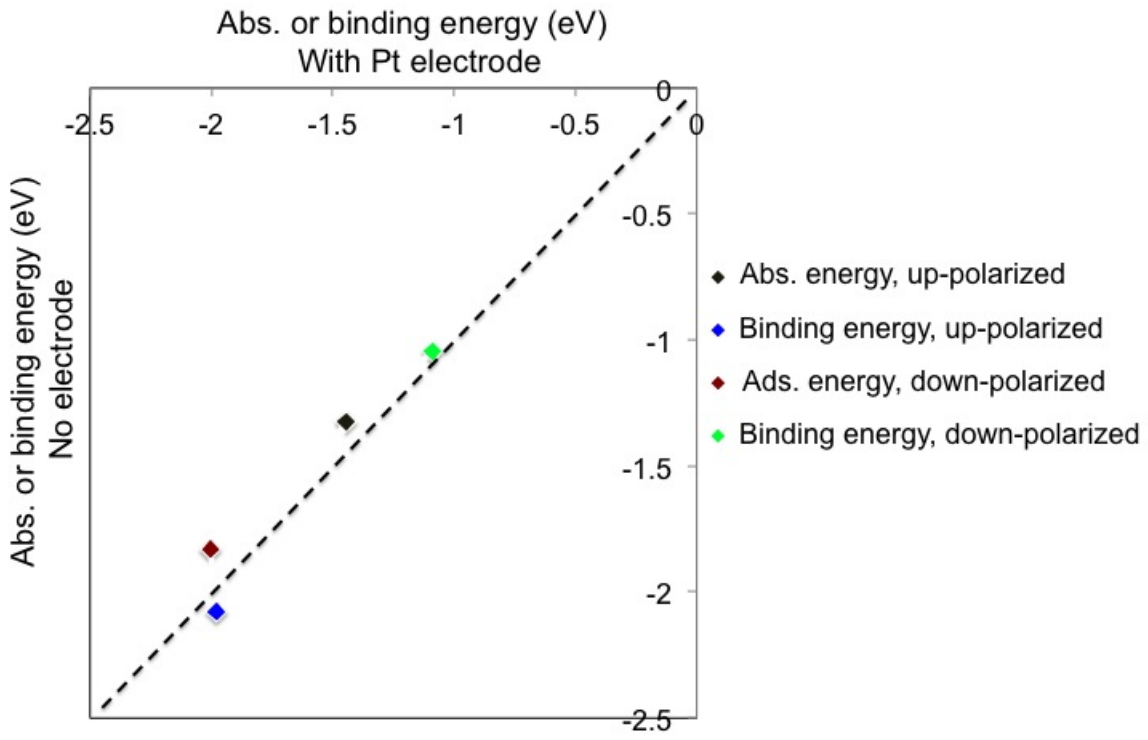

Figure 5-4: Comparing the ZnO binding energy on $PbTiO_3$ and CO_2 adsorption energy on $ZnO(11\bar{2}0)_2/PbTiO_3$ with an without a Pt electrode.

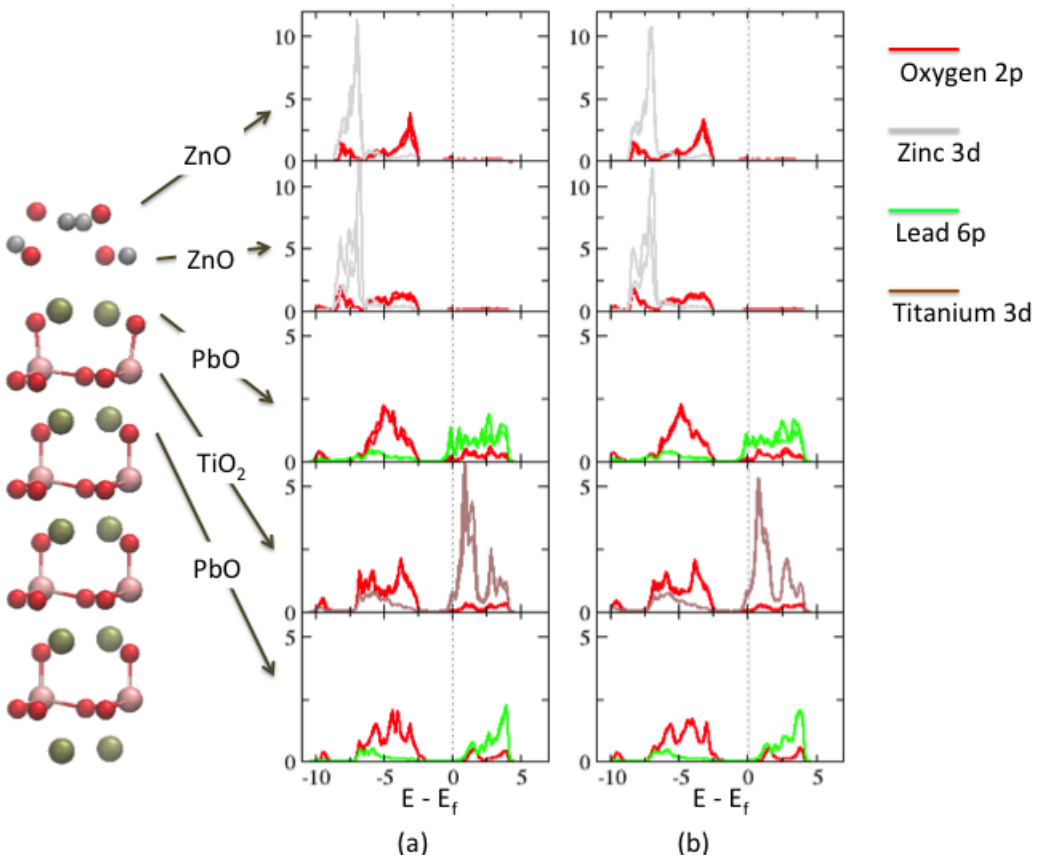

Figure 5-5: Projected densities of states for the topmost five layers of a) $ZnO/PbTiO_3/Pt$ and b) $ZnO/PbTiO_3$ for $PbTiO_3$ poled in the positive direction.

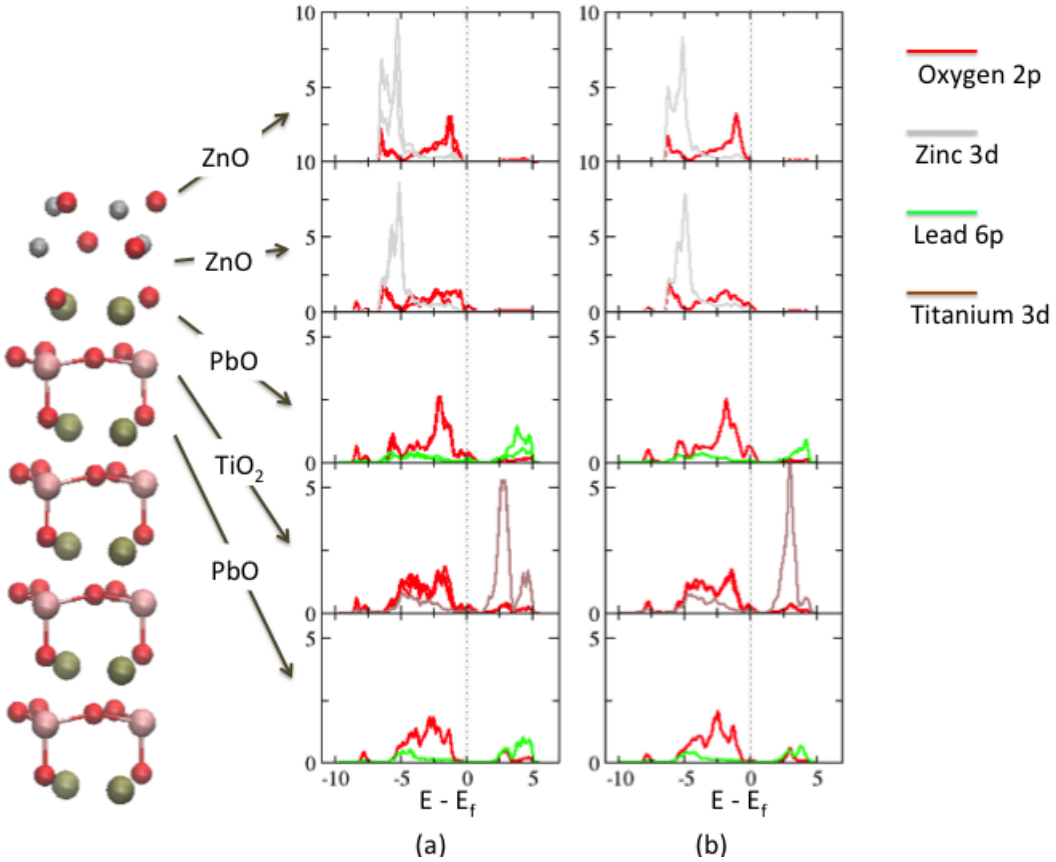

Figure 5-6: Projected densities of states for the topmost five layers of a) $ZnO/PbTiO_3/Pt$ and b) $ZnO/PbTiO_3$ for $PbTiO_3$ poled in the positive direction.

for PBE. Using this, we demonstrated that the best functional of the two to use for the CO_2/ZnO/$PbTiO_3$/Pt system is the Wu-Cohen functional. Finally, we explored the effect of adding an electrode by carrying out representative calculations using a Pt electrode beneath the perovskite. Our results showed that the electrode had little effect on the surface chemistry of the ZnO layers, and so we may model the CO_2/ZnO/$PbTiO_3$/Pt system without Pt.

Chapter 6

Surface Chemistry of ZnO($11\bar{2}0$) and ZnO(0001)

6.1 Introduction

Due to its wide band gap, gas adsorption properties and conductivity when doped, zinc oxide has found interesting electronics (e.g blue and UV light emitting diode), sensor, spintronics and piezoelectric applications [71]. In addition, when combined with copper nanoparticles, it is capable of catalyzing methanol synthesis, and has been the standard catalyst in the industrial manufacture of the chemical.

Our interest in zinc oxide stems from the latter application. As previously discussed, we are designing a novel approach to catalysis which may result in very high catalytic rates, beyond the maxima predicted by Sabatier's volcano plots. To do this, we try to tune the surface chemistry of a regular catalyst by changing the polarization of an underlying perovskite, thereby changing the structure and/or electronic properties of the surface layer. Zinc oxide is an ideal candidate to test this idea since its growth on perovskites has been well studied experimentally.

As a first step to modeling this system, we need to study bulk ZnO and the properties of its most stable surfaces. The non-polar ($11\bar{2}0$) and the polar (0001) are of interest since they are the most commonly observed growth orientations on perovksites [3, 72, 73]. In this chapter, we discuss some theory and the results of our

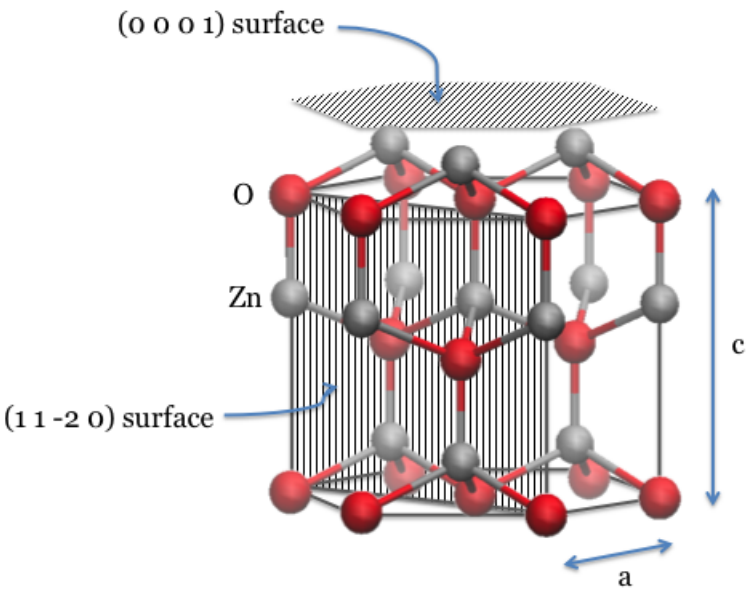

Figure 6-1: ZnO cutting planes for (0001) and $(11\bar{2}0)$ surfaces.

ab initio calculations of the atomic and electronic structure and surface chemistry of ZnO slabs.

6.2 *ab initio* calculations for non-polar ZnO $(11\bar{2}0)$

For our calculations, we carried out self-consistent density functional theory computations with a generalized gradient approximation as implemented in PWscf in the Quantum Espresso code [64]. We employ a cut-off energy of 50Ry and 5×5×1 and 4×4×1 Monkhorst-Pack k-point meshes for ZnO$(11\bar{2}0)$ and ZnO(0001) slabs respectively. All calculations correspond to zero temperature. For the local exchange correlation functional, Wu-Cohen [59] GGA was used rather than the more popular PBE because it performs better in predicting the properties of perovskites and many other molecules, surfaces and solids [60] as described in the previous chapter. Con-

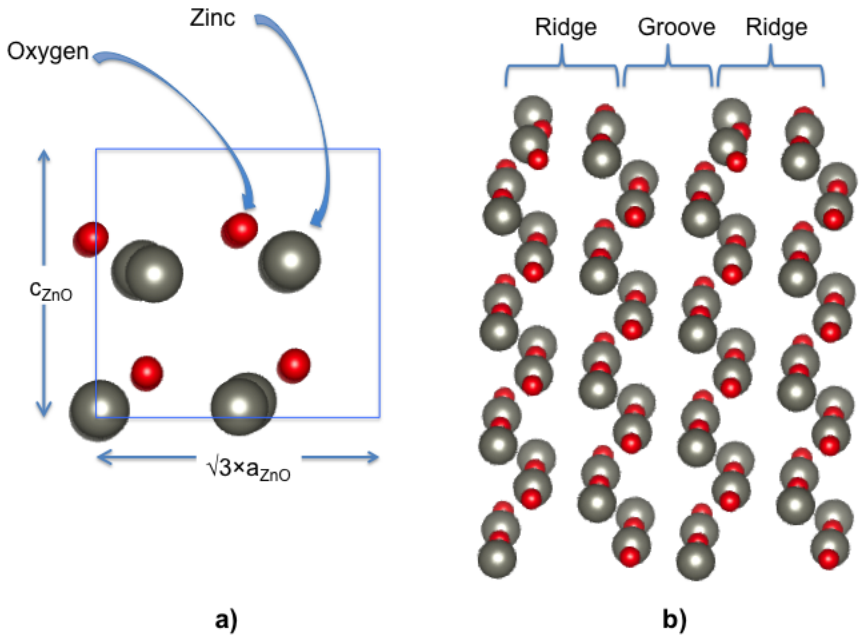

Figure 6-2: a) Unit cell ($x-y$ plane) for ZnO($11\bar{2}0$). b) 3D illustration of a 2×2 surface of ZnO($11\bar{2}0$) showing the groove and ridge alternating pattern at the surface.

vergence was assumed when the forces on the ions were less than 0.001 Ry/Bohr. For the slabs, eight atomic layers were modeled and the spacing between repeating slabs was 15Å. A dipole correction [74] was used to prevent artificial electrostatic interactions between the repeating units. Half of the 8 ZnO layers were relaxed in our calculations. The lattice constants in the x-y plane were fixed to c_{ZnO} and $\sqrt{3}\times a_{ZnO}$ respectively (see Fig. 6-2). We calculated surface electronic structure, and CO_2 and methanol adsorption properties.

6.2.1 Results

Surface electronic structure

Upon relaxing the ZnO($11\bar{2}0$) slab structure, we calculated the projected density of states (PDOS). Fig 6-3 shows the PDOS for the surface layer and the bulk-like layer in the center of the slab. Comparison of the PDOS in these layers shows that the loss of coordination and the appearance of a small dipole as evidenced by a surface

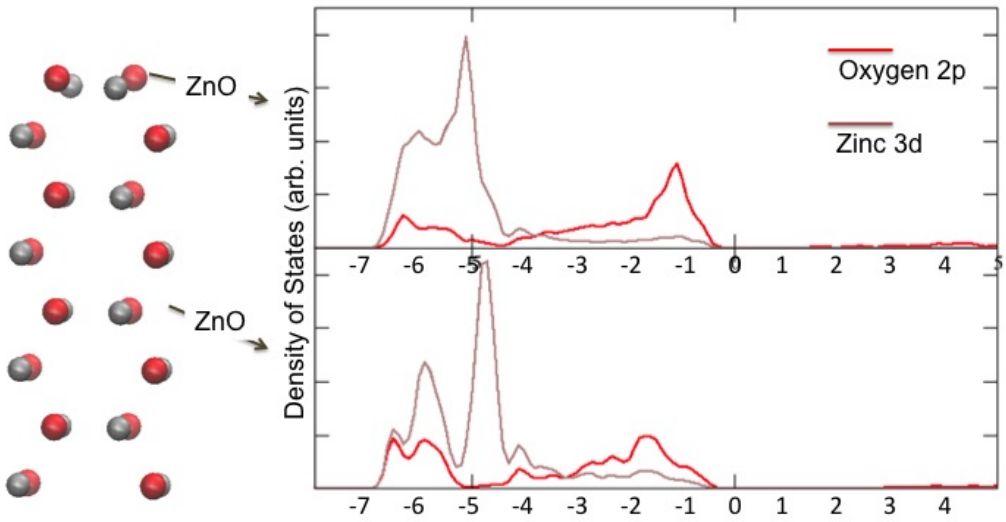

Figure 6-3: Projected density of states for ZnO($11\bar{2}0$) slab.

Zn-O displacement of $\delta_{Zn-O} = -0.23\mathring{A}$ perpendicular to the surface has little effect on the surface electronic structure. This conforms with STM and LEED studies [75, 76] which show an essentially bulk-like termination of the surface. Moreover, the slight dipole at the surface may explain the roughness reported in both papers. The dipole introduces an instability which can be compensated by adsorption of adatoms or a surface reconstruction as may be the case here (see Section 6.3.1). We measure the bond length at the surface compared to the bulk and find a 5% reduction, in agreement with Ref. [77] in which a 6% reduction was reported.

CO_2 adsorption properties

Next we calculate adsorption of CO_2 on the 1×1 surface (coverage of 1ML). We find that the molecule binds in a tridentate form, so that the carbon is surrounded by three oxygen atoms (Fig. 6-4), leading to a high binding energy of -1.15eV.

To analyse the mechanism for this process, we compare the O-atom projected

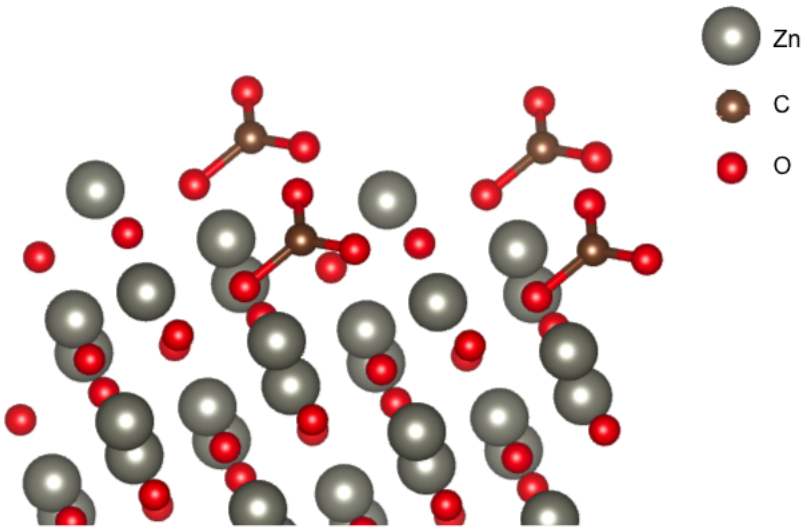

Figure 6-4: CO_2 adsorption on the ZnO($11\bar{2}0$) surface. The molecule binds across a groove in a tridentate manner.

densities of states of the ZnO surface before and after adsorption of CO_2 (Fig. 6-5). The plot shows a decrease in the pDOS for O-2p after binding, suggesting that the CO_2 in this adsorption process is an electron acceptor. The Zn-3d states remain essentially unchanged before and after adsorption. Computing the Lowdin charges for all the atoms before and after adsorption, we find a transfer of 0.65 electrons from the surface to the CO_2 molecule, confirming this picture.

We also performed CO_2 adsorption calculations for a lower adsorbate coverage of 1/2 ML using a $\sqrt{2} \times \sqrt{2}$ ZnO($11\bar{2}0$) surface supercell. We find that the adsorption energies unexpectedly decrease for this coverage. For most molecules, the adsorption energy tends to increase with decreasing coverage as molecule-molecule repulsions are reduced. If this is not the case, then either (1) the adsorption at the higher coverage involved some favorable contribution from the molecule-molecule interaction or (2) there is some re-relaxation of the surface such that the mechanism (such as charge transfer) which enhances the adsorption process is promoted. Since the direction interaction between the adjacent CO_2 molecules in the tridentate configuration is an

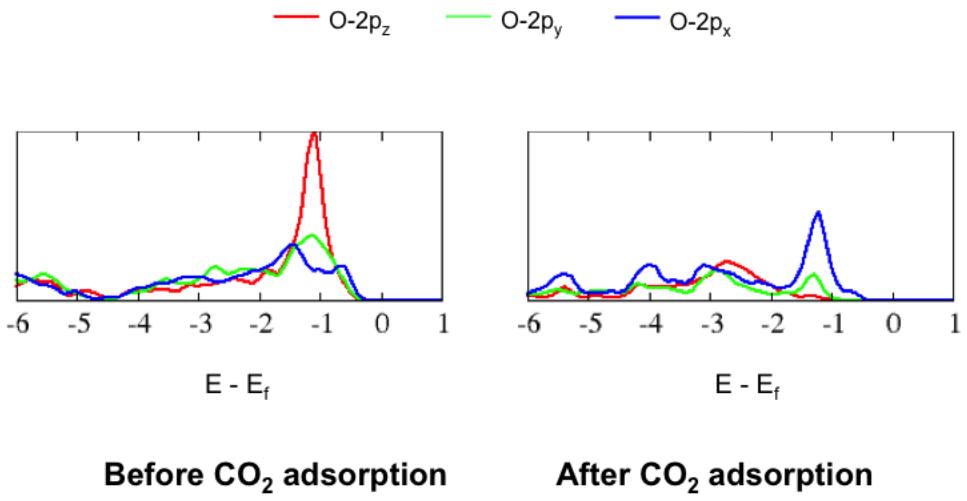

Figure 6-5: Projected densities of state on surface O atoms before and after CO_2 adsorption.

O-O repulsion (see Fig. 6-4), we expect the latter mechanism to be the case. The data are presented in Table 6.1.

Methanol adsorption properties

Due to the size of the methanol molecule, it is necessary to choose several different starting positions of its adsorption of on ZnO in our calculations. The minimum energy configuration is shown in Fig. 6-6 where the only atom directly binding to the surface is the hydrogen of the hydroxyl group. The binding energy was found to be -1.53eV. We also calculated the binding energy on a $\sqrt{2} \times \sqrt{2}$ ZnO$(11\bar{2}0)$ surface as shown in Table 6.1. We find that the binding energy decreases with decreasing coverage as with CO_2.

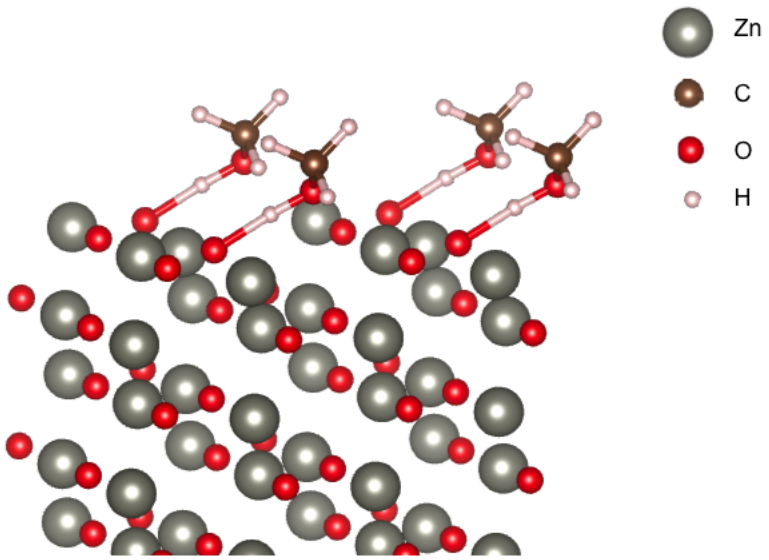

centering

Figure 6-6: Methanol adsorption on the ZnO($11\bar{2}0$) surface.

Cell size	Coverage (ML)	Molecule	Adsorption Energy (eV)
1×1	1	CO_2	-1.148
$\sqrt{2} \times \sqrt{2}$	1/2	CO_2	-0.812
1×1	1	CH_3OH	-1.525
$\sqrt{2} \times \sqrt{2}$	1/2	CH_3OH	-0.424

Table 6.1: CO_2 and methanol adsorption energies at different coverages for the ZnO($11\bar{2}0$) surface.

6.3 *ab-initio* calculations for ZnO(0001)

6.3.1 Theory of polar surfaces

ZnO grown in the vertical c-direction will either be O-terminated or Zn-terminated. Both of these configurations are polar. As shown in figure 6-1, the zinc and oxygen atoms are stacked in the form of double layers. If we consider that the atoms are perfectly ionic and carry their formal charges, the charge at each layer will be as shown in the figure where x is the sum of charges on each atomic layer. The dipole moment would be $m = Nxe(c/2 - uc)$, corresponding to a polarization $P_s = xe(1 - 2u)$ which in turn has an internally induced electric field associated with it. This means the polar surface has to be unstable [78] and our calculations should model an infinite number of layers to obtain the actual surface properties [77]. Contrary to this, experiments show that the surface of finite ZnO slabs are stable and undergo little reconstruction.

As discussed by Tasker [78], Meyer [77] and Woll [79], there exist different mechanisms that may lead to the removal of this instability. One of these is a charge transfer between the two different polar surfaces without a significant rearrangement of the geometric positions. Another possibility is a reconstruction changing the geometry of the surface. The last possibility is the adsorption of charged particles. In experiments (e.g Ref. [80]), the O-terminated surface is found to be normally stable because of the presence of adsorbed hydrogen and the clean O-terminated and Zn-terminated surfaces undergo a 3×1 reconstruction. For simplicity, the presence of adatoms or reconstructions at the surface are not taken into account in our calculations at this stage.

6.3.2 Results

We carried out calculations using eight double layers of ZnO(0001) slab in the hexagonal wurtzite structure. We considered both the Zn- and O- terminated structures. These are usually labeled as ZnO(0001) and ZnO($000\bar{1}$) respectively in the literature, but for simplicity we will refer to them as Zn-terminated or O-terminated ZnO(0001)

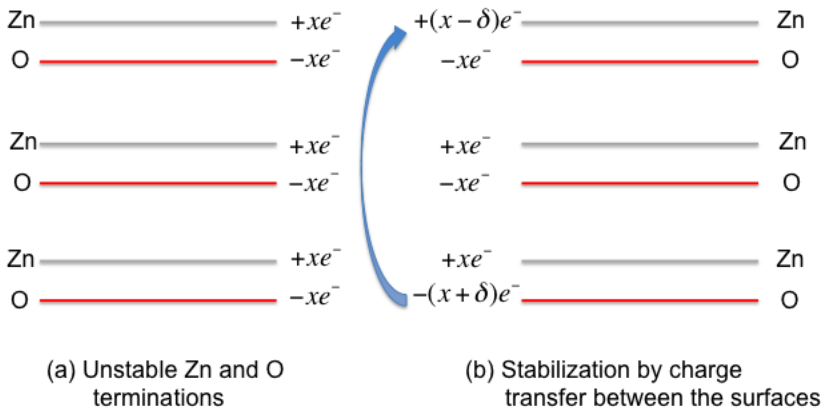

Figure 6-7: Illustration of the stabilization effect of charge transfer between the Zn- and O-terminated surfaces.

slab. We relaxed the topmost four ZnO stacks in each structure and fixed the rest to the bulk value (see Figure 6-8). We then examined the relaxation of the surface and its CO_2 and methanol adsorption properties.

Surface structure

Upon relaxation, it is seen that both the O- and Zn-terminated surfaces change significantly from the bulk structure. We tabulate the differences between the Zn and O planes in each ZnO double layer in Table 6.2; these displacements are indicative of the dipole in each layer. For the O-terminated surface, the oxygen and zinc planes move towards each other by approximately the same distance, amounting to a compression of the double layer distance by 45.5% at the surface. This is in excellent agreement with results of x-ray diffraction studies of the surface (such as Ref. [81] which reports a surface dipole compression of 45%).

The Zn-terminated surface shows a similar compression pattern except that the surface Zn-atoms remain in their bulk-like positions and the compression is due almost

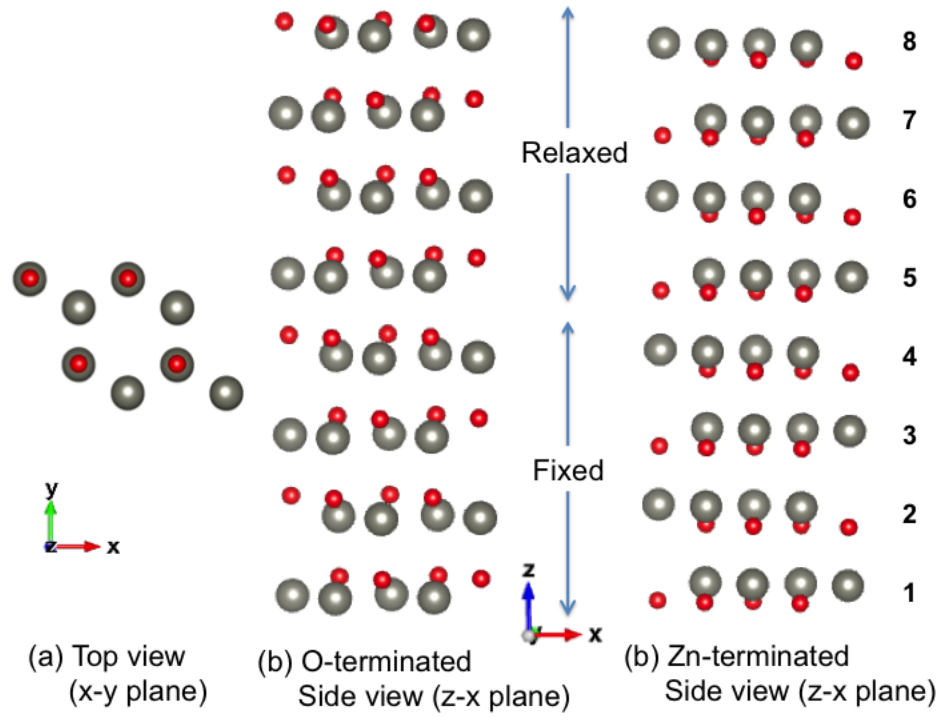

Figure 6-8: Configuration of the slab calculations for the 0001 O- and Zn- terminated slabs. Fig a) shows the plan view and b) and c) show side views of the O- and Zn-terminated slabs respectively.

entirely to the upward relaxation of O-plane by 0.17Å. The compression in this case is therefore much less than for the O-terminated case (see Table 6.2). The compression value of 26.2% is not in agreement with experiment reported in Ref. [82] which determined that the Zn-terminated surface is almost exactly bulk-like and no dipole relaxation takes place at the surface. Even the outward relaxation of the oxygen atoms in the surface double layer by as little as 0.1 cannot be fitted to the experimental data. Our results however correlate with results from other theoretical studies which predict a compression between 24% and 31%. [83, 81, 84, 77] This discrepancy between theory and experiment may be due to surface reconstruction or passivation which were not taken into account in the theoretical calculations. An investigation of this discrepancy is however beyond the scope of this thesis.

Next we studied the electronic structure of the two surfaces. As shown in figure 6-7, instead of a removal or repositioning of the zinc or oxygen ions to stabilize the surfaces, it is possible that there is a transfer of charge between the Zn- and O-

Layer	Dipole $\lvert\delta_{\mathrm{Zn-O}}\rvert$ (Å)	
	O-terminated	Zn-terminated
8	0.345	0.468
7	0.545	0.564
6	0.593	0.580
5	0.600	0.591
4	0.634	0.634
3	0.634	0.634
2	0.634	0.634
1	0.634	0.634

Table 6.2: Dipole ($\lvert\delta_{\mathrm{Zn-O}}\rvert$) in each layer of ZnO(0001). Recall that layers 5-8 are relaxed and 1-4 are fixed to the bulk configuration.

terminated surfaces of the slab. Such a charge transfer would lead to the build up of an electric field which opposes the electric field intrinsic to the polar surface and thus stabilizes the slab. A transfer of electrons from the O-terminated ZnO face to the Zn-terminated face will manifest in the formation of partially filled surface bands, a situation which is quite common for polar semiconductor surfaces [83]. Asalso lead to a consequence of the presence of partially filled surface states on the O-terminated surface, this surface would be metallic [79]. This can be seen in figure 6-9 where new states appear in both O-2p and Zn-3d orbitals around the Fermi level with comparatively more states on the O-terminated surface in agreement with the results in Ref. [84]. In Figure 6-10 for the Zn-terminated surface, we see that some electronic states close to the Fermi level are lost. Therefore data from Figs. 6-9 and 6-10 support the idea that ZnO(0001) thin slabs are stabilized by a charge transfer process from the Zn-terminated surface to the O-terminated surface. As expected, there is a slight metallicity at the Zn-terminated surface (figure 6-10).

CO_2 adsorption

We consider CO_2 adsorption on the 2×2 Zn- and O- terminated ZnO(0001) surfaces. Our results show that the O-terminated surface binds CO_2 much less strongly compared to the Zn-terminated case. This is puzzling as the O-termination provides many oxygen sites for the carbon center of the CO_2 to bind as was the case for the

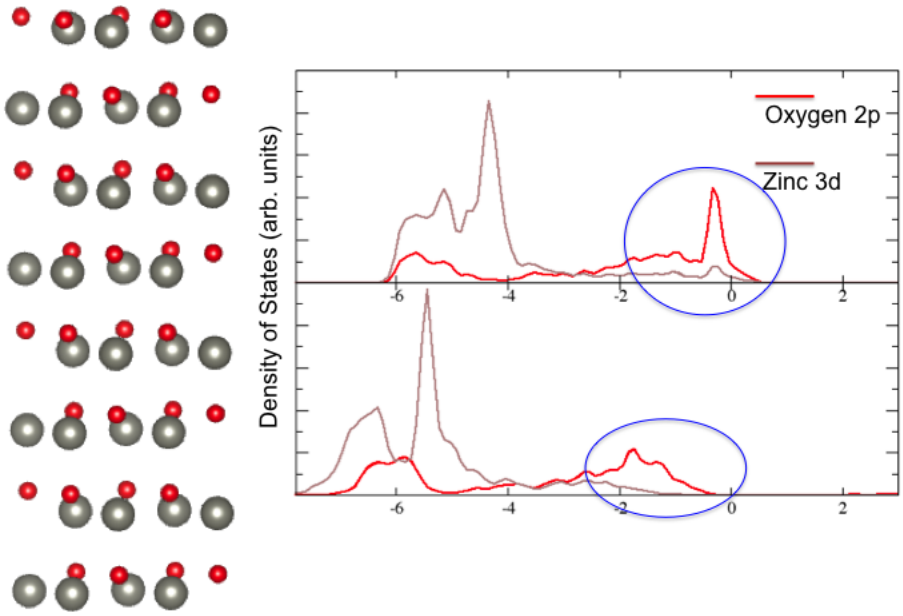

Figure 6-9: Density of states for the relaxed O-terminated ZnO layer and an almost bulk-like fixed layer. It is seen that new (metallic) O and Zn states appear at the surface close to the Fermi level.

$(11\bar{2}0)$ surface. We however recall that the tridentate configuration of CO_2 requires the oxygen atoms in the molecule to bind to the surface as well. In the case of the O-terminated surface, there are no Zn-atoms to bind to and O-O bonds are difficult to form. Therefore the net result is a lack of appreciable binding to the surface (see Figure 6-11). In the case of the Zn-terminated surface, some binding between the the carbon center and a Zn atom is possible and the two O-atoms are strongly attracted to nearby Zn atoms (see Figure 6-12). Therefore the CO_2 binding energy on this surface is comparatively large.

On the polar (0001) surfaces, we find that CO_2 is an electron acceptor during binding as we found for the ZnO$(11\bar{2}0)$ surface. For the O-terminated surface, the molecule accepts only $0.03e^-$ and has a binding energy of -0.23eV. This is in contrast to the binding on the Zn-terminated surface where the molecule accepts $1.05e^-$ and has a binding energy of -1.10eV, more than four times that on the O-terminated surface.

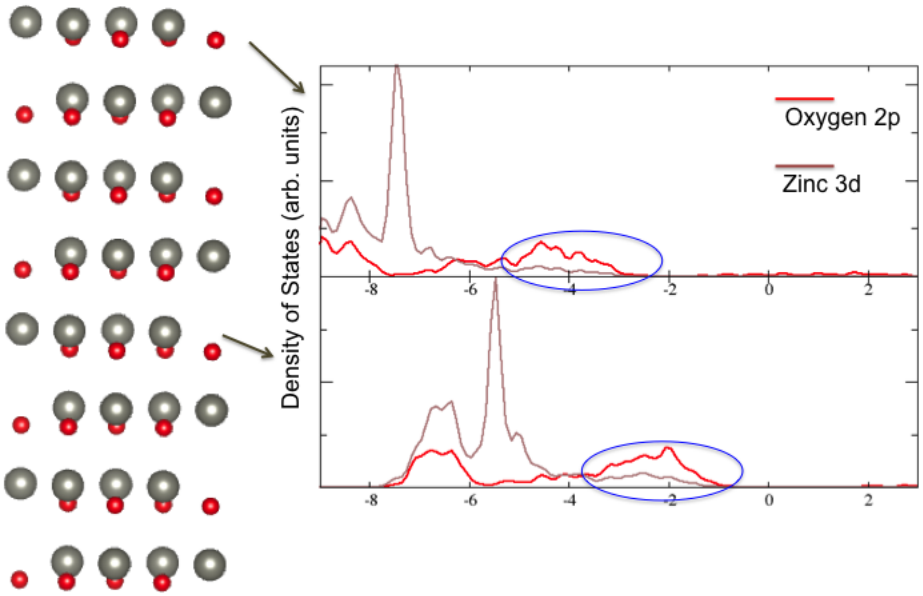

Figure 6-10: Density of states for the relaxed Zn-terminated ZnO(0001) surface layer and an almost bulk-like fixed layer. We see that peaks in the O- and Zn- states close to the Fermi level are lost on the surface.

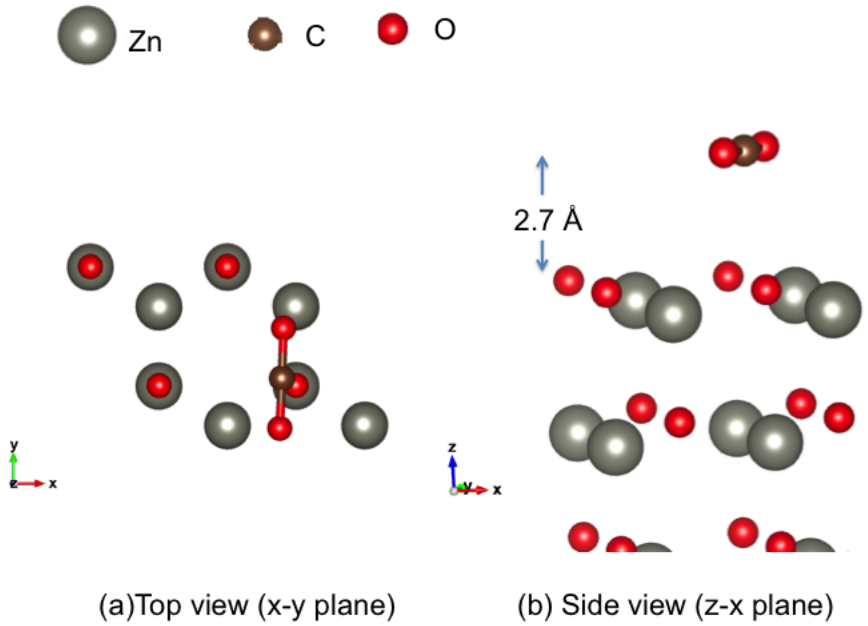

Figure 6-11: Binding configuration of CO_2 on O-terminated ZnO(0001). The binding energy is -0.23eV.

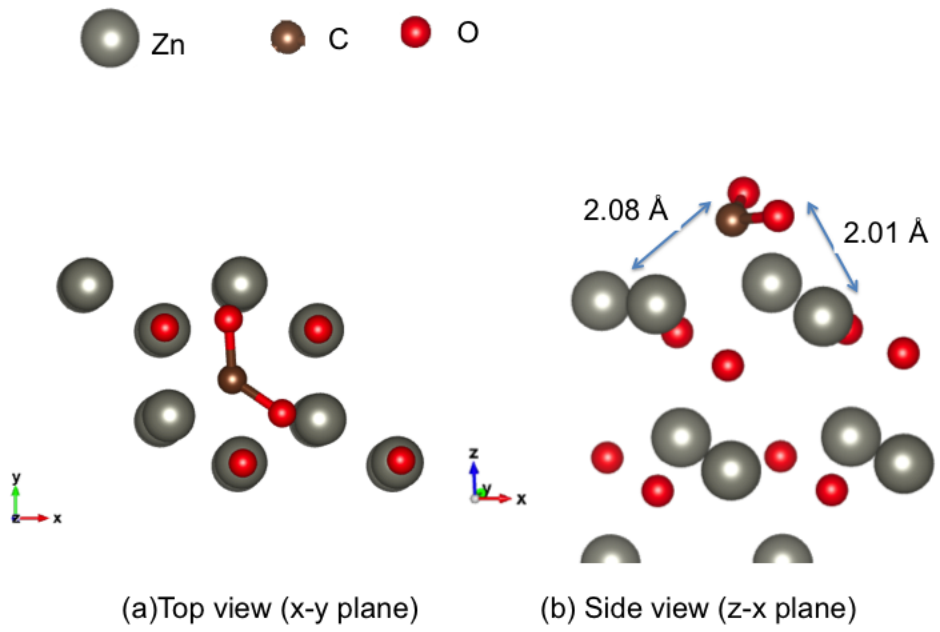

Figure 6-12: Binding configuration of CO_2 on Zn-terminated ZnO(0001). The binding energy is -1.10eV. The distance of each oxygen atom in the CO_2 to the nearest Zn atom is 2.01A, compared to the Zn-O distance in the ZnO bulk of 1.96A. This suggests a very strong CO_2-Zn bond.

Cell size	Coverage (ML)	Termination	Adsorption Energy (eV)
2×2	1/4	O	-0.233
$\sqrt{13} \times \sqrt{13}$	1/13	O	-0.255
2×2	1/4	Zn	-1.098
$\sqrt{13} \times \sqrt{13}$	1/13	Zn	-1.984

Table 6.3: CO_2 adsorption energies at different coverages for the O- and Zn- terminated ZnO(0001) surfaces.

We also performed CO_2 adsorption calculations using the larger $\sqrt{13} \times \sqrt{13}$ ZnO(0001) surfaces. The adsorption energies increased as expected, but most significantly for the Zn-terminated surface. The data are presented in Table 6.3.

Methanol adsorption

Methanol adsorption follows the trend for CO_2 adsorption. In this case, we used only the $\sqrt{13} \times \sqrt{13}$ ZnO(0001) surfaces. This is because we will be comparing the results here to that of $\sqrt{13} \times \sqrt{13}$ ZnO(0001)/$PbTiO_3$ in Chapter 8. We find that the adsorption energy on the O-terminated surface (-0.622eV) is about half that on the Zn-terminated surface (-1.154eV). For the O-terminated case, only the hydrogen atoms bind directly to the surface (see Fig. 6-13. In contrast, the Zn atoms at the surface in the Zn-terminated case provide bonding sites for the oxygen atom in methanol. The differences in bonding energy and configuration on slabs of the same cut and material could be important for applications in tunable catalysts.

6.4 Conclusion

We have investigated the properties of the non-polar ZnO($11\bar{2}0$) and the polar ZnO(0001) surfaces. We find that the surface of non-polar ZnO develops a slight dipole that may explain the surface roughness found in experiments. During CO_2 adsorption, the surface transfers a charge of $0.65e^-$ to the molecule . We also find methanol to be an electron acceptor that binds relatively strongly to the surface.

We also investigated the properties of the ZnO(0001) surfaces, demonstrating that the stabilizing mechanism for the ZnO(0001) slab polarization is charge transfer

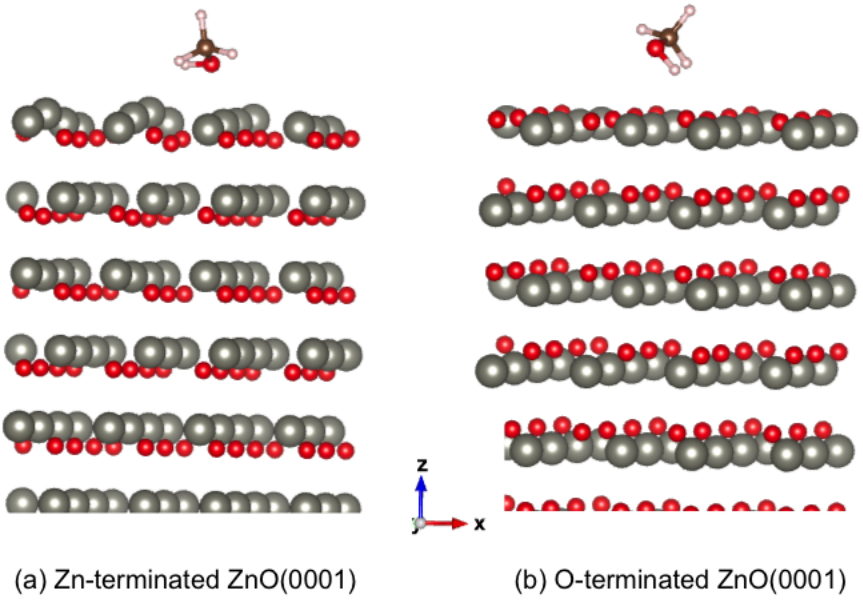

Figure 6-13: Binding configuration of methanol on (a) Zn-terminated and (b) on O-terminated ZnO(0001).

between the two surfaces (O-terminated and Zn-terminated). We show that CO_2 binds four times as strongly on the Zn-terminated surface as on the O-terminated surface due to the difficulty in forming bonds between O atoms in CO_2 and the O atoms on the ZnO(0001) surface in the O-terminated case. A similar trend was also found for methanol adsorption. As expected, we find that the adsorption energy for both $CO_2$and CH_3OH on these surfaces increases at lower coverages.

In the next two chapters, we will consider how the polarization of an underlying substrate affects the surface properties of ZnO($11\bar{2}0$) and ZnO(0001).

Chapter 7

Effect of polarization switching on the surface chemistry of $ZnO(11\bar{2}0)_n/PbTiO_3$

7.1 Introduction

Various studies have shown that the polarization of a substrate can affect the properties of supported metal films [85], including influencing reaction rates in catalysis [29]. Kolpak and Grinberg demonstrated the dynamical control of surface structure and reactivity in the coupling of ferroelectric $PbTiO_3$ with Pt [37]. They performed DFT computations of the adsorption of several molecules and atoms to the surface of ultrathin Pt(100) films supported on ferroelectric $PbTiO_3$ and showed that switching the polarization direction of the substrate dramatically changes the chemisorption strength and site preferences of CO, O, C, and N and alter the reaction pathways for dissociation of CO, O_2, N_2 and NO. Rather than using Pt, we use non-polar $ZnO(11\bar{2}0)$ and focus on CO_2 fixation processes. Since ZnO is a wide band-gap insulator, the mechanism for any substrate-polarization-induced changes is expected to be different compared to that of metal Pt layers. In addition, it is interesting to investigate CO_2 conversion processes on ZnO (which is used in the catalytic conversion

of CO_2) when the ZnO surface is made dynamically tunable.

In this chapter we calculate the surface, interface and adsorption properties of 1, 2, 3 and 4 layers of ZnO grown on polarized $PbTiO_3$. We will notationally write these as $ZnO(11\bar{2}0)_n/PbTiO_3\uparrow$ and $ZnO(11\bar{2}0)_n/PbTiO_3\downarrow$ for the up (positively) polarized and down (negatively) polarized $PbTiO_3$ respectively, where n is the number of $ZnO(11\bar{2}0)$ layers. In all our calculations, we use the PbO-terminated symmetric $PbTiO_3$ slab which has been demonstrated to be the slab termination that exists under realistic thermodynamic constraints. [2]

7.2 Method

We performed DFT computations using the plane-wave pseudopotential code PWscf [64]. A PbO-terminated centered 2×2 cell having 9 alternating PbO and TiO_2 layers stacked in the 001 direction was used for the $PbTiO_3$ substrate. All except the last two top layers were fixed to the bulk-like atomic positions in order to simulate a thick $PbTiO_3$ slab. We used 1-4 layers of ZnO oriented in the $11\bar{2}0$ direction. All the ZnO layers were relaxed along with the PbO and TiO_2 layers (see Figure). A k-point mesh of $4 \times 4 \times 1$ was selected. A spacing of $20\overset{o}{A}$ between periodic images of the superstructure in the z-direction was used. A dipole correction [74] was applied in the center of the vacuum region to cancel out any artificial field between the repeating layers. The in-plane lattice constant was fixed to $\sqrt{2}$ times the lattice constant of bulk $PbTiO_3$ (which was calculated to be $3.88\overset{o}{A}$). The relaxation calculations were set to complete when the forces on the relaxed layers were less than 1×10^{-3}a.u. For each ZnO film thickness, calculations were performed for positively and negatively poled $PbTiO_3$ substrates.

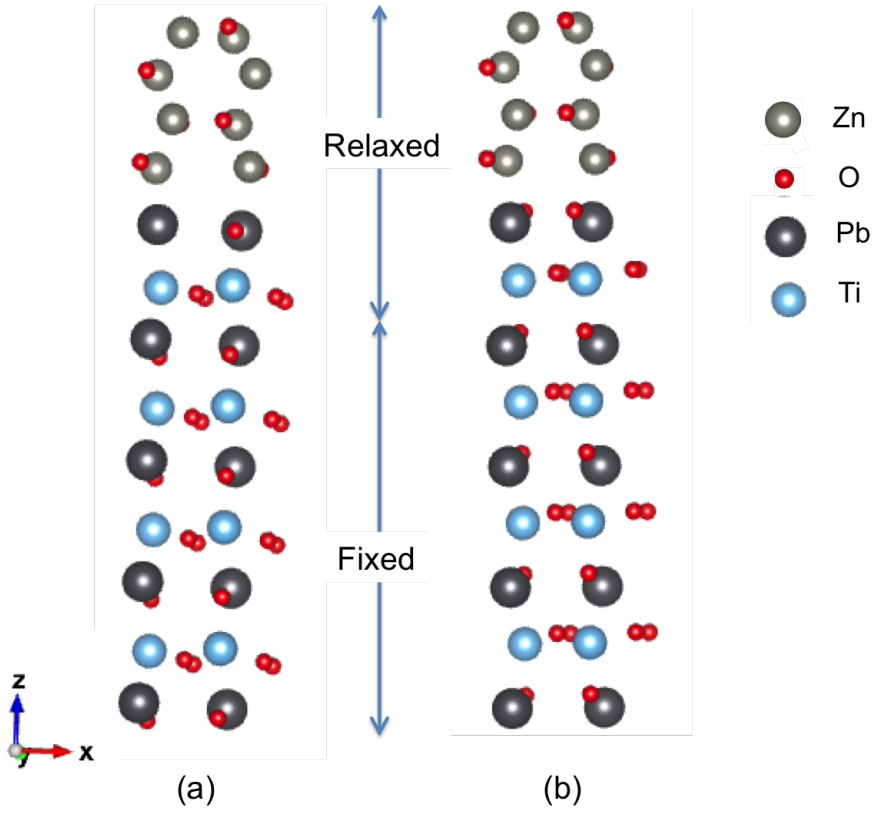

Figure 7-1: Unit cells for $ZnO(11\bar{2}0)_n/PbTiO_3$ slab for $n = 4$, (a)Up polarized and (b) Down polarized.

7.3 Results and discussion

7.3.1 Surface and interface properties

We first investigate the stability of the ZnO-$PbTiO_3$ interface. We calculated the interface formation energy using

$$E_{f,int} = E^{slab}_{PbTiO_3+ZnO} - E^{slab}_{PbTiO_3} - nE^{bulk}_{ZnO} - \sum_i n_i^{int}\mu_i(T, p_i) \tag{7.1}$$

where $E_{f,int}$ is the interface formation energy, $E^{slab}_{PbTiO_3+ZnO}$ is the energy of the complete ZnO + perovskite slab, $E^{slab}_{PbTiO_3}$ is the energy of the perovskite slab by itself, and nE^{bulk}_{ZnO} is the energy of ZnO bulk formed by the number of ZnO pairs in the ZnO layers (see Figure 7-2). The last term adds the effect of the chemical potential of the species μ_i and the interface structure (through the number of atoms of species i making up the interface, n_i^{int}). Since we are examining a perfect interface and assuming constant thermodynamic conditions for all slabs, we can compare the relative stabilities by ignoring the last term, or equivalently writing a relative interface formation energy as

$$E^{rel}_{f,int} = E_{f,int} + \sum_i n_i^{int}\mu_i(T, p_i) = E^{slab}_{PbTiO_3+ZnO} - E^{slab}_{PbTiO_3} - nE^{bulk}_{ZnO} \tag{7.2}$$

We will perform a full thermodynamic analysis for this system in a later work.

The results at different polarizations and number of layers for the *relative* interface formation energies are shown in Fig 7-3. As the figure shows, the interface with the negatively polarized substrate is more stable by ~0.5eV than that with the positively polarized substrate, suggesting that during experiments, it may be better to start the ZnO epitaxy at this polarization and switch it later if necessary when the required number of layers has been grown. However this assumes that the surface stoichiometry of the perovksite is the same for both polarizations. As Fig. 7-4 shows, n_O^{int} and n_{Pb}^{int} at the interface may not be the same at different polarizations even if μ_O and μ_{Pb} are

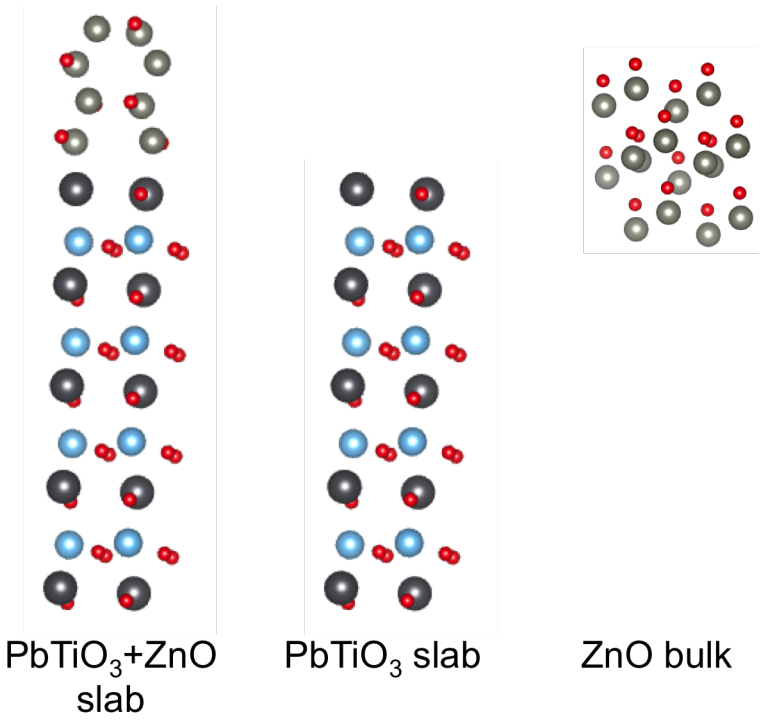

Figure 7-2: Calculating the interface formation energies.

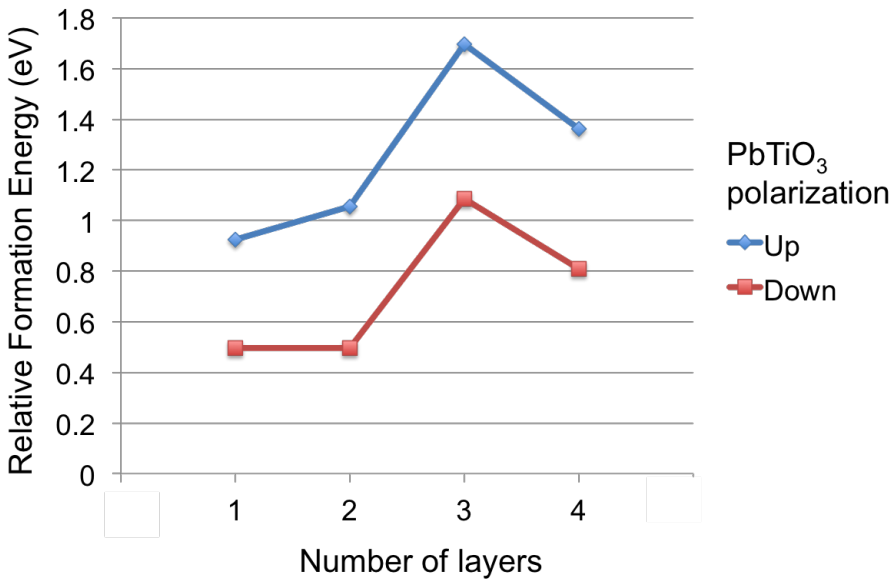

Figure 7-3: Relative interface formation energies of n-layers of ZnO on PbO-terminated $PbTiO_3$ at different polarizations. The formation energies are calculated using 7.2.

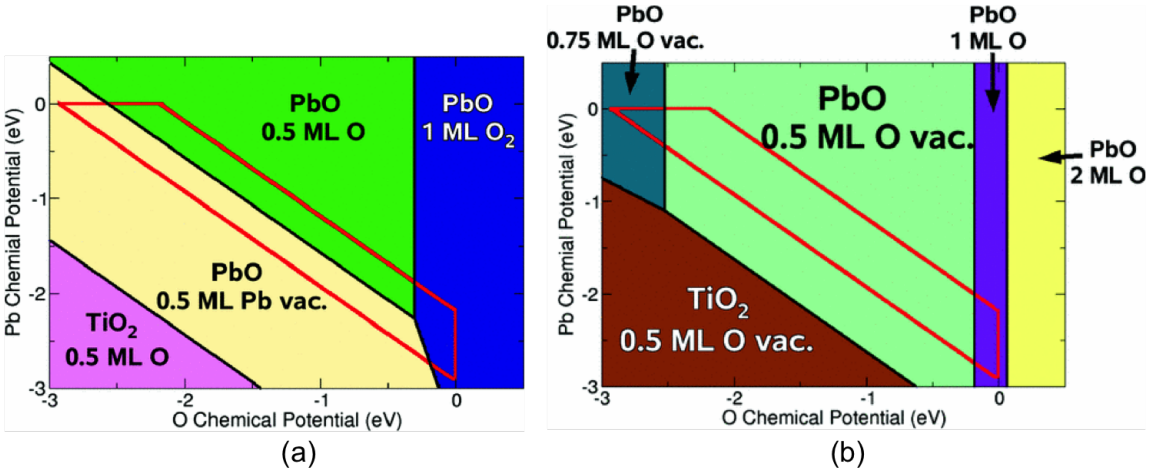

Figure 7-4: Phase diagram of (a) positively poled surface (b) negatively poled surface as a function of μ_O and μ_{Pb}. Each colored region is the thermodynamically stable structure for those chemical potentials. The physically allowed region is inside the red lines. Stable structures are all PbO terminated. Reprinted with permission from Ref. [2]. Copyright (2013) by the American Physical Society.

the same. Also, the number of ZnO layers grown may affect the interface structure for the ZnO layers (therefore affecting μ_{Zn} and n_{Zn}^{int}). Therefore the last term in Equation 7.1 may be different. An accurate analysis requires an investigation of all interface vacancy possibilities, which is beyond the scope of this thesis. We would however still expect the down-polarized interface to be the more stable. Since the oxygen atoms in the topmost PbO layer are closer to the lowest ZnO layer in the down-polarized case compared to the up-polarized case, the Zn atoms at the interface can more readily find O atoms to partially satisfy the coordination requirements and lower the surface (now interface) energy of the ZnO slab.

Our original hypothesis was that the polarization of the perovskite would affect the surface chemistry of the ZnO. To investigate this, we computed the projected densities of state for the atoms at the surfaces. From Fig. 7-5 it is clear that there is a distinct effect of the perovskite polarization on the electronic density of states on the ZnO($11\bar{2}0$) surface. In addition, we find the number of layers has some effect especially when the polarization is in the z-direction (up). In general, there is a downwards shift in energy for the valence band edge in the positively polarized structure, and an upward shift in the valence band edge energy for the negatively polarized structure.

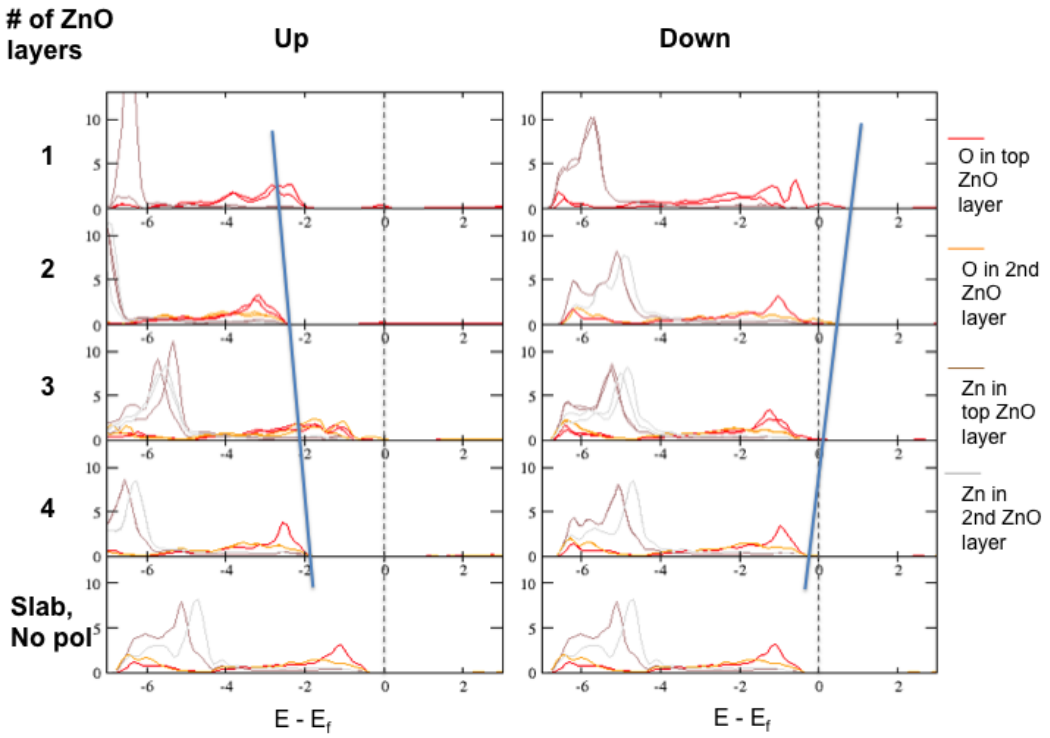

Figure 7-5: Projected DOS on O and Zn atoms in the first two surface layers of $ZnO(11\bar{2}0)_n/PbTiO_3$for n =1, 2, 3 and 4 and both polarization directions in the $PbTiO_3$. The plots at the bottom, "Slab, no pol" are for the first two layers of $ZnO(11\bar{2}0)$ as described in Section 6.2. The slant lines are the show the approximate shift in the valence band edges due to polarization effects.

It is instructive to further investigate how the perovskite polarization in combination with a specific number of ZnO layers produces different surface chemistries. We turn our attention to exploring how the electron density in the ZnO layers change with the introduction of the $PbTiO_3$. The density redistribution plots in Fig. 7-6 are obtained by subtracting the electronic density of the $ZnO(11\bar{2}0)_n$ and $PbTiO_3$ from that of $ZnO(11\bar{2}0)_n/PbTiO_3$, i.e

$$\rho_R(\mathbf{r}) = [\rho_o(\mathbf{r})]_{\mathrm{ZnO(1120)_n/PbTiO_3}} - [\rho_o(\mathbf{r})]_{\mathrm{ZnO(1120)_n}} - [\rho_o(\mathbf{r})]_{\mathrm{PbTiO_3}} \tag{7.3}$$

where $\rho_o(\mathbf{r})$ is the ground state charge density obtained from self-consistent DFT calculations. Obviously, the sum of the charge redistribution over real space will equal zero.

$$\sum_{\mathbf{r}} d\mathbf{r}^3 \rho_R(\mathbf{r}) = 0 \tag{7.4}$$

We can see from the charge redistribution plots of Fig. 7-6 that:

- the charge redistributions at the ZnO surface are mostly around the oxygen atoms. For the up-polarized structure, we see an increased electronic density in the p_z orbitals at the expense of a $p_{x,y}$-like orbital. The reverse is the case for the down-polarized structure.

- the spatial densities of the charge redistributions roughly decreases away from the ZnO-$PbTiO_3$interface. This correlates with reduced polarization effects away from the interface.

Therefore we conclude that the effect of the perovskite is to draw electrons from (or push electrons to) the $ZnO(11\bar{2}0)_n$ sub-structure. The effectiveness of this redistribution at the surface however depends how far it is from the interface.

We also calculated the dipoles at the surfaces of the ZnO and compared to that of the $ZnO(11\bar{2}0)$ slab. Figure 7-7 shows the results. We find the greatest fluctuations are for the up-polarized structure, consistent with the pDOS plots of Figure 7-5. For each polarization direction, the observed pattern can be explained as a competition

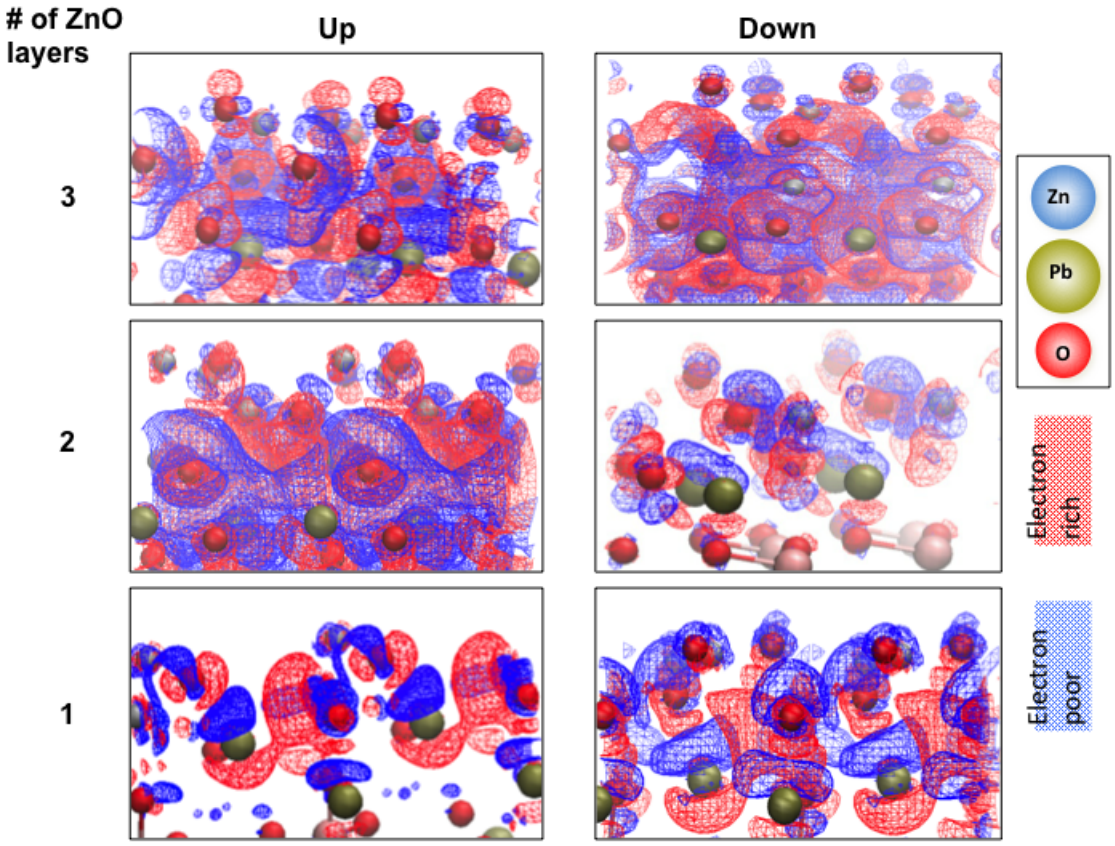

Figure 7-6: Charge redistribution plots for $ZnO(11\bar{2}0)_n/PbTiO_3$for n =1, 2, 3.

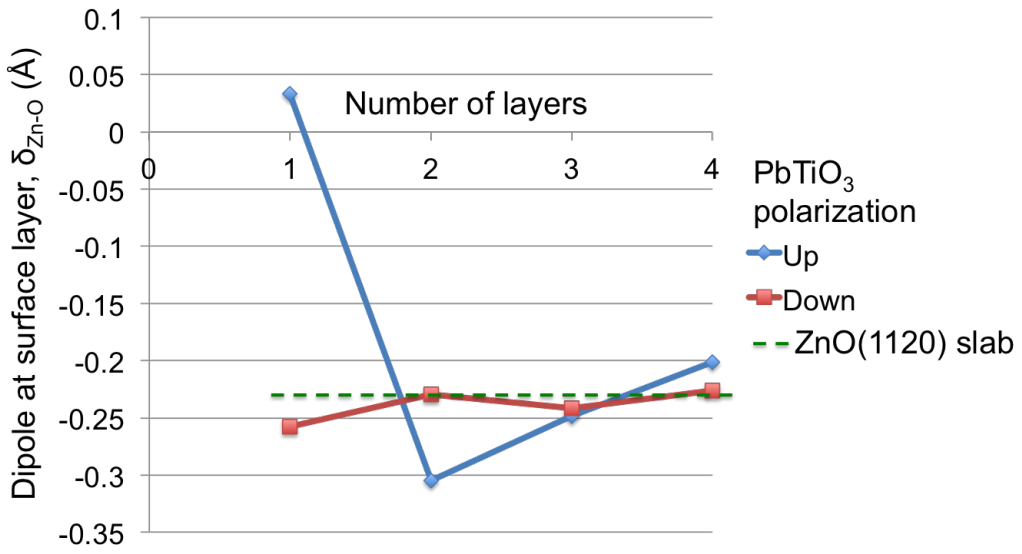

Figure 7-7: Dipoles at the surfaces of $ZnO(11\bar{2}0)_n/PbTiO_3$ where n is the number of ZnO layers.

between the effect of the number of layers and polarization. This phenomenon will be further explored in the next section when discussing CO_2 adsorption properties, which reflects these trends.

7.3.2 Adsorption properties

CO_2 adsorption

To examine CO_2 adsorption on the surfaces of $ZnO(11\bar{2}0)_n/PbTiO_3$. We first determined the most favorable adsorption configuration on the catalyst (see Fig. 7-8). We find that configuration (a) is the most stable configuration. We then ran different calculations for the adsorption energies of CO_2 on $ZnO(11\bar{2}0)_n/PbTiO_3$ and plain ZnO slabs. Our results are shown in Fig. 7-9, which shows that there was a difference in adsorption energies of $\sim 0.8eV$ between the different polarizations of the perovskite at $n = 1$, 2 and 3. The difference tapers off after four layers of ZnO. We estimate therefore that the polarization effects will be negligible for $ZnO(11\bar{2}0)_n/PbTiO_3$ layer for $n \geq 4$. We compare this with earlier calculations of CO adsorption on $Pt(001)_n/PbTiO_3$ [37] where the difference in adsorption energies on the Pt surface at $n = 1$ was $\sim 0.6eV$ and essentially decreases to zero for $n > 1$.

Figure 7-8: Starting configurations for relaxation calculations of CO_2 on the ZnO surface.

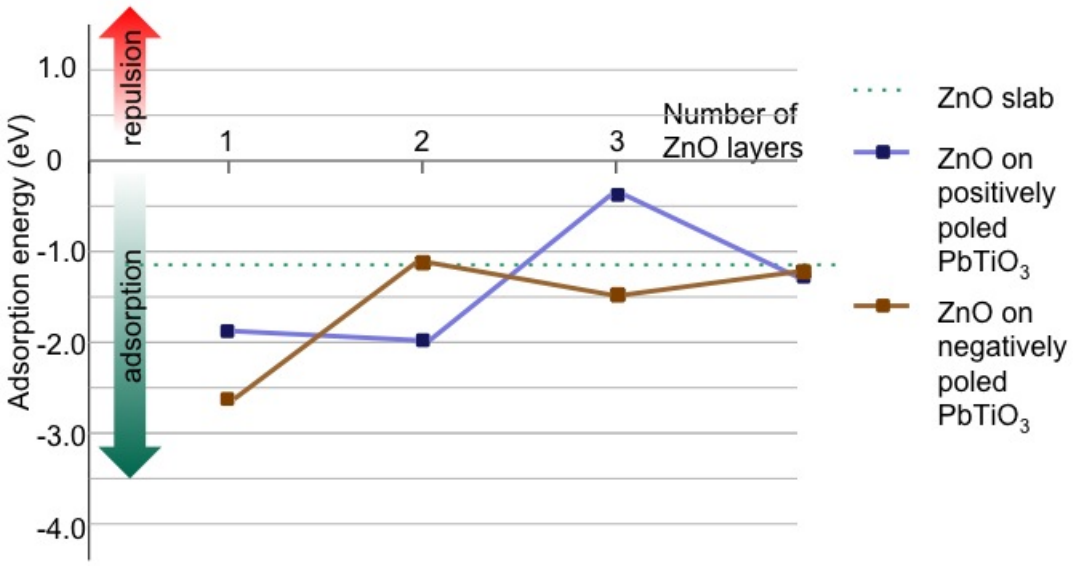

Figure 7-9: Adsorption energies of CO_2 on $ZnO(11\bar{2}0)_n/PbTiO_3$ at n=1, 2, 3 and 4 and different $PbTiO_3$ polarizations.

Another interesting aspect of the results in Fig. 7-9 is the change in the polarization direction that gives the best CO_2 affinity as each additional ZnO layer is added. For example, at n =1, CO_2 binds more strongly to the negatively poled surface, while it binds more strongly to the positively poled surface at n =2, and so on. This is strikingly similar to the results for the dipoles at the surfaces of the slabs as shown in Figure 7-7. We therefore expect that the surface dipole is a good descriptor in CO_2 adsorption and we developed a simple mechanistic model to explain this correlation (see Fig. 7-10). On a positively poled surface, the O atoms in the first bonded ZnO layer are strongly bound to Pb and are electron-satisfied and so will not be reactive with the carbon in the CO_2 molecule. In the second layer, the O atoms are farther away from the surface and so are only weakly bound to the PbO surface termination. They are therefore electron deficient and will readily take part in reactions. After two layers, we expect that the the epitaxial interface polarization does not have a direct effect on the chemical properties of the layer, but rather this responsibility is taken over by induced atomic polarizations on atoms in the previous layer. This assertion is supported by the charge redistribution plots of Fig. 7-6 which show little activity around the third and fourth layers (little redistribution of charges there due to the presence of the polarized surface). On a negatively poled interface (Fig. 7-10(b)), the reverse behavior occurs.

To investigate the CO_2 adsorption trend further, we calculated the densities of states projected on the oxygen orbitals in the ZnO surface before and after CO_2 adsorption. We find that the adsorption properties of the surfaces could be related to the electronic density of the oxygen p_z orbital relative to the p_x orbital and the spread of the projected density of states in the p_z orbital around the Fermi level. This is illustrated in Fig 7-11.

Figure 7-12 compares the projected densities of states for all the surfaces before and after CO_2 adsorption. In Fig. 7-12(a), the peak of the projected O-p_z orbital is below that of the O-p_x orbital for n =3 on the positively polarized structure. According to the description in Fig. 7-11, the CO_2 adsorption in this case should be poor. We find this to be true, with $E_{ads} = -0.361eV$ and the projected densities of

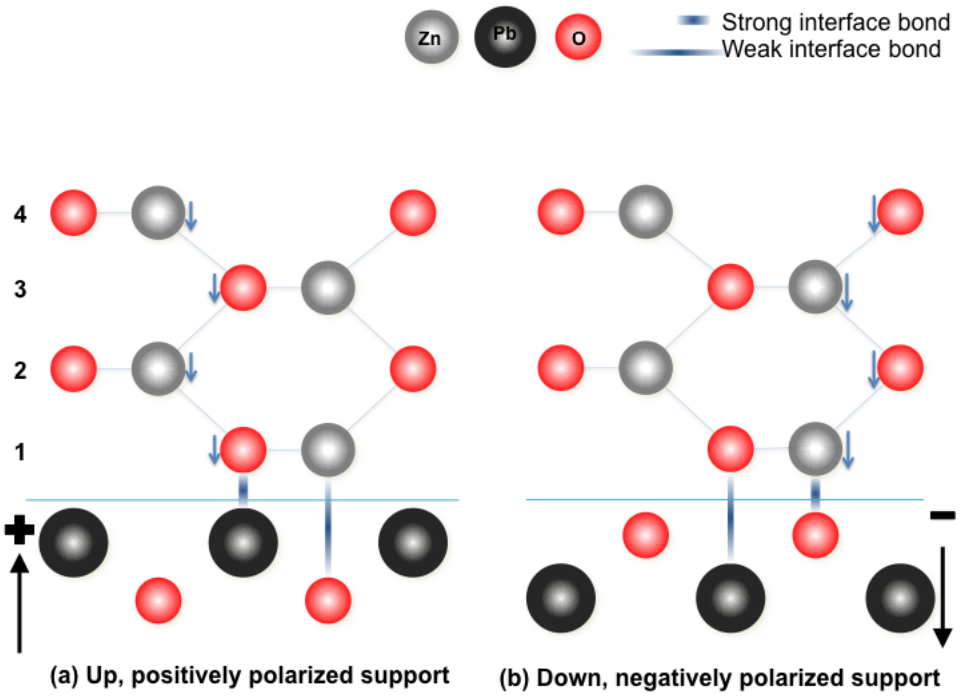

Figure 7-10: A simple mechanistic model for CO_2 affinity on $ZnO(11\bar{2}0)_n/PbTiO_3$for n =1, 2, 3. Thin and thick lines represent relatively weak and strong bonds respectively. CO_2 affinity is assumed to be related to the occupancy of the O-orbitals. The happier the oxygen atoms are, the less likely they will bond with (transfer electrons to) the carbon atoms.

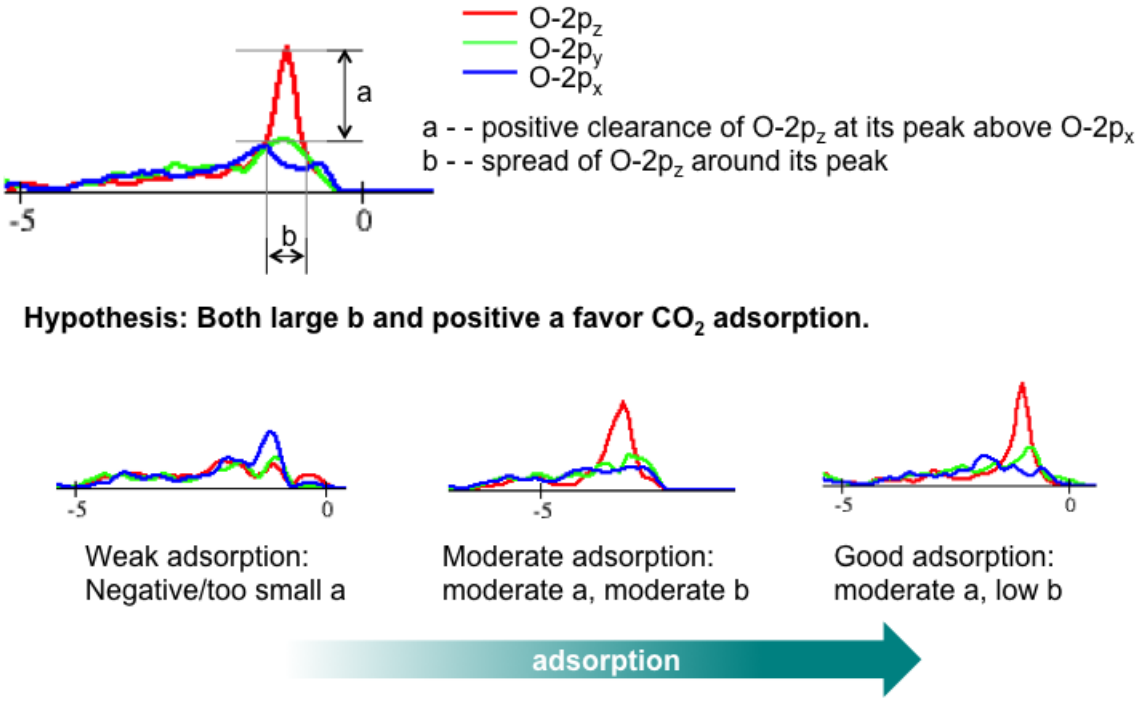

Figure 7-11: Descriptor for CO_2 affinity on $ZnO(11\bar{2}0)_n/PbTiO_3$ surfaces.

states before and after adsorption remain the same. For the remaining structures in Fig. 7-12(a), the peak of the projected O-p_z orbital is above the O-p_x orbital and so our model would predict strong adsorption. We find this to be the case. We also observe that the greater the width of the O-p_z orbital projected DOS about its peak, the stronger the adsorption. Consider for example that $E_{ads} = -1.979eV$ for $n = 2$ on the positively polarized structure. This adsorption energy is greater than those of, for example, $n = 2$ and 3 on the negatively polarized structures in which the O-p_z orbital band width is smaller.

A similar reasoning may be applied to the plots in Fig. 7-12(b) except for the case where $n = 1$ on down-polarized structure. The extremely high adsorption energy which appears not to involve the oxygen atoms at the surface may be attributed to an interference of the more strongly interacting PbO layer . This effect is not seen in the up-polarized case because it reacts much more weakly with CO_2. [2]

Methanol adsorption

Methanol adsorption properties on the surfaces of interest would of course be important to know when considering CO_2 conversion to methanol. As above, we calculated the adsorption energies using:

$$E_{ads} = E_{ZnO(1120)_n/PbTiO3+CH_3OH} - E_{ZnO(1120)_n/PbTiO3} - E_{CH_3OH} \tag{7.5}$$

The results are shown in Fig. 7-13. We see a great difference ($\sim 2.6eV$) in adsorption energies between the two polarization orientations for n =1. As seen in Fig. 7-14, methanol adsorbs on the positively polarized structure mainly through a hydrogen atom with the C-O axis vertical. In contrast, the C-O axis is horizontal and the bonding is through two hydrogen and the oxygen atom when adsorption is on the negatively polarized structure. The difference in adsorption energies for methanol between the positively and negatively polarized structures however tapers off quickly to $\sim 0.2eV$ for n =2, 3 and 4. The smaller differences compared to CO_2 adsorption on the surfaces might be due to the greater degree of freedom the larger methanol

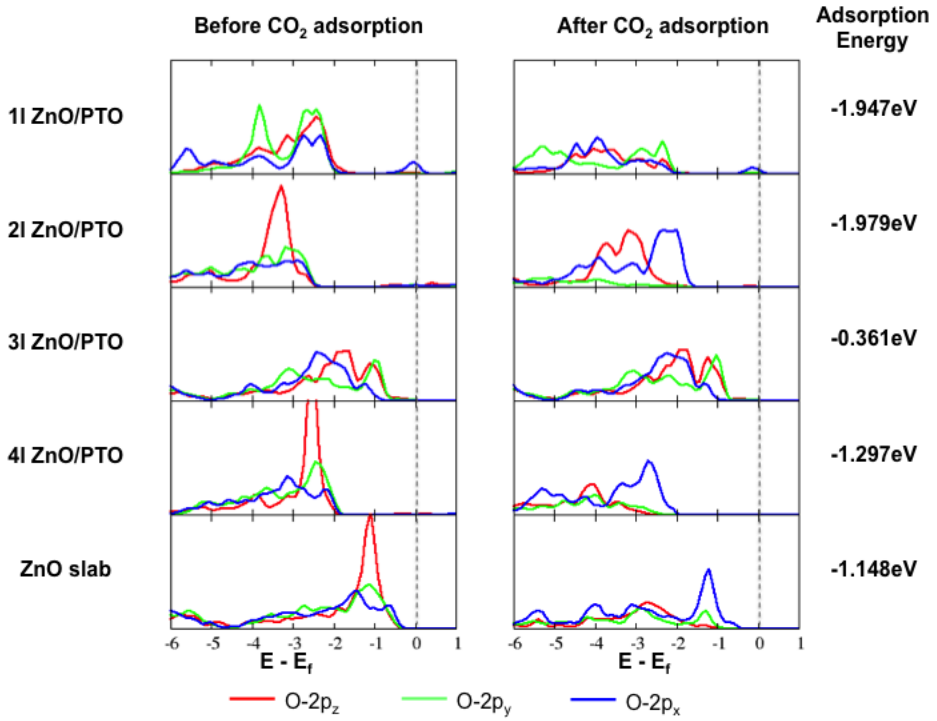

(a) Comparison of projected DOS on surface oxygen atoms before and after CO_2 adsorption on $ZnO(11\bar{2}0)_n/PbTiO_3$ for n =2 and 3.

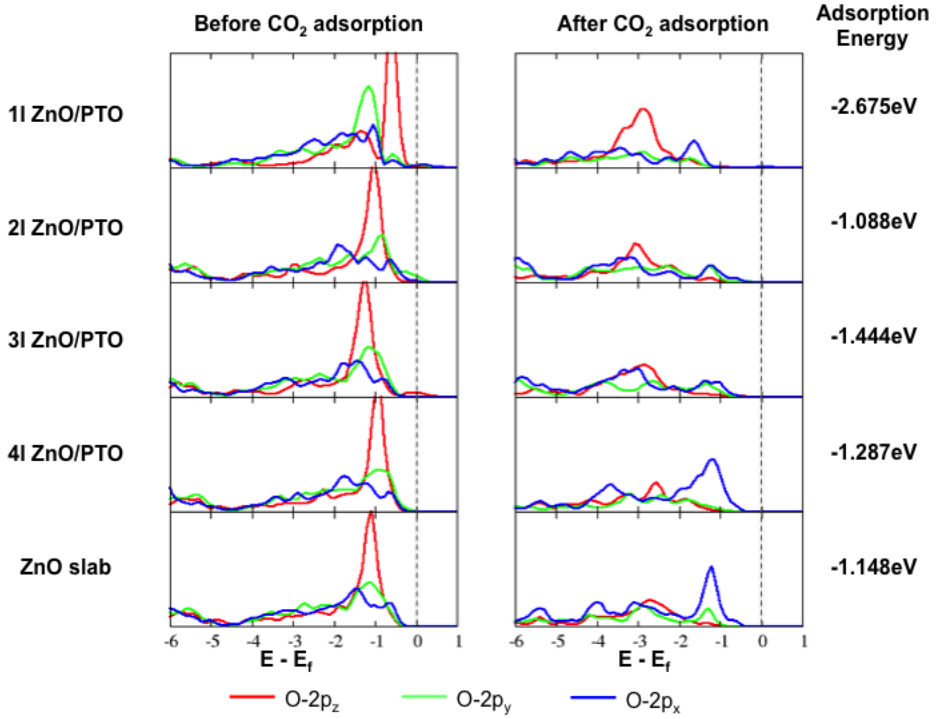

(b) Comparison of projected DOS on surface oxygen atoms before and after CO_2 adsorption on $ZnO(11\bar{2}0)_n/PbTiO_3$ for n =1 and 4.

Figure 7-12: Comparison of projected DOS on surface oxygen atoms before and after CO_2 adsorption on $ZnO(11\bar{2}0)_n/PbTiO_3$. Electrons in the O p_z orbitals are donated during CO_2 adsorption at all the surfaces.

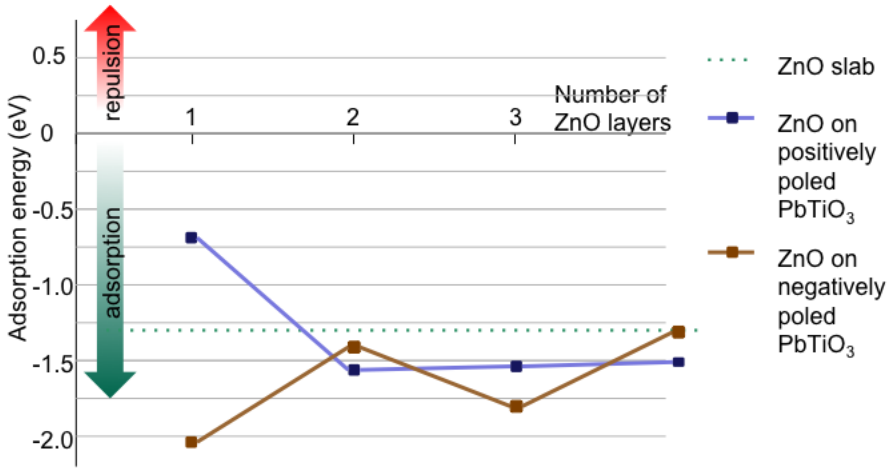

Figure 7-13: Adsorption energies for methanol on $ZnO(11\bar{2}0)_n/PbTiO_3$.

molecule has to find a more favorable ground state orientation on the surfaces.

7.4 Conclusion

We have seen that the surface chemistry of $ZnO(11\bar{2}0)_n/PbTiO_3$ is dependent on both the polarization direction of the $PbTiO_3$ substrate and the number of $ZnO(11\bar{2}0)$ layers n, with the effect of the substrate polarization becoming negligible for $n \geq 4$. Nonetheless, this is a much better performance than previous studies on tunable catalysts with metals [37], in which the effect essentially disappears for n > 1.

CO_2 and methanol adsorption calculations on $ZnO(11\bar{2}0)_n/PbTiO_3$ show that the polarization direction that gives the strongest adsorption energy changes as each additional ZnO layer is added. The mechanism for this process is hypothesized to be direct interaction of the first two ZnO layers and then secondary interactions of other layers with the PbO at the interface. The activation energy for thermal CO_2 dissociation into adsorbed CO and O was also found to be strongly polarization

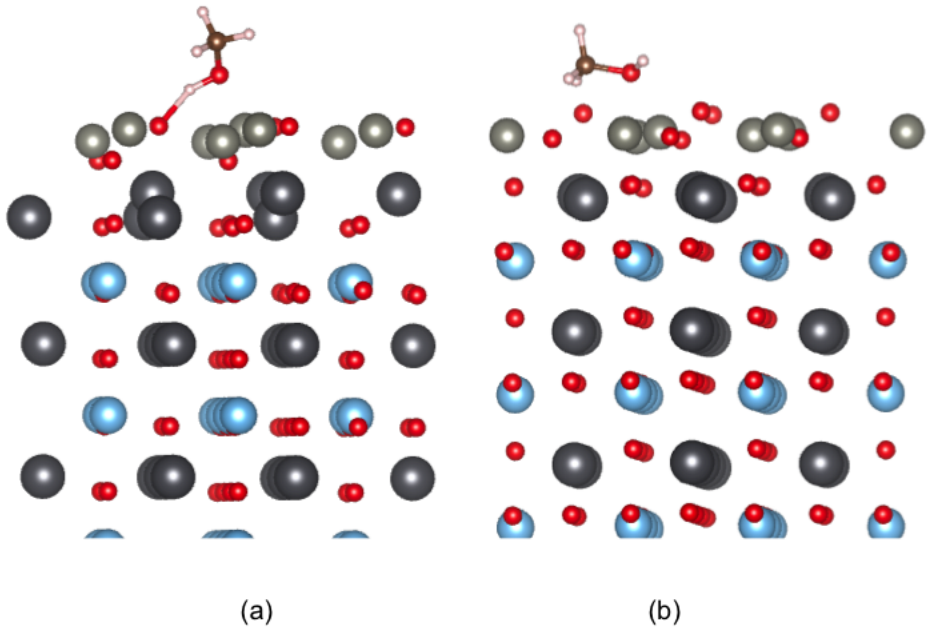

Figure 7-14: Configuration for methanol adsorption on $ZnO(11\bar{2}0)_n/PbTiO_3$for (a) positively polarized structure and (b) negatively polarized structure, for n=1.

dependent, with the positively poled substrates significantly decreasing the barrier relative to $ZnO(11\bar{2}0)$.

The large changes in CO_2 adsorption energy with polarization switching reported in this work are indicative of the possibility of controlling reaction energetics and pathways of CO_2 reactions. Indeed, our future work will focus on determining reaction energetics for CO_2 conversion to methanol and to cyclic carbonates using these catalysts.

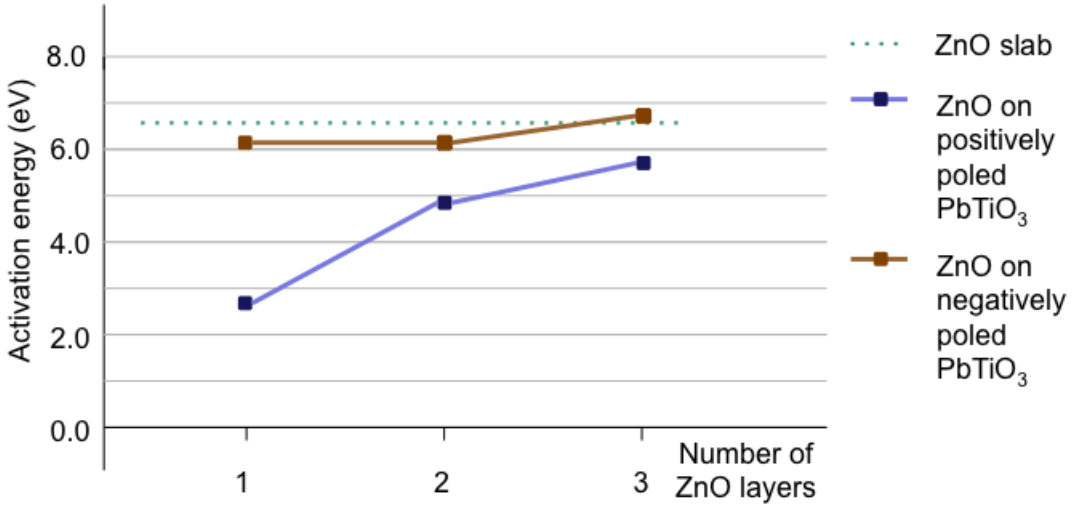

Figure 7-15: Activation energies for CO_2dissociation on $ZnO(11\bar{2}0)_n/PbTiO_3$for n =1, 2 and 3.

Chapter 8

Effect of polarization switching on the surface chemistry of $ZnO(0001)_n/PbTiO_3$

8.1 Introduction

As described in the previous chapter, polarization switching effects at the surface of $ZnO(11\bar{2}0)_n/PbTiO_3$ are negligible beyond four layers of ZnO grown on the perovskite. Although this is a substantial increase in the film thickness through which the substrate polarization effects can be observed when compared to metal/$PbTiO_3$ systems, it may still be difficult to control film growth to this level in large scale production of the catalyst. In this chapter, we therefore investigate another possible approach: polar ZnO(0001) films on PbTiO3(001).

Wei *et al.* [72] have experimentally shown the growth of both the non-polar $ZnO(11\bar{2}0)$ and polar ZnO(0001) on an ABO_3 perovskite (Fig. 8-1) depending on the growth conditions and method, in agreement with other papers. [86][87] Since the two possible terminations of polar ZnO(0001) have very different surface properties, [79] an ability to switch from one to the other would be a basis for an excellent tunable catalyst.

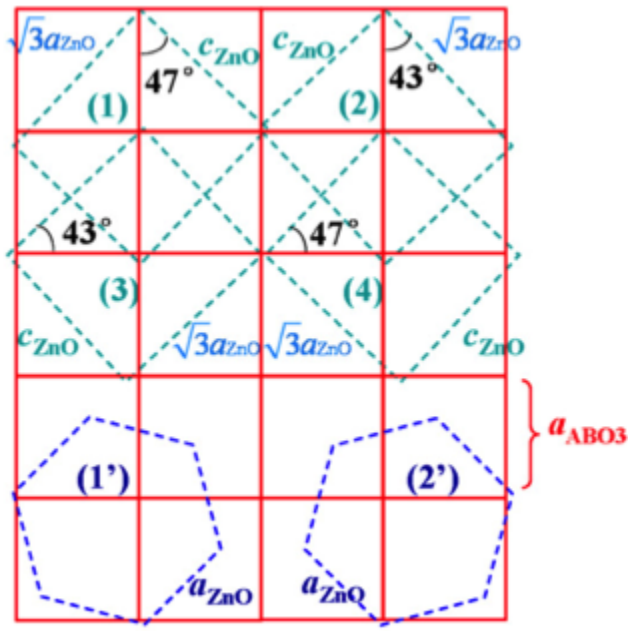

Figure 8-1: Schematic drawing of the epitaxial relationships of ZnO on $SrTiO_3$(001). Reproduced from Ref. [3].

Polar ZnO is known to not undergo any phase transitions at atmospheric pressures and its polarization cannot be switched with an electric field until its melting temperature of 2248K.[88] Previous attempts to induce ferroelectricity in ZnO at regular temperatures have included Li-doping (resulting in a ferroelectric transition at 330K at 6% Li concentration). [88, 89, 90] In these cases the smaller dopant atoms occupy off-center positions and form electric dipoles locally, thereby leading to ferroelectric behavior. Therefore the ferroelectricity comes from the dopants and does not utilize the intrinsic polarity of the ZnO material. The best remnant polarization obtained from these approaches was only $0.8\mu C/m^2$, about 33 times less than that of $BaTiO_3$ and 71 times less than that of $PbTiO_3$. In this chapter, we show that it is possible to attain a (potentially high T_c and remnant polarization) ZnO(0001) ferroelectric and we discuss the properties of the system as a tunable catalyst for CO_2 conversion.

Cell	a_{PbTiO_3}	θ_{PbTiO_3}	a_{ZnO}	θ_{ZnO}	$\%m_a$	$\%m_b$
ABCD	$\sqrt{2} \times \sqrt{2}$	90	$\sqrt{3} \times 2$	90	1.94	17.71
PQRS	2×2	90	$\sqrt{7} \times \sqrt{7}$	98.2	10.17	10.17
WXYZ	3×3	90	$\sqrt{13} \times \sqrt{13}$	87.8	0.095 (1.92)	0.095 (1.92)

Table 8.1: Selecting $x - y$ plane unit cell for ZnO epitaxy on $PbTiO_3$. See text for description.

8.2 Interface structure

The first step in modeling the $ZnO(0001)_n/PbTiO_3$ system for DFT plane wave computations is to figure out a reasonable unit cell for the matching of the hexagonal ZnO(0001) surface to the square $PbTiO_3$ surface. Possible options ABCD, PQRS and WXYZ requiring no more than a 4×4 $PbTiO_3$ surface substrate are shown in Fig. 8-2. The strains for each cell are tabulated in Table 8.1. The first column lists the cells (see Fig. 8-2), the second and fourth columns give the dimensions of the unit cell relative to the minimum planar unit cells of $PbTiO_3$ and ZnO respectively. The third and fifth columns give the angle of the rhombus formed by the planar cell of $PbTiO_3$ and ZnO respectively. The last two columns report the lattice mismatches between the second and fourth columns with respect to the second. For the last row, the values in bracket denote the total mismatch after the angular orientation of the lattice vectors are taken into account. We find that the most acceptable unit cell is WXYZ, a $\sqrt{13} \times \sqrt{13}$ cell of ZnO grown on 3×3 cell of $PbTiO_3$ (see Fig.8-3).

As before, we performed DFT computations using the plane-wave pseudopotential code PWscf [64]. A PbO-terminated centered 3×3 cell having 9 alternating PbO and TiO_2 layers stacked in the 001 direction was used for the $PbTiO_3$ substrate. All except the last two top layers were fixed to the bulk-like atomic positions in order to simulate a thick $PbTiO_3$ slab. We used 1-4 layers of ZnO oriented in the 0001 direction. All the ZnO layers were relaxed along with the PbO and TiO_2 layers. A k-point mesh of $1 \times 1 \times 1$ was selected. A spacing of 20Å between periodic images of the superstructure in the z-direction was used. A dipole correction [74] was applied in the center of the vacuum region to cancel out any artificial field between the repeating layers. The in-plane lattice constant was fixed to 3 times the lattice constant of bulk

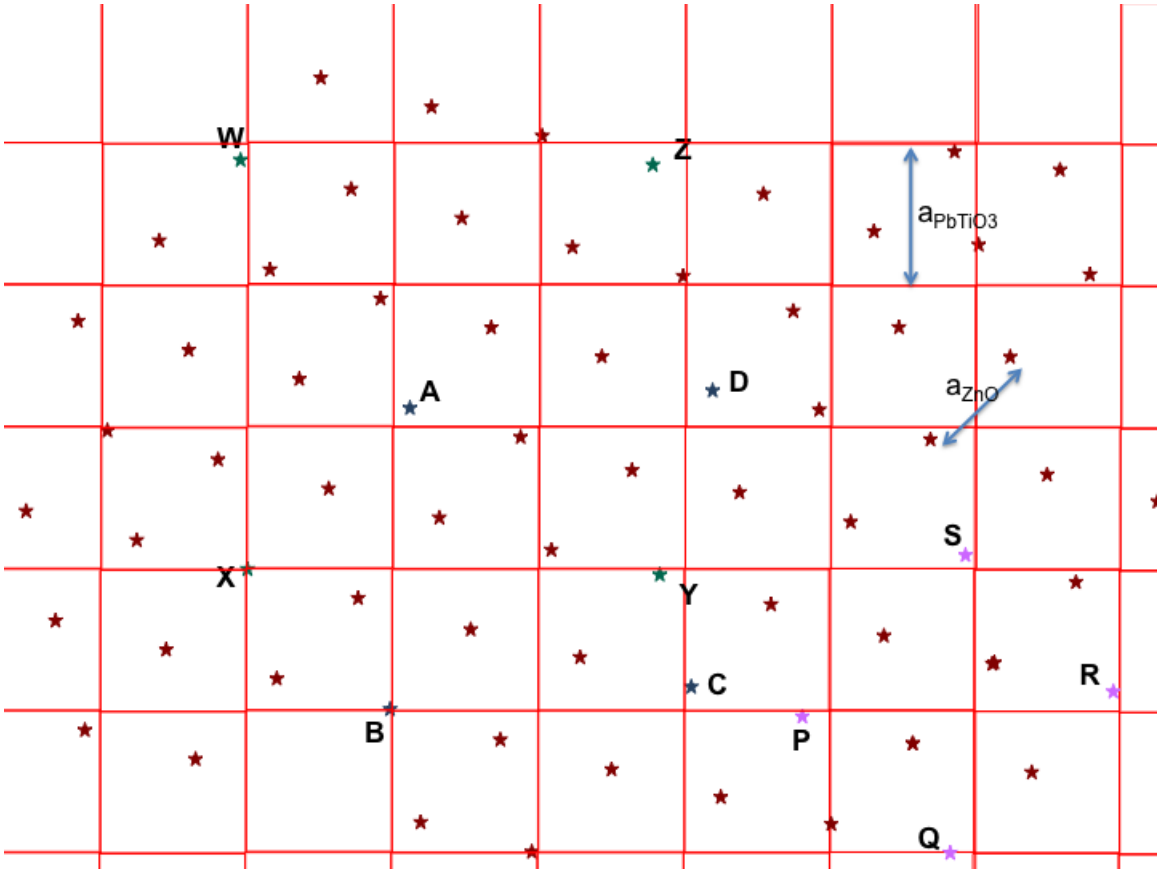

Figure 8-2: Epitaxial relationships of hexagonal ZnO(0001) (corner are the stars) on $PbTiO_3$(001) (edges are straight lines).

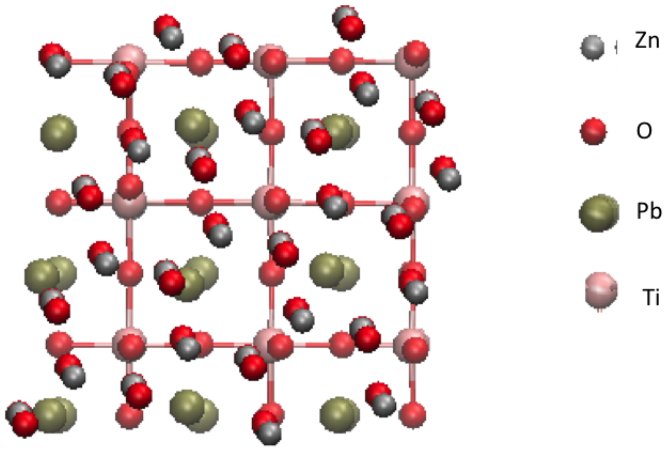

Figure 8-3: Unit cell WXYZ in the $x - y$ plane.

$PbTiO_3$ (which was calculated to be 3.87Å). The relaxation calculations were set to complete when the forces on the relaxed layers were less than 1×10^{-3}a.u. In total, we considered 16 systems: $ZnO(0001)_n$ positively and negatively polarized epitaxial layers 'grown' on $PbTiO_3$ positively and negatively polarized slabs for n =1, 2, 3 and 4.

8.3 Results

8.3.1 ZnO(0001) polarity switching

The starting positions for finding the ground states of $ZnO(0001)_n/PbTiO_3$ in our calculations were structured to determine whether thin ZnO(0001) films can be switched by the polarization of the underlying perovskite (Fig. 8-4). To each polarized $PbTiO_3$ slab, we added the two possible polarizations of ZnO(0001), leading to two starting configurations for each polarization direction.

The relaxed structures showed definite polarization switching (see corresponding configurations in Figs. 8-4 and 8-5). Figs. 8-6 and 8-7 show the magnitude of the difference between the average z-positions of the Zn and O atoms in each layer of ZnO for 1, 2, 3 and 4 layers at different starting configurations. These should be compared with Fig. 8-8 which shows the same data for free standing ZnO slabs.

While the polarization switching in ZnO may not be as complete if starting from different ZnO polarizations (see Figs. 8-4 and 8-5), we find that the perovskite polarization is sufficient to switch the polarization of the layers 50-80% of the way. Since in practice, the electric field that is used to switch the perovskite will probably help align the atoms in the right right direction, this number may become higher. Another observation from the plots is that the switching is most complete for n =3 (three layers of ZnO). We may attribute this to the right balance between remnant polarization in free-standing thin films of ZnO which increases with thickness (Fig. 8-8) and the propagation of perovskite-induced ferroelectricity in the ZnO which should decrease with thickness.

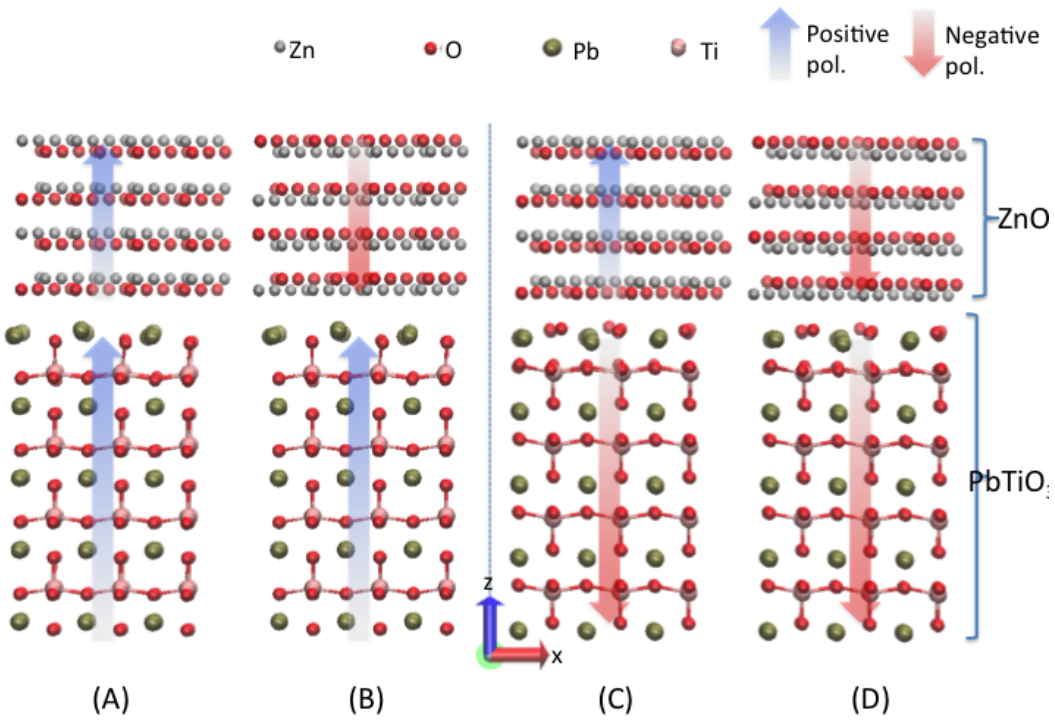

Figure 8-4: Starting configurations for $ZnO(0001)_n/PbTiO_3$ calculations for n=4.

While we understand the energy penalty for switching the perovskite layer (by varying the polarization and calculating the total energy in DFT), for practical applications, it would be necessary to also calculate the energy penalty for the additional switching of the ZnO polarization. Because some of atoms in the perovskite layers were fixed so as to simulate a thicker slab, the relaxed structures calculated are not the minimum energy ones and so NEB calculation results will be meaningless. We instead find an *approximate upper bound* for this value by calculating the energy in the ZnO layers as

$$E(ZnO)_{x\delta} = E(PbTiO_3 + ZnO)_{x\delta} - E(PbTiO_3)_{x\delta} \tag{8.1}$$

where δ is the matrix of total differences between corresponding atomic positions of any two end states, and $0 < x < 1$ is some fraction denoting how far the switching has progressed. Ideally, relax calculations for each x-configuration of $(PbTiO_3 +$

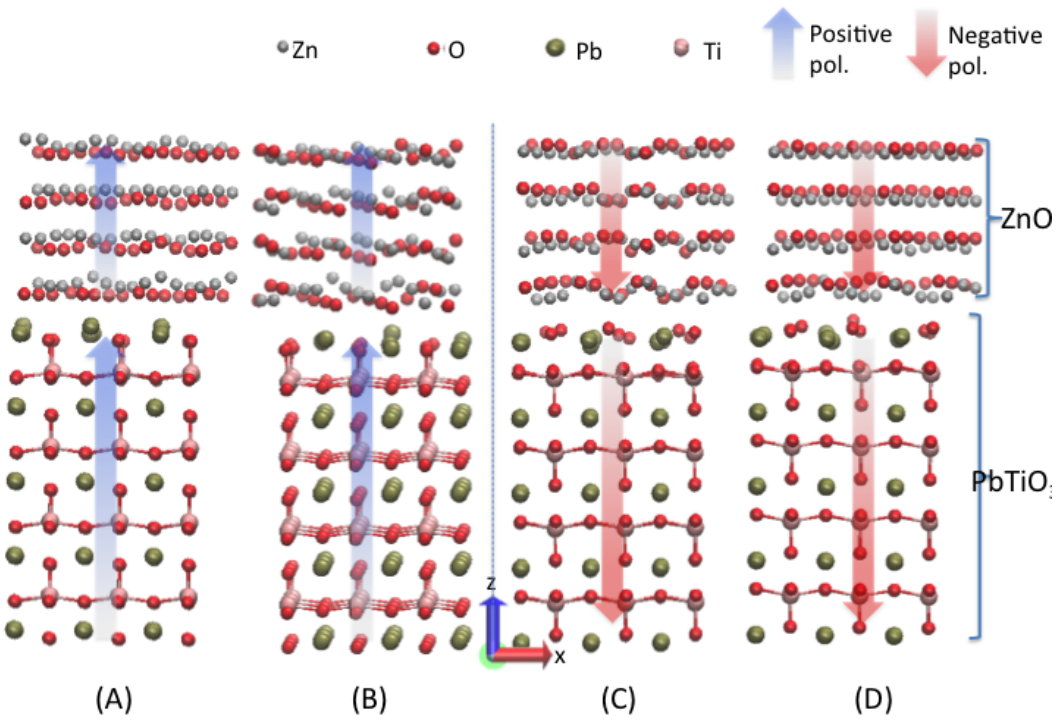

Figure 8-5: Relaxed configurations for $ZnO(0001)_n/PbTiO_3$ calculations for n=4.

$ZnO)_{x\delta}$ should be carried out first and then the atomic positions are used to calculate $E(PbTiO_3)_{x\delta}$. Since we merely want an upper bound, we carried out self-consistent-field calculations at the fixed x-configurations of $(E_{PbTiO_3+ZnO})_{x\delta}$. An example plot is shown in Fig. 8-9 which shows energies for transformations from relaxed configurations A to C and then to D and compares this to the energies in the ZnO layers had they not been stabilized.

8.3.2 Surface and interface properties

Next we analyze the surface properties. The projected densities of state for the top ZnO layer in each configuration and total number of ZnO layers is shown in Fig. 8-10. Due to the similarities in the electronic structures of the terminations for each polarization direction, we can infer that ZnO(0001) grown on positively (up) poled $PbTiO_3$ will display characteristics similar to that of a Zn-terminated ZnO(0001) slab. In contrast, ZnO(0001) grown on negatively (down) poled $PbTiO_3$ will display

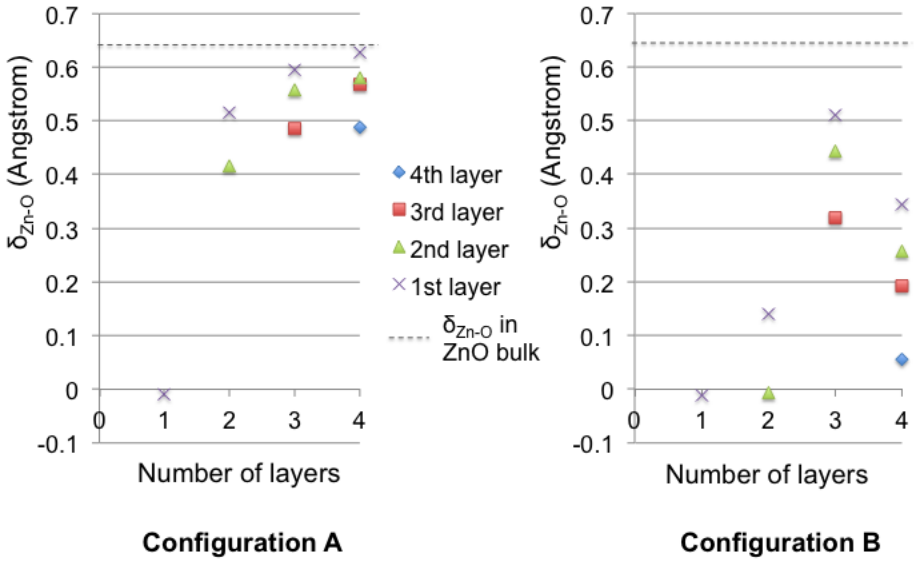

Figure 8-6: Average polarization vector δ_{Zn-O} in the ZnO layer(s) in $ZnO(0001)_n/PbTiO_3$ for n =1, 2, 3 and 4. Configurations A and B refer to starting polarization directions as in Fig 8-4(A) and (B) where the perovskite is positively polarized.

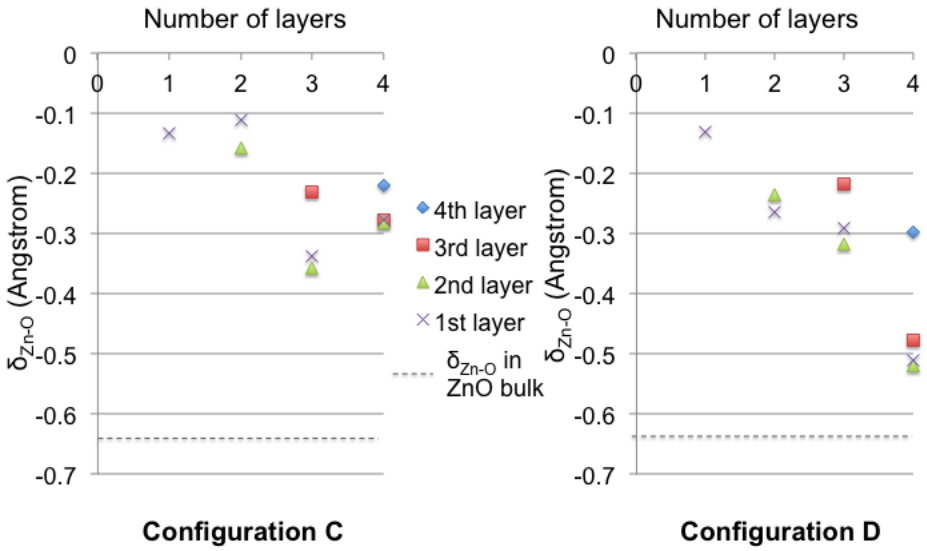

Figure 8-7: Average polarization vector δ_{Zn-O} in the ZnO layer(s) in $ZnO(0001)_n/PbTiO_3$ for n =1, 2, 3 and 4. Configurations C and D refer to starting polarization directions as in Fig 8-4(C) and (D) where the perovskite is negatively polarized.

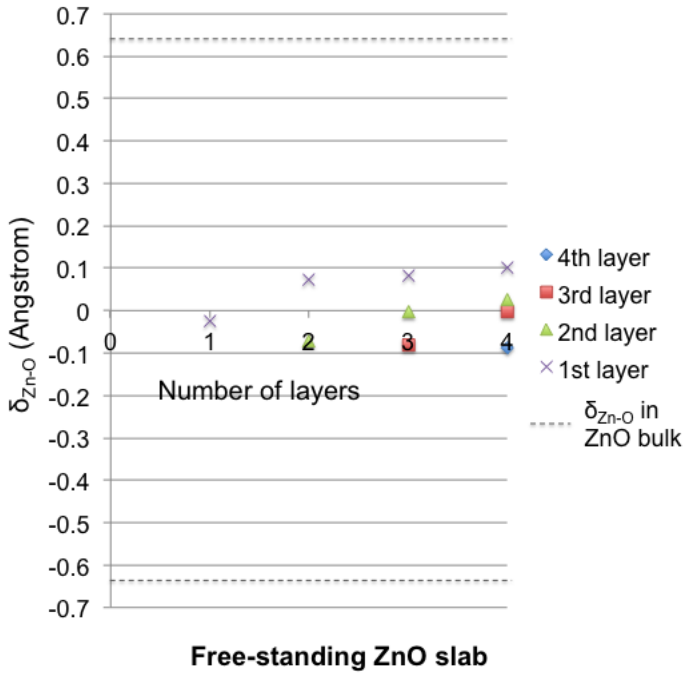

Figure 8-8: Average polarization vector δ_{Zn-O} in the ZnO layer(s) in free standing ZnO$(0001)_n$ for n =1, 2, 3 and 4.

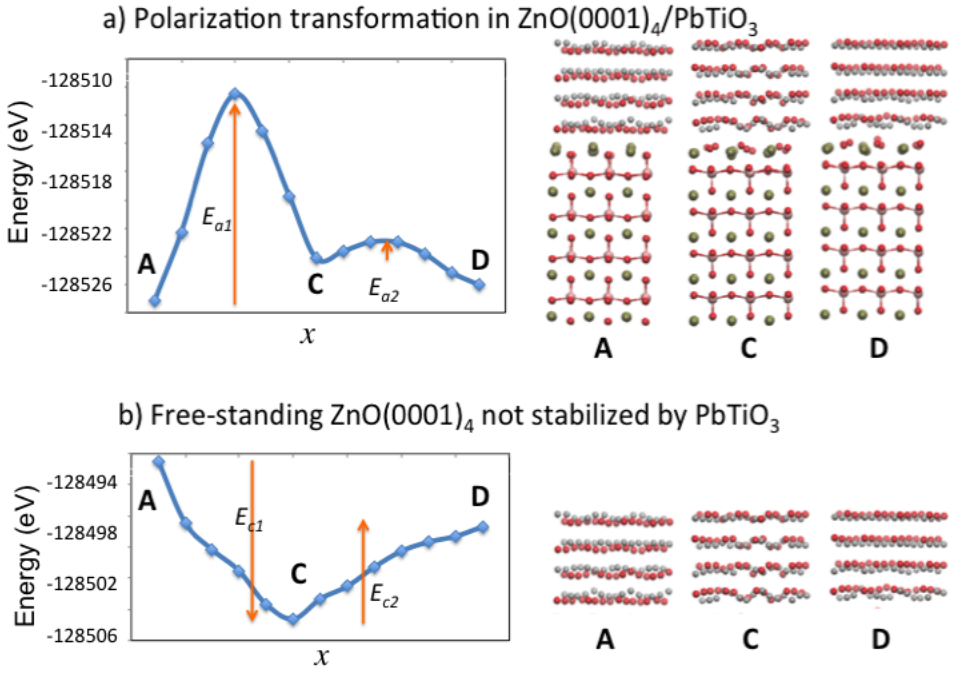

Figure 8-9: Transformation from up-polarized to down-polarized ZnO$(0001)_n$/$PbTiO_3$ for n=4.

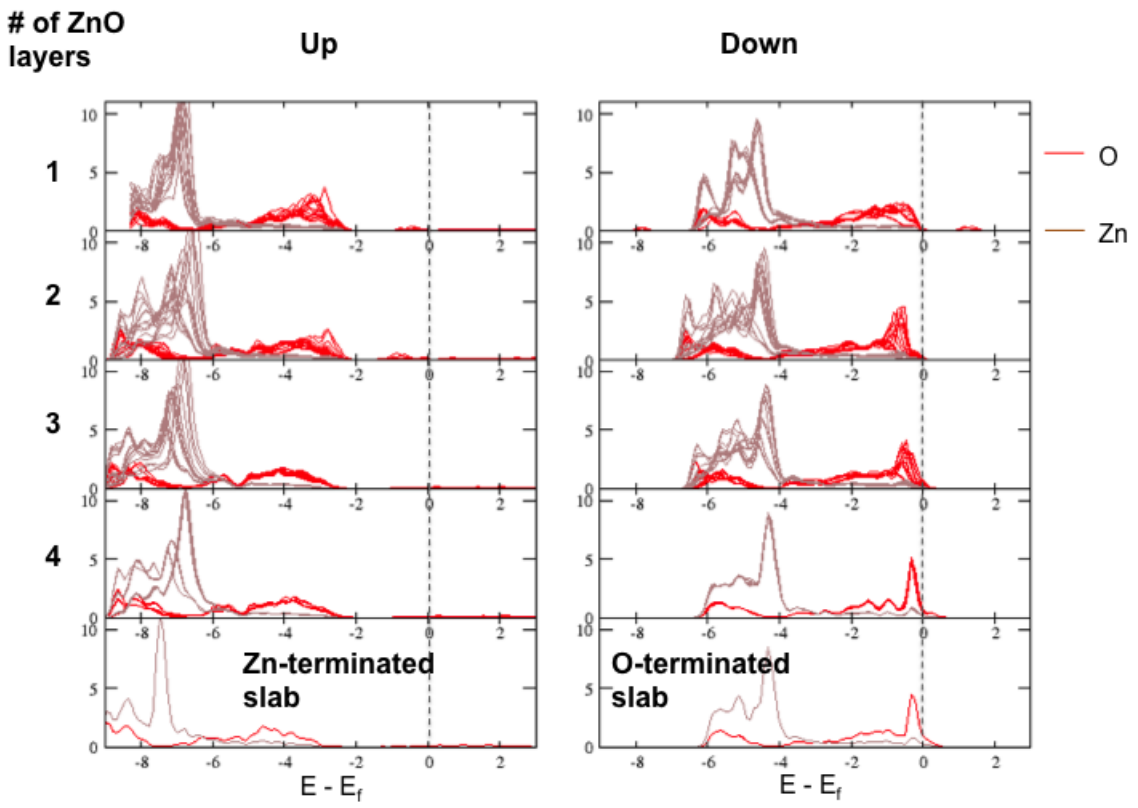

Figure 8-10: Densities of states projected on the topmost Zn and O atomic layers in $ZnO(0001)_n/PbTiO_3$ for n =1, 2, 3 and 4. The bottom graphs are for unsupported thick ZnO slabs.

characteristics similar to that of an O-terminated ZnO(0001) slab.

As was the case for the $ZnO(11\bar{2}0)$ epitaxy in the previous chapter, we calculated the relative interface formation energy for $ZnO(0001)_n$ on PbO-terminated $PbTiO_3$. The results for different number of layers and orientation of ZnO are shown in Fig. 8-11. We find that the first layer is quite stable, but as more layers are grown, the interface becomes less stable (though not necessarily unstable), meaning the ZnO layer at the interface prefers to bind with the next higher ZnO layer than with the PbO surface, which in turn will prefer to bind to the next higher layer if available and so on. As this process takes place, the interfacial ZnO layer is being 'dragged' up, at least for the ideal interface. This picture could change when vacancies are taken into account.

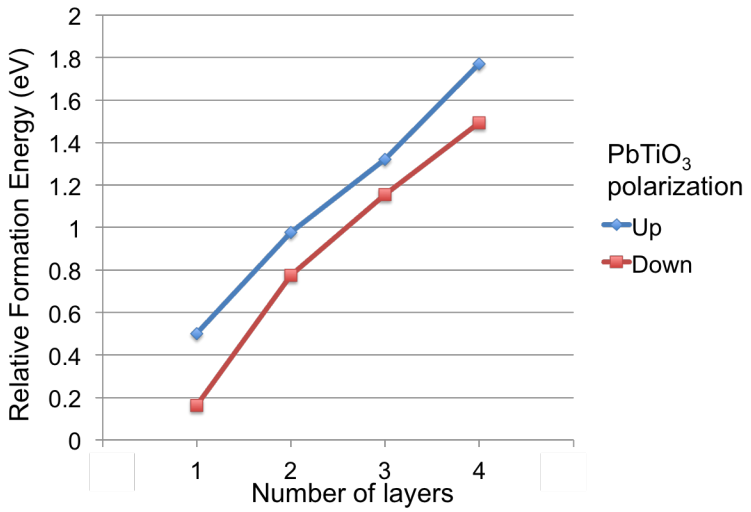

Figure 8-11: Relative interface formation energies for ZnO(0001) on up- and down-polarized $PbTiO_3$.

8.3.3 Adsorption properties

CO_2 adsorption

We calculated CO_2 adsorption energies on $ZnO(0001)_n/PbTiO_3$ and compared these to adsorption energies on ZnO(0001) slabs. Our results are consistent with the previous section, viz, the surface properties of up-polarized $ZnO(0001)_n/PbTiO_3$ corresponds to that of a Zn-terminated ZnO(0001) surface and the surface properties of the down-polarized $ZnO(0001)_n/PbTiO_3$ corresponds to that of an O-terminated ZnO(0001). The results are shown in Fig. 8-12. The difference in adsorption energies at the different polarizations is as high as 1.65eV and shows no sign of tapering after four layers.

The anomaly here is the case where n=1. We find that the adsorption energy at both polarization directions is the same. As discussed in Section 8.3.1, the perovskite substrate maintains the polarization of the ZnO which would have otherwise collapsed. The thinner the ZnO layer, the less the average polarization. Therefore as the ZnO layer thickness decreases, there is little intrinsic polarization in the layers. For the freestanding $ZnO(0001)_1$ slab, the polarization is practically zero (see Fig. 8-8). The perovskite coupling does not change this polarization so much, therefore the

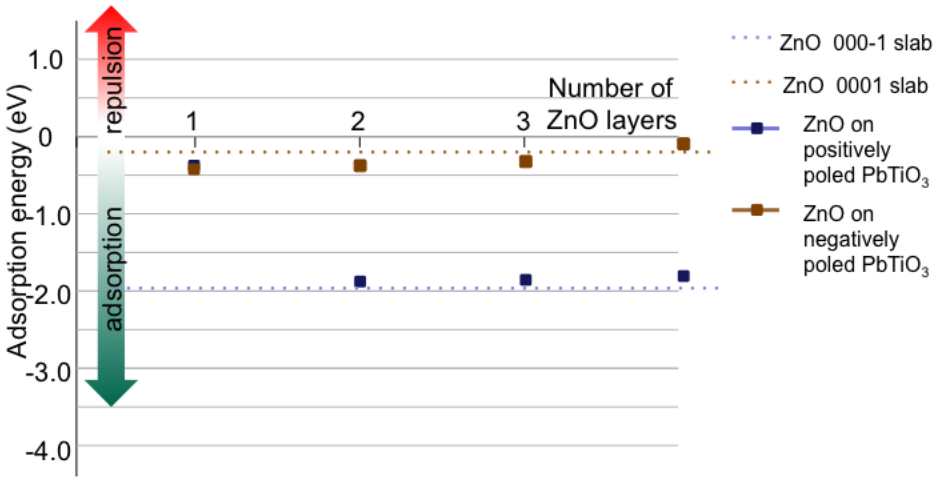

Figure 8-12: Adsorption energies of CO_2 on $ZnO(0001)_n/PbTiO_3$ for n =1, 2, 3 and 4. Lines denoting the adsorption of CO_2 on ZnO(0001) slabs are added.

surfaces at both substrate polarizations for n =1 are almost the same, and so are the adsorption energies.

8.4 Conclusion

We have explored the stable structures for the $ZnO(0001)_n/PbTiO_3$ system. We found that switching from the one polarization direction in the structure to the other should be possible. This means there is now a simple means to obtain a (high T_c) ZnO ferroelectric. For n >1, we can expect that $ZnO(0001)_n$ grown on $PbTiO_3$ will be a completely ferroelectric material - where the positively polarized structure is similar to the Zn-terminated ZnO(0001) surface and the negatively polarized structure is similar to O-terminated ZnO(0001) surface. Since the two polarization directions in polar ZnO(0001) have very different chemical and electronic properties, it should be worthwhile to explore the use of $ZnO(0001)_n/PbTiO_3$ as a tunable catalyst. This will be our next line of investigation.

Chapter 9

Summary and conclusion

Our overall goal was to explore tunable catalysis as a means to cheaply convert CO_2 to useful chemicals while saving the environment. We have applied density functional theory to explore a potential catalyst, $ZnO/PbTiO_3$ for this process. We have explored whether/how a perovskite influences the surface chemistry of the ZnO catalyst which is oriented in a non-polar $(11\bar{2}0)$ and then a polar (0001) direction.

We have seen that the surface chemistry of $ZnO(11\bar{2}0)_n/PbTiO_3$ is dependent on both the polarization direction of the $PbTiO_3$ substrate and on the number of $ZnO(11\bar{2}0)$ layers n. We also found that for $n \geq 4$, the effect of the substrate polarization is lost. CO_2 and methanol adsorption calculations show that the polarization direction which gives the best affinity changes as each additional ZnO layer is added switches. The mechanism for this process is hypothesized to be direct interaction of the first two ZnO layers and then secondary interactions of other layers with the PbO at the interface.

We also explored the possibility of using a polar ZnO surface. ZnO grown in the 0001 direction seemed a perfect candidate for a test case. We calculated the stable structures for the $ZnO(0001)_n/PbTiO_3$ system. We found that switching from the one polarization direction in the structure to the other should be possible. For n >1, we can expect that $ZnO(0001)_n$ grown on $PbTiO_3$ will be a completely ferroelectric material - where the positively polarized structure is similar to the Zn-terminated ZnO(0001) surface and the negatively polarized structure is similar to O-terminated

ZnO(0001) surface. This is an important result as there have been many attempts by researchers to make a wide-band-gap semi-conductor such as ZnO ferroelectric which will add a multifunctional nature to it.

Our future work will focus on finding the reaction pathways and energetics of CO_2 fixation to methanol and cyclic carbonates on $ZnO(11\bar{2}0)_n$/ and $ZnO(0001)/PbTiO_3$ surfaces, since our calculations have shown that they have quite different surface chemistries. In addition, we will explore the use of these structures as catalysts in electrochemical applications. The possibility of tuning the band-gap, density of states, orbital occupations, etc, which are common descriptors for electrochemical reactions, makes ZnO grown on a ferroelectric substrate an exciting candidate for such applications.

Bibliography

[1] Mette Mikkelsen, Mikkel Jørgensen, and Frederik C. Krebs. The teraton challenge. a review of fixation and transformation of carbon dioxide. *Energy & Environmental Science*, 3(1):43, 2010.

[2] Kevin Garrity, Arvin Kakekhani, Alexie Kolpak, and Sohrab Ismail-Beigi. Ferroelectric surface chemistry: First-principles study of the PbTiO3 surface. *Physical Review B*, 88(4):045401, July 2013.

[3] X. H. Wei, Y. R. Li, W. J. Jie, J. L. Tang, H. Z. Zeng, W. Huang, Y. Zhang, and J. Zhu. Heteroepitaxial growth of ZnO on perovskite surfaces. *Journal of Physics D: Applied Physics*, 40(23):7502, 2007.

[4] Steven Chu and Arun Majumdar. Opportunities and challenges for a sustainable energy future. *Nature*, 488(7411):294–303, August 2012.

[5] Appendix a: CO2 for use in enhanced oil recovery (EOR) | global carbon capture and storage institute.

[6] The Global CCS Institute. Accelerating uptake of CCS: industrial use of captured carbon dioxide. Technical report, March 2011.

[7] Carbon capture and storage: Special report of the intergovernmental panel on climate change. Technical report, IPCC, 2005.

[8] P. Viebahn and M. Fischedick. Carbon capture and storage in Germany–Cost development, life cycle assessment, and energy scenarios within an integrated assessment.

[9] M. Lenzen. Global warming effect of leakage from CO2 storage. *Critical Reviews in Environmental Science and Technology*, 2010.

[10] False hope: Why carbon capture and storage won't save the climate. Technical report, Greenpeace, May 2008.

[11] Walter Leitner. Supercritical carbon dioxide as a green reaction medium for catalysis. *Accounts of Chemical Research*, 35(9):746–756, September 2002.

[12] Clarence D Chang. Methanol to gasoline process. In *Perspectives in Molecular Sieve Science*, volume 368, pages 596–614. American Chemical Society, 1988.

[13] The Methanol Institute. The methanol industry report 2012.

[14] J. F. Knifton and R. G. Duranleau. Ethylene glycol—dimethyl carbonate cogeneration. *Journal of molecular Catalysis*, 67(3):389–399, 1991.

[15] S. Liang, H. Liu, T. Jiang, J. Song, G. Yang, and B. Han. Highly efficient synthesis of cyclic carbonates from CO2 and epoxides over cellulose/KI. *Chem. Commun.*, 47(7):2131–2133, 2010.

[16] K. Xu. Nonaqueous liquid electrolytes for lithium-based rechargeable batteries. *Chemical Reviews-Columbus*, 104(10):4303–4418, 2004.

[17] Michael North. Synthesis of cyclic carbonates from CO2 emissions. *Chemistry Today*, 30(3), June 2012.

[18] Yong Liu, Yi Zhang, Tiejun Wang, and Noritatsu Tsubaki. Efficient conversion of carbon dioxide to methanol using copper catalyst by a new low-temperature hydrogenation process. *Chemistry Letters*, 36(9):1182–1183, 2007.

[19] Xu and J. A. Moulijn. Mitigation of CO2 by chemical conversion: Plausible chemical reactions and promising products. *Energy & Fuels*, 10(2):305–325, January 1996.

[20] Andrew A. Peterson, Frank Abild-Pedersen, Felix Studt, Jan Rossmeisl, and Jens K. Nørskov. How copper catalyzes the electroreduction of carbon dioxide into hydrocarbon fuels. *Energy & Environmental Science*, 3(9):1311, 2010.

[21] Yoshio Hori, Akira Murata, and Ryutaro Takahashi. Formation of hydrocarbons in the electrochemical reduction of carbon dioxide at a copper electrode in aqueous solution. *Journal of the Chemical Society, Faraday Transactions 1: Physical Chemistry in Condensed Phases*, 85(8):2309–2326, January 1989.

[22] Edwin Ramaroson, Roger Kieffer, and Alain Kiennemann. Reaction of carbon dioxide and hydrogen on supported palladium catalysts. *Journal of the Chemical Society, Chemical Communications*, (12):645–646, January 1982.

[23] Xue-Lian Liang, Xin Dong, Guo-Dong Lin, and Hong-Bin Zhang. Carbon nanotube-supported Pd–ZnO catalyst for hydrogenation of CO2 to methanol. *Applied Catalysis B: Environmental*, 88(3–4):315–322, May 2009.

[24] L. Fan and K. Fujimoto. Promotive SMSI effect for hydrogenation of carbon dioxide to methanol on a Pd/CeO2 catalyst. *Journal of Catalysis*, 150(1):217–220, November 1994.

[25] Changpin Shao, Li Fan, Kaoru Fujimoto, and Yasuhiro Iwasawa. Selective methanol synthesis from CO2/H2 on new SiO2-supported PtW and PtCr bimetallic catalysts. *Applied Catalysis A: General*, 128(1):L1–L6, July 1995.

[26] Jun Ma, Nannan Sun, Xuelan Zhang, Ning Zhao, Fukui Xiao, Wei Wei, and Yuhan Sun. A short review of catalysis for CO2 conversion. *Catalysis Today*, 148(3–4):221–231, November 2009.

[27] Jean-Luc Dubois, Kazuhiro Sayama, and Hironori Arakawa. CO₂ hydrogenation over carbide catalysts. *Chemistry Letters*, 21(1):5–8, 1992.

[28] Andrew A. Peterson and Jens K. Norskov. Activity descriptors for CO2 electroreduction to methane on transition-metal catalysts. *Journal of Physical Chemistry Letters*, 3(2):251–258, January 2012.

[29] G. Parravano. Ferroelectric transitions and heterogenous catalysis. *The Journal of Chemical Physics*, 20(2):342–342, 1952.

[30] Yang Yun and Eric I. Altman. Using ferroelectric poling to change adsorption on oxide surfaces. *Journal of the American Chemical Society*, 129(50):15684–15689, December 2007.

[31] Li Li, Paul A. Salvador, and Gregory S. Rohrer. Photocatalysts with internal electric fields. *Nanoscale*, 6(1):24–42, 2014. WOS:000328673000001.

[32] Ionel Popescu, Adriana Urda, Tatiana Yuzhakova, Ioan-Cezar Marcu, Jozsef Kovacs, and Ioan Sandulescu. BaTiO3 and PbTiO3 perovskite as catalysts for methane combustion. *Comptes Rendus Chimie*, 12(9):1072–1078, September 2009.

[33] Mosha H. Zhao, Dawn A. Bonnell, and John M. Vohs. Effect of ferroelectric polarization on the adsorption and reaction of ethanol on BaTiO3. *Surface Science*, 602(17):2849–2855, September 2008.

[34] Dongbo Li, Mosha H. Zhao, J. Garra, A. M. Kolpak, A. M. Rappe, D. A. Bonnell, and J. M. Vohs. Direct in situ determination of the polarization dependence of physisorption on ferroelectric surfaces. *Nature Materials*, 7(6):473–477, June 2008.

[35] Yasunobu Inoue, Isao Yoshioka, and Kazunori Sato. Polarization effects upon adsorptive and catalytic properties. 1. carbon monoxide oxidation over palladium deposited on lithium niobate (LiNbO3) ferroelectrics. *The Journal of Physical Chemistry*, 88(6):1148–1151, March 1984.

[36] Y. Inoue, K. Sato, and S. Suzuki. Polarization effects upon adsorptive and catalytic properties. II: surface electrical conductivity of NiO deposited on LiNbO3 and its changes upon gas adsorption. *Journal of physical chemistry*, 89(13):2827–2831, 1985.

[37] Alexie M. Kolpak, Ilya Grinberg, and Andrew M. Rappe. Polarization effects on the surface chemistry of PbTiO3-Supported pt films. *Physical Review Letters*, 98(16):166101, April 2007.

[38] Y. Yun, N. Pilet, U. D. Schwarz, and E. I. Altman. Comparison of the interaction of pd with positively and negatively poled LiNbO3(0 0 0 1). *Surface Science*, 603(20):3145–3154, October 2009.

[39] J. E. Jones. On the determination of molecular fields. II. from the equation of state of a gas. *Proceedings of the Royal Society of London. Series A*, 106(738):463–477, October 1924.

[40] A. K. Rappe, C. J. Casewit, K. S. Colwell, W. A. Goddard, and W. M. Skiff. UFF, a full periodic table force field for molecular mechanics and molecular dynamics simulations. *Journal of the American Chemical Society*, 114(25):10024–10035, December 1992.

[41] Murray S. Daw and M. I. Baskes. Embedded-atom method: Derivation and application to impurities, surfaces, and other defects in metals. *Physical Review B*, 29(12):6443–6453, June 1984.

[42] Robert J. Le Roy, Nikesh S. Dattani, John A. Coxon, Amanda J. Ross, Patrick Crozet, and Colan Linton. Accurate analytic potentials for li2(x σ1g+) and li2(a σ1u+) from 2 to 90 å, and the radiative lifetime of li(2p). *The Journal of Chemical Physics*, 131(20):204309, November 2009.

[43] E. Schrödinger. An undulatory theory of the mechanics of atoms and molecules. *Physical Review*, 28(6):1049–1070, December 1926.

[44] P. Hohenberg and W. Kohn. Inhomogeneous electron gas. *Physical Review*, 136:864–871, November 1964.

[45] W. Kohn and L. J. Sham. Self-consistent equations including exchange and correlation effects. *Physical Review A*, 140:1133–1138, 1965.

[46] W. Kohn and L. J. Sham. Self-consistent equations including exchange and correlation effects. *Physical Review*, 140(4A):A1133–A1138, November 1965.

[47] G. B. Bachelet, D. R. Hamann, and M. Schlüter. Pseudopotentials that work: From h to pu. *Physical Review B*, 26(8):4199–4228, October 1982.

[48] David Vanderbilt. Soft self-consistent pseudopotentials in a generalized eigenvalue formalism. *Physical Review B*, 41(11):7892–7895, April 1990.

[49] Stefan Grimme. Semiempirical GGA-type density functional constructed with a long-range dispersion correction. *Journal of Computational Chemistry*, 27(15):1787–1799, November 2006.

[50] Jens Antony and Stefan Grimme. Density functional theory including dispersion corrections for intermolecular interactions in a large benchmark set of biologically relevant molecules. *Physical Chemistry Chemical Physics*, 8(45):5287, 2006.

[51] Stefan Grimme, Jens Antony, Tobias Schwabe, and Christian M?ck-Lichtenfeld. Density functional theory with dispersion corrections for supramolecular structures, aggregates, and complexes of (bio)organic molecules. *Organic & Biomolecular Chemistry*, 5(5):741, 2007.

[52] Arthur F. Voter and Jimmie D. Doll. Transition state theory description of surface self-diffusion: Comparison with classical trajectory results. *The Journal of Chemical Physics*, 80(11):5832–5838, June 1984.

[53] Graeme Henkelman, Blas P. Uberuaga, and Hannes Jónsson. A climbing image nudged elastic band method for finding saddle points and minimum energy paths. *The Journal of Chemical Physics*, 113(22):9901–9904, 2000.

[54] A. J. Cohen, P. Mori-Sanchez, and W. Yang. Insights into current limitations of density functional theory. *Science*, 321(5890):792–794, August 2008.

[55] Axel D. Becke. A new mixing of Hartree–Fock and local density-functional theories. *The Journal of Chemical Physics*, 98(2):1372–1377, January 1993.

[56] John P. Perdew, J. A. Chevary, S. H. Vosko, Koblar A. Jackson, Mark R. Pederson, D. J. Singh, and Carlos Fiolhais. Atoms, molecules, solids, and surfaces: Applications of the generalized gradient approximation for exchange and correlation. *Physical Review B*, 46(11):6671–6687, September 1992.

[57] David C. Langreth and M. J. Mehl. Beyond the local-density approximation in calculations of ground-state electronic properties. *Physical Review B*, 28(4):1809–1834, August 1983.

[58] S. Tinte, M. G. Stachiotti, C. O. Rodriguez, D. L. Novikov, and N. E. Christensen. Applications of the generalized gradient approximation to ferroelectric perovskites. *Physical Review B*, 58(18):11959–11963, November 1998.

[59] Z. Wu and R. E. Cohen. More accurate generalized gradient approximation for solids. *Physical Review B*, 73(23):235116, 2006.

[60] Fabien Tran, Robert Laskowski, Peter Blaha, and Karlheinz Schwarz. Performance on molecules, surfaces, and solids of the wu-cohen GGA exchange-correlation energy functional. *Physical Review B*, 75(11), March 2007.

[61] J. P. Perdew, K. Burke, and M. Ernzerhof. Generalized gradient approximation made simple. *Physical review letters*, 77(18):3865–3868, 1996.

[62] Stefan Grimme. Accurate description of van der waals complexes by density functional theory including empirical corrections. *Journal of Computational Chemistry*, 25(12):1463–1473, September 2004.

[63] Mark J. Allen and David J. Tozer. Helium dimer dispersion forces and correlation potentials in density functional theory. *The Journal of Chemical Physics*, 117(24):11113–11120, December 2002.

[64] Paolo Giannozzi, Stefano Baroni, Nicola Bonini, Matteo Calandra, Roberto Car, Carlo Cavazzoni, Davide Ceresoli, Guido L Chiarotti, and Matteo Cococcioni. QUANTUM ESPRESSO: a modular and open-source software project for quantum simulations of materials. *Journal of Physics: Condensed Matter*, 21(39):19, 2009.

[65] [http://webbook.nist.gov/chemistry/].

[66] Jo?rg Koßmann, Guido Roßmu?ller, and Christof Ha?ttig. Prediction of vibrational frequencies of possible intermediates and side products of the methanol synthesis on ZnO(0001) by ab initio calculations. *The Journal of Chemical Physics*, 136(3):034706, 2012.

[67] Sergio A. S. Farias, E. Longo, R. Gargano, and João B. L. Martins. CO2 adsorption on polar surfaces of ZnO. *Journal of Molecular Modeling*, 19(5):2069–2078, October 2012.

[68] Katawut Chuasiripattana, Oliver Warschkow, Bernard Delley, and Cathy Stampfl. Reaction intermediates of methanol synthesis and the water–gas-shift reaction on the ZnO(0001) surface. *Surface Science*, 604(19-20):1742–1751, September 2010.

[69] Na Sai, Alexie M. Kolpak, and Andrew M. Rappe. Ferroelectricity in ultrathin perovskite films. *Physical Review B*, 72(2):020101, July 2005.

[70] Rémi Arras, Victor G. Ruiz, Warren E. Pickett, and Rossitza Pentcheva. Tuning the two-dimensional electron gas at the LaAlO3/SrTiO3(001) interface by metallic contacts. *Physical Review B*, 85(12):125404, March 2012.

[71] Wang, Christopher J. Summers, and Zhong Lin Wang. Large-scale hexagonal-patterned growth of aligned ZnO nanorods for nano-optoelectronics and nanosensor arrays. *Nano Letters*, 4(3):423–426, March 2004.

[72] X. H. Wei, Y. R. Li, J. Zhu, W. Huang, Y. Zhang, W. B. Luo, and H. Ji. Epitaxial properties of ZnO thin films on SrTiO[sub 3] substrates grown by laser molecular beam epitaxy. *Applied Physics Letters*, 90(15):151918, 2007.

[73] W. Huang, J. Y. Dai, and J. H. Hao. Structural and resistance switching properties of ZnO/SrTiO[sub 3]/GaAs heterostructure grown by laser molecular beam epitaxy. *Applied Physics Letters*, 97(16):162905, 2010.

[74] Lennart Bengtsson. Dipole correction for surface supercell calculations. *Physical Review B*, 59(19):12301, 1999.

[75] Olga Dulub, Lynn A. Boatner, and Ulrike Diebold. STM study of the geometric and electronic structure of ZnO (0001)-zn,(0001)-o,(1010), and (1120) surfaces. *Surface Science*, 519(3):201–217, 2002.

[76] Ulrike Diebold, Lynn Vogel Koplitz, and Olga Dulub. Atomic-scale properties of low-index ZnO surfaces. *Applied Surface Science*, 237(1–4):336–342, October 2004.

[77] B. Meyer and Dominik Marx. Density-functional study of the structure and stability of ZnO surfaces. *Physical Review B*, 67(3), January 2003.

[78] P. W. Tasker. The stability of ionic crystal surfaces. *Journal of Physics C: Solid State Physics*, 12(22):4977, 1979.

[79] C Woll. The chemistry and physics of zinc oxide surfaces. *Progress in Surface Science*, 82(2-3):55–120, 2007.

[80] M. Kunat, St. Gil Girol, Th. Becker, U. Burghaus, and Ch. Wöll. Stability of the polar surfaces of ZnO: a reinvestigation using he-atom scattering. *Physical Review B*, 66(8), August 2002.

[81] A. Wander, F. Schedin, P. Steadman, A. Norris, R. McGrath, T. Turner, G. Thornton, and N. Harrison. Stability of polar oxide surfaces. *Physical Review Letters*, 86(17):3811–3814, April 2001.

[82] Mauro Sambi, Gaetano Granozzi, Gian Andrea Rizzi, Maurizio Casarin, and Eugenio Tondello. An angle-scanned photoelectron diffraction study on the surface relaxation of ZnO (0001). *Surface science*, 319(1):149–156, 1994.

[83] Claudine Noguera. Polar oxide surfaces. *Journal of Physics: Condensed Matter*, 12(31):R367, 2000.

[84] Johan M Carlsson. Electronic structure of the polar ZnO{0 0 0 1}-surfaces. *Computational Materials Science*, 22(1–2):24–31, November 2001.

[85] H. L. Stadler. Changing properties of metals by ferroelectric polarization charging. *Physical Review Letters*, 14(24):979–981, 1965.

[86] C H Jia, Y H Chen, G H Liu, X L Liu, S Y Yang, and Z G Wang. Structural and optical properties of ZnO films on SrTiO 3 substrates by MOCVD. *Journal of Physics D: Applied Physics*, 42(1):015415, January 2009.

[87] M. Karger and M. Schilling. Epitaxial properties of al-doped ZnO thin films grown by pulsed laser deposition on SrTiO3(001). *Physical Review B*, 71(7), February 2005.

[88] A. Onodera. Novel ferroelectricity in II-VI semiconductor ZnO. *Ferroelectrics*, 267(1):131–137, 2002.

[89] X. S. Wang, Z. C. Wu, J. F. Webb, and Z. G. Liu. Ferroelectric and dielectric properties of li-doped ZnO thin films prepared by pulsed laser deposition. *Applied Physics A*, 77(3-4):561–565, August 2003.

[90] C. W. Zou, M. Li, H. J. Wang, M. L. Yin, C. S. Liu, L. P. Guo, D. J. Fu, and T. W. Kang. Ferroelectricity in li-implanted ZnO thin films. *Nuclear Instruments & Methods in Physics Research Section B-Beam Interactions with Materials and Atoms*, 267(7):1067–1071, April 2009. WOS:000266155000004.